Dike-Driven Hydrothermal Processes on Mars and Sill Emplacement on Europa

Kathleen L. Craft

Dissertation submitted to the faculty of the Virginia Polytechnic Institute and State University in partial fulfillment of the requirements for the degree of

Doctor of Philosophy
In
Geosciences

Robert P. Lowell
Scott D. King
Erin Kraal
G. Wesley Patterson
Donald Rimstidt

September 3, 2013
Blacksburg, VA

Keywords: hydrothermal, dike, sill, ice, Mars, Europa, Athabasca Valles, fracture

Dike-Driven Hydrothermal Processes on Mars and Sill Emplacement on Europa

Kathleen L. Craft

ABSTRACT

Evidence of hydrothermal and tectonic activity is found throughout our solar system. Here I investigated hydrothermal and fracturing processes on three planetary bodies: Earth, Mars and Europa. For the first project, we set up a dike-driven hydrothermal system and calculated heat and water flow using boundary layer theory. Water flow rates and volumes were then compared to the requirements for surface feature formation. Results found that the water volumes produced were adequate to form Athabasca Valles, except the flow rates were low. Episodic flood releases could enable the higher flow rates if water was first collected in aquifers, possibly stored beneath ice. On the icy moon Europa, I modeled a proposed sill emplacement mechanism using a finite element code and found that water could flow up through an approximately 10 km thick ice shell without freezing. The analysis also found that shallow cracks in the ice combined with deep cracks cause a stress direction change that helps the fracture turn and propagate more horizontally. However, the sill lifetime is less than the time a study by *Dombard et al.* [2013] calculated to be necessary for the formation of flexure fractures along margins of double ridges. Replenishment processes will be explored in future work to help extend sill lifetime. The last investigation calculated dike induced permeability changes in the crust on Earth and Mars and related the changes to water and heat flow rates and water volumes. Comparisons were made to event plume heat and elevated fluid

temperatures observed at mid-ocean ridges. Heat values determined by the models agreed well with the 10^{14} to 10^{17} J expected. For the Martian model, water flow rates and volumes were compared to formation requirements for the valley system Athabasca Valles. Results found that flow rates would be adequate in the high permeability damage zone adjacent to the dike. However, the lowered permeability outside the damage zone would restrict replenishment flow and could cause the need for water storage and periodic release between flood events as the volume within the damage zone is not adequate for the valley formation.

DEDICATION

This dissertation is dedicated to my boys, Liam and Corbin, may you always be curious, bright eyed and looking for the next adventure. Find joy and also help to make some.

I also dedicate this work to a friend and colleague lost along the way. Kurt Frankel, you were taken too early, yet in the short time we knew each another your laughter and wisdom inspired and encouraged me. Thank you.

ACKNOWLEDGEMENTS

This work would not have been possible without the tremendous support of many people. I first would like to thank my advisor, Robert Lowell, for his constant support, donation of his time, and guidance over the past 7 years we have worked together. I look forward to future collaborations. I greatly appreciate the guidance from my committee members: Scott King, Erin Kraal, Wes Patterson, and Don Rimstidt. Much appreciation goes to Louise Prockter and Wes Patterson for introducing me to the icy body Europa and helping me get involved in mission work. And a very big thanks to the geophysics students at Virginia Tech who helped me remain steadfast in my goal, especially my dear friends Pavithra Sekhar, Karina Cheung, Aida Farough, Sharmin Shamsalsadati, and Kristie Dorfler. You ladies rock.

I cannot thank my family and friends enough for their continuous support including: my parents, Lynn and Wayne Hale, and in-laws, Liz and Bill Craft; friends Nancy and Dan Dudek, Laurie and Jon Fritsch, Cindy Rosenbaum and Matt Wisnioski, Sandie Klute, Cathy and Mike Field, Pam and Ethan Swint and Jeni Walke. Thank you to my children for providing distraction when I needed it (or didn't), and most of all so much laughter and perspective on life. Last, I could not have completed this dissertation without the incredible love and support (and patience) of my husband Michael Craft. Thank you honey, you are wonderful.

This research was supported in part by NASA grant #NNX10AO38G to R. P. Lowell, a Virginia Space Grant Award to K. L. Craft and Virginia Tech Multicultural Awards and Opportunities Program funding to K. L. Craft.

Table of Contents

LIST OF FIGURES

LIST OF TABLES

LIST OF SYMBOLS

Each chapter has its own symbols table(s) at the end of the section

PREFACE

The first chapter was published in the Journal for Geophysical Research, Planets, May 2012. Robert P. Lowell was a co-author. It is presented here in its published format.

The second chapter will be submitted to Icarus following review here by the committee. Co-authors will be G. Wesley Patterson, R. P. Lowell and L. Germanovich.

The third chapter will be submitted for publication with R. P. Lowell and L. Germanovich as co-authors.

1 Introduction

This work seeks to explore hydrothermal and fracturing processes on planetary bodies. We begin by investigating possible hydrothermal activity on Mars motivated by evidence observed by rovers and orbiting spectrometers that suggested hydrothermal deposits including hydrated silicate deposits existed on the surface [*Murchie et al.*, 2007; 2009; *Bibring et al.*, 2004]. Also, surface feature morphologies indicate volcanic and fluvial processes had been part of the their formation processes, possibly in the geologically recent past. Drawing from experience modeling terrestrial mid-ocean ridge hydrothermal circulation, we apply boundary layer calculations to determine if hydrothermal activity driven by dike intrusions could provide the volume of water, at the rates needed to form surface morphology. In particular, we compare our results to the flood feature Athabasca Valles. We also calculate ice melt and vapor phase transition to determine the effect on flow rates and volume produced.

Another planetary body, Europa, which also exhibits many different types of features on its surface, drew our interest. Recent work by *Dombard et al.* [2013] suggested the need for a shallow water sill to exist beneath the icy surface at about 1 km depth to enable flexure observed at some double ridges. Shallow water bodies on Europa have astrobiological implications in that the water could be a location for life and may be accessible for exploration. Our investigation seeks to find a feasible method for fracturing within the shell and driving ocean water from the base of the ice shell up to a shallow depth. Then, through application of a finite element program, we explore the ability to initialize and propagate a horizontal fracture through the application of: shallow and deep cracks, material layering and lateral stress gradients. The lifetime of a shallow water sill was also calculated and considered in relation to the models by *Dombard et al.* [2013] for formation of the double ridge flanking fractures.

The last project combines the investigation tactics applied in the first two projects: hydrothermal modeling and fracture mechanics to consider how the emplacement process of a dike intrusion would occur and effect the surrounding stress field and permeability on Earth and Mars. Changes in permeability relate to changes in fluid flow rates and volumes through the boundary layer calculations. Results are used to determine if water and heat flows are adequate for terrestrial event plumes observed at mid-ocean ridges, where sudden and high temperature flows occur. Investigations for Martian diking events apply resulting permeability changes to fluid flow evaluations and relate volume and flow rate results to formation requirements for the flood feature Athabasca Valles. We also compare stress levels in the crust to those calculated by a previous study by *Hanna and Phillips* [2006] that suggested pressurization of a subsurface aquifer could supply floods for surface morphology formation.

2 Boundary Layer Models of Hydrothermal Circulation on Mars and its Relationship to Geomorphic Features

Craft, K. L., and R. P. Lowell (2012), Boundary layer models of hydrothermal circulation on Mars and its relationship to geomorphic features, J. Geophys. Res., 117, E05006, doi:10.1029/2012JE004049.

http://onlinelibrary.wiley.com/doi/10.1029/2012JE004049/abstract

Boundary layer models of hydrothermal circulation on Mars and its relationship to geomorphic features

Kathleen L. Craft[1] and Robert P. Lowell[1]

Received 10 January 2012; revised 26 March 2012; accepted 28 March 2012; published 16 May 2012.

[1] We apply steady state boundary layer theory to single phase, dike-driven hydrothermal systems beneath the surface of Mars to provide estimates of the heat and liquid water outputs over a range of crustal permeabilities and dike dimensions. Model results yielded a heat output of $\sim 1.8 \times 10^{19}$ J/yr and a volumetric fluid flow rate of ~ 15 km^3/yr for a 1000 km long, 1 km tall dike-like intrusion injected into crust with a permeability of 10^{-11} m^2. A similar, 10 km tall dike could generate a heat output of $\sim 5.6 \times 10^{19}$ J/yr and ~ 46 km^3/yr of fluid flow. For dike half-widths of 10 and 100 m, total volume production of fluid ranged between ~ 45 and $\sim 13{,}800$ km^3 along one side of the dike over the respective 3 and 300 year half-dike lifetimes. The calculated fluid flow rates are much less than those estimated for production of the outflow channel system, Athabasca Valles; yet, the total fluid volume produced is of the required magnitude. If fluid could be stored in a near surface reservoir until later episodic release(s), the water volume supplied by one side of a single, 100 m half-width, 200 km long, and 10 km tall dike emplaced into a region with permeability equal to 10^{-11} m^2 could form the outflow channel. Hydrothermally generated meltwater from an overlying, near surface ice layer was found to contribute significantly to the fluid flow volume for this system.

Citation: Craft, K. L., and R. P. Lowell (2012), Boundary layer models of hydrothermal circulation on Mars and its relationship to geomorphic features, *J. Geophys. Res.*, *117*, E05006, doi:10.1029/2012JE004049.

1. Introduction

[2] Hydrothermal systems exist at many locations in the Earth where heat sources drive fluid circulation [e.g., *Lowell*, 1991; *Lowell and Rona*, 2004]. Analogous systems are likely to exist, or have previously existed on other planetary bodies where environmental conditions allow for fluid stability near the surface for some part of the planet's history and where volcanism, impacts, and/or tidal stresses generate large thermal gradients that drive fluid flow. Hydrothermal systems could contribute to a planet's heat transfer as they do on Earth. *Elderfield and Schultz* [1996] estimate that about 25% of the total global heat flux occurs from hydrothermal flow in oceanic crust younger than ~65 Ma; however, hydrothermal systems contribute only a small fraction of the heat loss from continental crust. Moreover, they could serve as energy resources and as agents for geochemical cycling and ore formation [e.g., *Edmond et al.*, 1979; *Hedenquist and Lowenstern*, 1994; *Hannington et al.*, 1995]. Because hydrothermal systems have been linked to the origin of life on Earth [e.g., *Baross and Hoffman*, 1985], they may provide clues to the existence of life elsewhere in the solar system. It is therefore of critical scientific importance to understand hydrothermal processes on planetary bodies.

[3] As evidenced by fluvial features associated with volcanic activity and hydrothermal deposits, hydrothermal systems have existed on Mars from the Noachian period (≥3.5 billon years ago) to geologically recent years. During the Noachian period the atmosphere might have been denser [e.g., *Pollack et al.*, 1987; *Jakosky and Phillips*, 2001] and rainfall may have been a major formation mechanism for surface features [*Craddock and Maxwell*, 1993; *Gulick*, 1998; *Baker et al.*, 1991]. However, there is evidence that certain surface features on Mars, including many of the outflow channels, formed more recently than the Noachian period in a climate where rainfall was not and currently is not possible [*Mouginis-Mark*, 1990; *Baker*, 2001; *Hamilton et al.*, 2011]. Also, many small valleys are found grouped together as opposed to spread more evenly across the terrain, indicating formation by groundwater outflow rather than rainfall [*Gulick and Baker*, 1993; *Gulick*, 1993, 1998; *Gulick et al.*, 1997]. Additionally, the valleys exhibit sapping as opposed to runoff morphology [*Baker et al.*, 1992].

[4] Fluvial features indicating hydrothermal formation include valleys and outflow channels. *Brakenridge et al.* [1985] hypothesized that certain small valleys resulted from impact melting of ground ice and subsequent fluid flow. Most outflow channels are located near volcanic features. For example, the Athabasca Valles channels originate at a fissure within Cerberus Fossae, a series of fissures believed to have

[1]Department of Geosciences, Virginia Polytechnic Institute and State University, Blacksburg, Virginia, USA.

Corresponding author: K. L. Craft, Department of Geosciences, Virginia Polytechnic Institute and State University, Blacksburg, VA 24060, USA. (kcraft5@vt.edu)

0148-0227/12/2012JE004049

formed from dike emplacement [*Burr et al.*, 2002a; *Head et al.*, 2003] driven by flexural loading in the Tharsis and Elysium Mons regions [*Hall et al.*, 1986; *Hanna and Phillips*, 2006].

[5] Deposits suggesting hydrothermal origin have been observed by the Mars rovers and orbiters. Hydrated silicate deposits, including phylosillicates, have been observed within craters by the spectrometers CRISM (Compact Reconnaissance Imaging Spectrometer for Mars) [*Murchie et al.*, 2007, 2009] and OMEGA (Observatoire pour la Mineralogie, L'Eau, les Glaces et l'Activitié) [*Bibring et al.*, 2004] and also confirmed by TES (Thermal Emission Spectrometer) [*Christensen et al.*, 2001] and THEMIS (Thermal Emission Imaging System) [*Christensen et al.*, 2004] readings. *Marzo et al.* [2010] suggests the hydrated silicate deposits resulted from hydrothermal activity associated with the crater forming impact processes rather than exposure of earlier formed deposits. Hydrated silicates are also observed in areas containing geomorphic features consistent with hydrothermal activity [*Marzo et al.*, 2010]. *Ehlmann et al.* [2009] also find evidence for mineral phases and assemblages indicative of possible hydrothermal activity in cratered terrains using CRISM and OMEGA data. On Mars, clay minerals are observed to be widespread on Noachian terrain and *Ehlmann et al.* [2011] assert that the minerals and the relative ages and stratigraphic relationships of the clay deposits indicate formation by subsurface hydrothermal activity. Also, *Squyres et al.* [2008], *Yen et al.* [2008] and *Schmidt et al.* [2008] suggest hydrothermal activity in Gusev Crater based on halogens and silicates analyzed by the Spirit rover.

[6] While it is unlikely water or ice exists in the near subsurface globally on Mars, certain areas may contain sizable quantities as suggested by observations from multiple orbiting instruments. For example, *Watters et al.* [2007] analyzed data from the Mars Advanced Radar for Subsurface and Ionospheric Sounding (MARSIS) instrument that indicates a possible ice rich area within the equatorial Medusae Fossae Formation. Also, a study of High Resolution Imaging Science Experiment (HiRISE), Context Camera (CTX), and Mars Orbiter Camera (MOC) images by *Hamilton et al.* [2011] of cratered cones and pitted terrains in the western Tartarus Colles region (25°N–27°N, 170°E–171°E) suggests the features formed as a result of lava-ground ice interactions. *Seibert and Kargel* [2001] suggest ice wedge activity from observations of contraction-crack polygon features. SHARAD data indicates ice rich units (abundant reflections) dated late Amazonian in latitudes 40–50°N [*Stillman and Grimm*, 2011]. In other regions, SHARAD imaging fails to detect water and ice, although *Stillman and Grimm* [2011] state that water alteration and/or absorption may cause signal scattering and attenuation that prevents detection. *Plaut et al.* [2007] describe ice rich deposits detected by the MARSIS instrument in the south polar regions. Using the HiRISE, *McEwen et al.* [2011] observed dark lineae that lengthen in the warm seasons and recede in cold ones. They suggest the lineae may indicate liquid brines near the surface. Recent impacts and volcanism may have interacted with the subsurface ice/water and enabled hydrothermal activity under current environmental conditions [e.g., *Hamilton et al.*, 2011]. Hydrothermal systems, therefore, are a plausible formation mechanism for past and certain recent fluvial features since water can only exist for a short period at the surface and rain is not possible currently.

[7] Quantitative analyses have been performed previously on various types of Martian hydrothermal systems. For example, *Gulick* [1998] and *Harrison and Grimm* [2002] modeled hydrothermal systems driven by magmatic intrusions. *Rathbun and Squyres* [2002], *Abramov and Kring* [2005] and *Barnhart et al.* [2010] investigated impact driven systems, and *Squyres et al.* [1987] and *Ogawa et al.* [2003] discussed the role of sills and lava flows as a mechanism for melting permafrost. Our analyses of hydrothermal systems on Mars consider a system similar to *Gulick* [1998] and *Harrison and Grimm* [2002] consisting of a subsurface magma intrusion emplaced in a water saturated porous medium (Figure 1). *Gulick*'s [1998] results predict that large temperature gradients exist within less than 100 m of the intrusion, suggesting that fluid behavior close to the chamber may dominate the mass and heat transfer regime. *Harrison and Grimm* [2002] focus on somewhat more sill-like geometries.

[8] To complement the models of *Gulick* [1998] and *Harrison and Grimm* [2002], we focus on hydrothermal flow driven by igneous dike intrusions. In this setting, hydrothermal systems tend to be relatively short-lived as a result of the relatively small thickness to height ratio of the intrusion, but the heat and fluid fluxes may be substantial because of the sharp thermal gradients that occur near the dike boundary. Hydrothermal circulation near a dike represents a fundamental end-member case of a magma-driven hydrothermal process that has received relatively little attention.

[9] To capture the fluid flow and heat transfer behavior near the dike wall, we employ a steady state boundary layer theory approach. Because the boundary thins as the permeability increases, the analytical solution provides high spatial resolution results for the temperature and velocity distributions close to the dike wall, especially in high-permeability settings that may be difficult to address numerically. Additionally, the boundary layer method provides a clear understanding of the fundamental physics and provides parametric relationships that can be used to verify numerical simulations. The steady state boundary layer methodology also provides an upper limit estimate to the heat and fluid output, while enabling relatively simple parametric quantification of hydrothermal heat and mass transfer for a broad range of possible Martian crustal permeabilities. By focusing on heat and mass transfer in the narrow boundary layer adjacent to the intrusion at early times where these processes are maximal, the boundary layer approach complements the model of *Gulick* [1998] as well as the work of *McKenzie and Nimmo* [1999] who considered heat transfer from a conductively cooling dike and that of *Hanna and Phillips* [2006] who modeled rapid egress of fluid near a dike as a result of dike generated stresses. Note that in the analyses below, we only consider flow along one side of the dike, and hence consider the half-width of the dike as the heat source. Fluid flow volumes are double what we calculate below. Because permeability, which may vary over several orders of magnitude, is the main controlling parameter in our analyses, however, we neglect the factor of two in the estimated flow rates.

[10] Additionally, we explore the effects of two-phase flow and the volume of fluid produced by melting a layer of

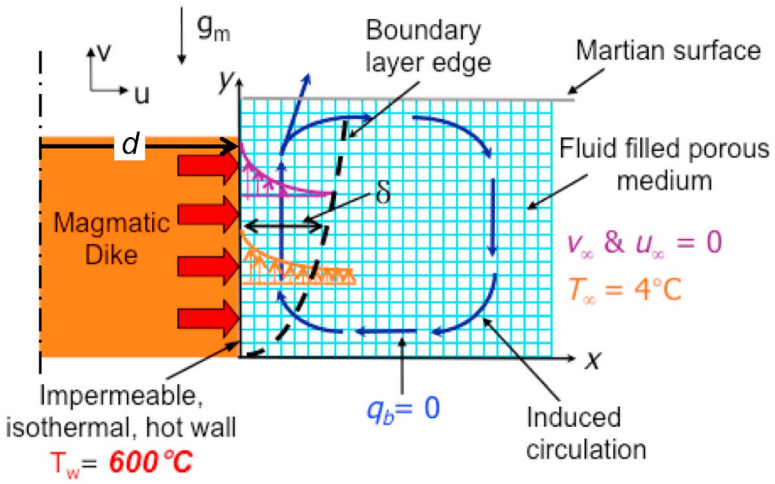

Figure 1. Steady state boundary layer model of magma-driven hydrothermal circulation on Mars. Constant temperature wall transfers heat to adjacent, fluid filled, porous medium and induces circulation. A boundary layer forms next to the hot wall. The change in velocity and temperature across the boundary layer thickness are shown by the profiles drawn in purple (velocity) and orange (temperature). Symbols are defined in Table 1.

ice overlying a dike-driven hydrothermal system. A layer of ice or permafrost located above the hydrothermal system would slowly melt as the circulating hydrothermal fluid transfers heat to the ice above. The fluid produced by melting the ice layer could contribute a significant amount to the volume reaching the surface and forming morphology there. Finally, we then compare our results to previous models and discuss the feasibility for a hydrothermal system to form the Athabasca Valles fluvial features on Mars.

2. Hydrothermal Circulation

2.1. Model Set-up

[11] The mathematical simplification that results from applying boundary layer theory provides considerable insight into hydrothermal system behavior without performing complicated numerical calculations. Figure 1 depicts the two-dimensional model and boundary conditions for a hydrothermal system on Mars near a hot vertical wall representing the boundary of a magmatic dike-like intrusion, and cartoons of the resulting circulation and thermal boundary layer. Horizontal position within the model is denoted by x, and vertical position is given by y. The vertical, impermeable, heated wall is set at a constant temperature, T_w, and conducts heat through to the adjacent fluid saturated medium that is initially at 4°C. T_w is set to 600°C to simulate the estimated temperature of the crust directly adjacent to the hot magma intrusion (~1200°C) [*Carslaw and Jaeger*, 1959]. Other parameters noted in Figure 1 include Martian gravity, g, and the horizontal and vertical fluid velocities infinitely far from the heated wall, u_∞ and v_∞ respectfully, which are set to zero. Additionally, there is no heat or fluid flow across the bottom horizontal boundary. Definition of variables and parameters used are given in Table 1.

2.2. Boundary Layer Theory

[12] To analyze the hydrothermal system, we applied the boundary layer theory as described by *Cheng and Minkowycz* [1977] and *Bejan* [1995]. Boundary layer theory assumes that convection is vigorous and occurs within a thin layer adjacent to the hot wall. In this way, boundary layer theory provides a good approximation for convection near the sides of a magmatic intrusion, especially in the early stages after convection stabilizes. Because the theory assumes a steady state, it provides an upper estimate to the convective heat and mass flux near the intrusion. This theory was chosen, in part, after reviewing results obtained by *Gulick* [1998] for hydrothermal circulation near the wall of a cooling intrusion that showed the majority of temperature change occurred within a relatively narrow region near the intrusion boundary [see *Gulick*, 1998, Figure 5].

[13] As heat is transferred by conduction from the hot wall to the adjacent fluid, its density decreases and the resulting buoyancy drives the hot fluid upward; conservation of mass requires that cooler water further from the wall moves toward the wall to replace the hot fluid. The cooler water is then heated such that for the system with a fixed wall temperature, steady state circulation occurs. The change in velocity and temperature across the boundary layer thickness are shown schematically in Figure 1 by the profiles drawn in purple (velocity) and orange (temperature). An assumption made in the boundary layer model is that outside of the boundary layer there is little change in temperature and velocity from the initial values.

[14] For a two-dimensional system, the governing, nonlinear partial differential equations that describe a hydrothermal system include conservation of mass:

$$\frac{\partial u}{\partial x} + \frac{\partial v}{\partial y} = 0 \qquad (1)$$

Table 1. Definition of Variables for Hydrothermal Circulation Analyses

Symbol	Definition	Value	Units
a	Effective thermal diffusivity of rock-fluid mixture	Equation (11)	m^2s^{-1}
$c_{p,f}$	Specific heat of the fluid	4.18	kJ $(kg°C)^{-1}$
$c_{p,r}$	Specific heat of the rock	0.84	kJ $(kg°C)^{-1}$
d	Dike half-width	Varies	m
f	Similarity variable for velocities	Equation (9)	unitless
g	Martian gravitational acceleration	3.72	ms^{-1}
H	Dike height	1 or 10	km
K	Permeability	10^{-14} to 10^{-8}	m^2
Nu	Nusselt number	$\sim Ra^{1/2}$	unitless
P	Pressure acting on fluid	Varies	MPa
Q_{bl}	Heat flow per length across boundary layer	Equation (18)	J/km/yr
q_b	Heat flow per length along base of model area	0	J/km/yr
Ra_y	Rayleigh number	Equation (12)	unitless
T_w	Temperature of heated wall	600	°C
T_0	Initial temperature of heated wall at emplacement	1200	°C
T_∞	Temperature at infinite distance from heated wall	4	°C
$\langle T \rangle$	Average temperature across boundary layer thickness	125	°C
t_f	Fluid travel time from bottom to top of dike	Varies	yr
u	Horizontal velocity	Varies	ms^{-1}
u_∞	Horizontal velocity at infinite distance from heated wall	0	ms^{-1}
v	Vertical velocity	Equation (15)	ms^{-1}
v_D	Darcian velocity vector	Varies	ms^{-1}
v_∞	Vertical velocity at infinite distance from heated wall	0	ms^{-1}
$\langle v \rangle$	Average Vertical velocity across boundary layer thickness	Varies	ms^{-1}
x	Horizontal position	Varies	m
y	Vertical position	0 to 10,000	m
y_v	Vertical position above the critical depth for vapor/liquid	Varies	m
α_f	Thermal expansion coefficient of water for high temperatures	10^{-3}	$°C^{-1}$
γ	Value such that heat flux is conserved across the vapor-water interface	1	unitless
δ	Boundary layer thickness	Equation (17)	m
δ_v	Thickness of vapor boundary layer	Equation (21)	m
η	Similarity variable for position	Varies	unitless
η_δ	Position value at edge of boundary layer	6.6	unitless
λ_m	Thermal conductivity of rock-fluid mixture	2.6	J $(sm°C)^{-1}$
θ	Similarity variable for temperature	Equation (10)	unitless
μ	Dynamic viscosity of the fluid for high temperatures	10^{-4}	kg $(m\ s)^{-1}$
ξ	Dynamic viscosity of steam	2.1×10^{-5}	kg $(m\ s)^{-1}$
ρ_∞	Density of the fluid at infinite distance from heated wall	1000	$kg\ m^{-3}$
ρ_f	Density of the fluid	Equation (5)	$kg\ m^{-3}$
ρ_v	Density of the vapor	715	$kg\ m^{-3}$
τ	Conductive time scale	Varies	yr
Φ_{vol}	Fluid volume flow rate per length	Equation (19)	$m^3(m\ yr)^{-1}$
ψ	Stream function	Varies	m^2s^{-1}

Darcy's law (conservation of momentum):

$$u = (-K/\mu)\frac{\partial P}{\partial x} \tag{2}$$

$$v = (-K/\mu)\left(\frac{\partial P}{\partial y} + \rho_f g\right) \tag{3}$$

conservation of energy:

$$c_{p,f}\rho_f v_D.\nabla T = \lambda \nabla^2 T \tag{4}$$

and temperature dependent density:

$$\rho_f = \rho_\infty\left[1 - \alpha_f(T - T_\infty)\right] \tag{5}$$

[*Bejan*, 1995; *Cheng and Minkowycz*, 1977]. The variables are defined as: *u, v*: horizontal and vertical Darcian velocities of the fluid, respectively; *x, y*: horizontal and vertical position, respectively; $c_{p,f}$: specific heat of fluid; *g*: gravity; *K*: permeability; λ_m: thermal conductivity of rock-fluid mixture; *P*: pressure; $\boldsymbol{v_D}$: the Darcian velocity vector; *T*: temperature; T_∞: temperature infinitely far from hot wall; α_f: thermal expansion coefficient of water; μ: fluid dynamic viscosity; ρ_f: fluid density; ρ_∞: density infinitely far from hot wall. Variables and their definition are located in Table 1.

[15] We do not consider a temperature gradient with depth for T_∞, as the estimated Martian gradient of $\sim$10°C/km would give about a 130°C increase for the deepest system we consider at $\sim$13 km. This temperature change makes little difference in our results because it affects the Rayleigh number by only 20%, whereas permeability ranges over six orders of magnitude ($K = 10^{-14}$ to 10^{-8} m^2). The permeability of the Martian crust is not known and likely exhibits spatial variability. Basaltic ocean crust permeability may be as high as $\sim 10^{-9}$ m^2 (*Fisher*, 1998) and similar estimates have been obtained for lava flow regions in the Oregon and California Cascades [*Manga*, 2004; *Saar and Manga*, 2004], which may be close to that expected at Cerebus Fossae. We extend the range slightly to 10^{-8} m^2 to take into account the crust of Mars has likely been fractured by multiple meteorite impacts. As discussed in *Gudmundsson* [2001], the damage

zones surrounding fractures, such as those formed by dike intrusions or meteorite impacts, increase the permeability above that typically expected at depth. To set a lower limit, we take into account permeability estimates for 2A basalt layers at terrestrial mid-ocean ridges from measurements in ophiolites that are on the order of 10^{-12} to 10^{-10} m^2 [*Nehlig and Juteau*, 1988; *van Everdingen*, 1995]. Also, observational studies of the Endeavor segment of the Juan de Fuca Ridge by *Wilcock and McNabb* [1996] estimate permeabilities on the order of 10^{-13} to 10^{-12} m^2. We consider these estimates and assume a lower limit crustal permeability on Mars of 10^{-14} m^2, because for the geometries considered, boundary layer theory is not applicable for lower permeabilities. Other Martian hydrothermal system studies have considered similar permeabilities [e.g., *Barnhart et al.*, 2010; *Harrison and Grimm*, 2002].

[16] Boundary conditions are then set for the system:

$$\begin{aligned} u &= 0; \quad T = T_w \ at \ x = 0 \\ v &= 0; \quad T = T_\infty \ at \ x = \infty \end{aligned} \tag{6}$$

To solve the equations, we wrote the velocity components in terms of the stream function, ψ:

$$\begin{aligned} u &= -\frac{\partial \psi}{\partial y} \\ v &= \frac{\partial \psi}{\partial x} \end{aligned} \tag{7}$$

As described in *Bejan* [1995] and *Cheng and Minkowycz* [1977], we then converted equations (1) through (7) to a set of ordinary differential equations using the similarity variable, η:

$$\eta = Ra_y^{1/2}(x/y) \tag{8}$$

and dimensionless parameters:

$$f(\eta) = \frac{\psi}{aRa_y^{1/2}} \tag{9}$$

$$\theta(\eta) = \frac{(T - T_\infty)}{(T_w - T_\infty)} \tag{10}$$

where

$$a = \frac{\lambda_m}{\rho_\infty c_{p,f}} \tag{11}$$

is the effective thermal diffusivity and Ra_y is the Rayleigh number for flow within a porous medium as defined by [e.g., *Bejan*, 1995]:

$$Ra_y = \frac{\rho_\infty g \alpha_f K (T_w - T_\infty) y}{\mu a} \tag{12}$$

The dimensionless parameters, η, $f(\eta)$ and $\theta(\eta)$, are substituted into the governing equations and result in two ordinary differential equations:

$$f'' + \theta' = 0 \tag{13}$$

$$\theta'' - \frac{1}{2} f\theta' + = 0 \tag{14}$$

Through differentiation, integration, the application of the boundary conditions and the u-substitution method (as described in *Craft* [2008]), we solve the equations and determine the vertical velocity and temperature values as functions of the parameter $f'(\eta)$, which is equal to the dimensionless temperature $\theta(\eta)$:

$$v = \left[\rho_\infty g \alpha_f (T_w - T_\infty) K/\mu\right] f'(\eta) \tag{15}$$

$$T = f'(\eta)(T_w - T_\infty) + T_\infty \tag{16}$$

Figure 2 depicts the solution for $f'(\eta)$ as a function of η. Since vertical velocity and temperature are directly related to $f'(\eta)$, Figure 2 also describes the T and v profiles within the boundary layer.

[17] Equation (12) provides an important relationship of the boundary layer thickness, δ, to Ra_y. First, we assume that the boundary layer edge occurs where $\theta(\eta) = 0.01$, which means that the temperature is almost equal to that of the initial temperature far from the wall, T_∞. The value of η at $\theta(\eta) = f'(\eta) = 0.01$ is denoted as η_δ and rearranging equation (8) the relationship is expressed as:

$$\delta = x = \frac{\eta_\delta y}{Ra_y^{1/2}} \tag{17}$$

Thus, $\delta \sim yRa_y^{-1/2}$, and the Nusselt number Nu, a dimensionless number that describes the advective heat flux, scales as $Nu \sim y/\delta \sim Ra_y^{1/2}$ [*Bejan*, 1995]. From results shown in Figure 2, $\eta_\delta = 6.6$. Using this value for η_δ in equation (17), boundary layer thicknesses were calculated for the range of permeabilities from 10^{-14} to 10^{-8} m^2.

[18] An inherent assumption of the boundary layer theory is that the boundary layer thickness, δ, is much less than the height of the wall that represents the magma intrusion height, H. Typically the ratio, δ/H, at which the boundary layer theory is considered applicable, is around 0.1. Our analysis sets the acceptable ratio at 0.2 or less in order to provide estimates for a wider range of hydrothermal systems, although more exact analyses may be required to verify the boundary layer results for systems with δ/H ratios above 0.1.

[19] The boundary layer theory also assumes the system has reached a steady state. If one considers the development of fluid flow following rapid dike emplacement and one further assumes that the dike wall temperature is constant, two independent time scales emerge that place constraints on the applicability of the model. Rather than calculate these time scales exactly, we use a scale analysis approach. The time for steady state flow to establish, t_s, will be $\sim t_s = H/v$, which is the time required for fluid to move from the base of the hot wall to the surface. The assumption of constant wall temperature means that the time frame for steady state flow should be less than the time, τ, it would take for the dike to cool by conduction across through the intrusion's width. The conductive time scale is $\tau \sim d^2/a$, where d is the dike half-width and a is the thermal diffusivity. For conductive cooling of a vertical slab emplaced at temperature T_0 in an infinite medium at temperature T_∞, the wall temperature instantly falls to the mean temperature $(T_0 + T_\infty)/2$, and remains there until $\tau \approx 1$ [*Carslaw and Jaeger*, 1959]. Hence, the assumption of a constant wall temperature over the conductive time scale seems reasonable.

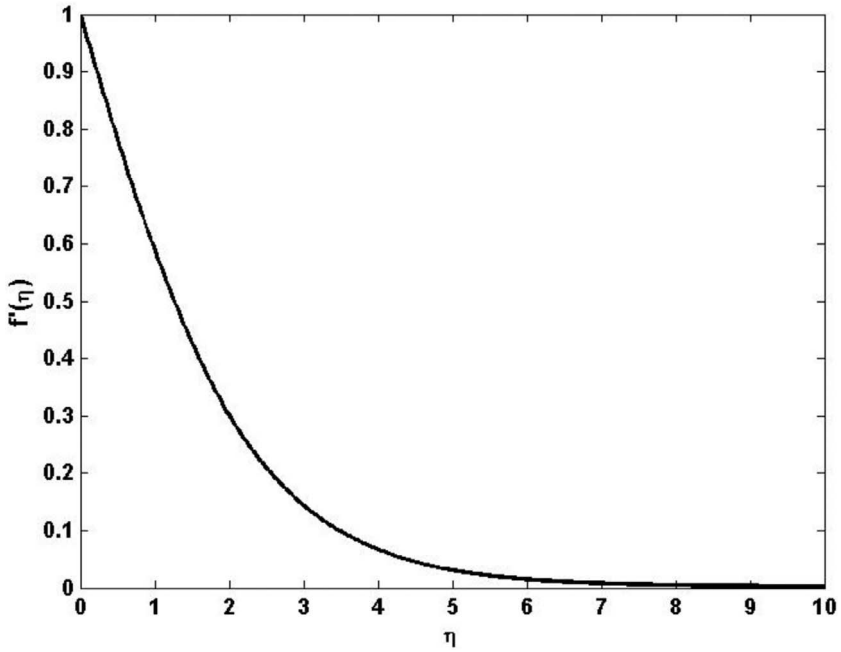

Figure 2. Similarity solution for $f'(\eta)$ as a function of η. The solution indicates the shape of the temperature and vertical velocity profiles within the boundary layer is shown, where distance from the hot wall increases as η increases.

[20] In this paper, we consider 1 km and 10 km tall dikes, which for typical crack aspect ratios of 10^{-2} to 10^{-3} [*Pollard*, 1987; L. N. Germanovich, personal communication, 2010] suggest maximum dike widths on the order of 10 and 100 m, respectively. In this study, we model one half of the dike and adjacent water saturated crust with 10 and 100 m dike half-widths. For thermal diffusivity equal to 10^{-6} m^2/s, $\tau \sim 3$ years and $\sim$300 years, respectively, for the assumed dike half-widths. We also consider a group of ten, 10 m half-width, 1 km tall dikes labeled as a 1 km tall, 100 m half-width dike system. The time for a dike system to reach steady state was then compared to the lifetimes to determine if steady state could be reached within the dike's lifetime for the different permeabilities. Combining results

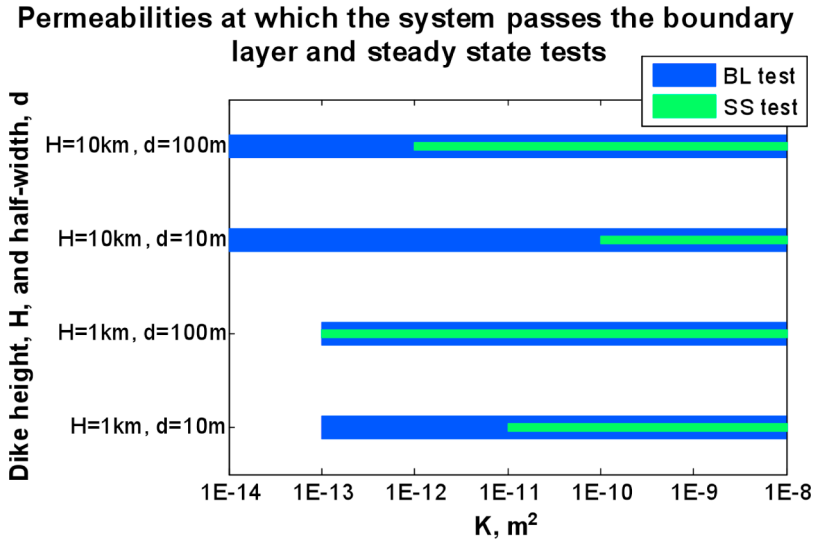

Figure 3. Determination of the permeabilities where boundary layer theory is applicable: The green bars indicate dike heights, half-widths and permeabilities where a system reaches a steady state before the heat from the magma intrusion conducts through the entire dike half-width. Blue shaded boxes indicate system permeabilities where boundary layer thickness is ≤ 0.2 of dike height. Two dike half-widths of 10 m or 100 m are considered for each dike height (1 km or 10 km). The 1 km tall, 100 m half-width represents a group of ten, 1 km tall, 10 m half-width dikes. We analyzed the systems that pass both the steady state and boundary layer tests, i.e., where the green and blue bars overlap.

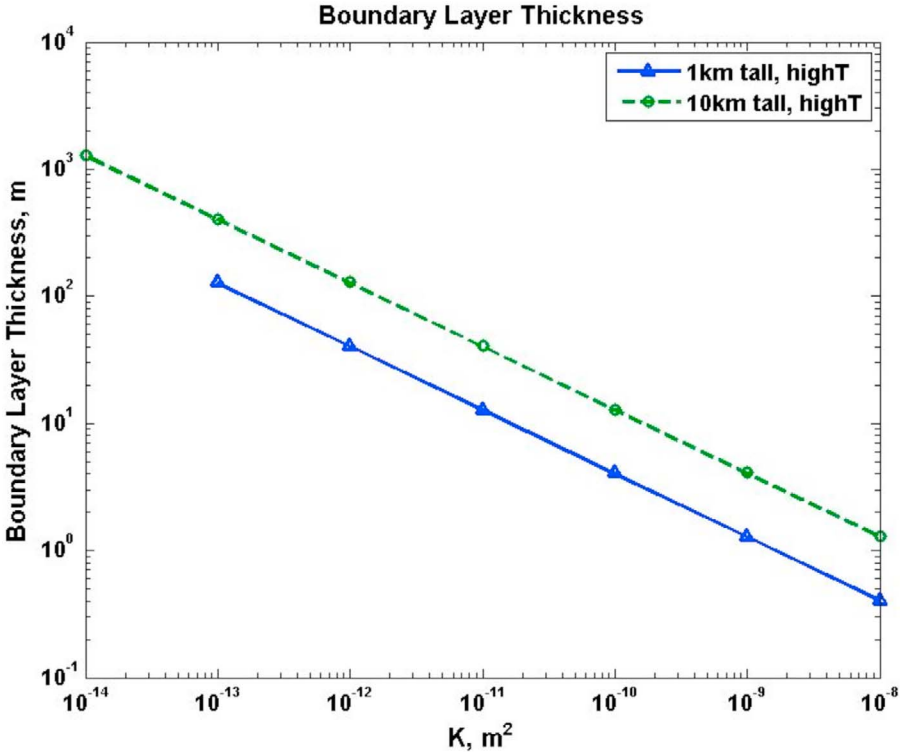

Figure 4. Boundary layer thicknesses for 1 and 10 km tall dikes where δ/D $\leq$ 0.2. The permeability range covers reasonable values for estimated terrestrial crust (K $\sim 10^{-9}$ m^2) and increased permeability due to impact fracturing (K $\leq 10^{-8}$ m^2) and for terrestrial mid-ocean ridge estimates and boundary layer theory applicability (K $\geq 10^{-14}$ m^2).

from the δ/H criterion with the criterion for reaching a steady state $t_s/\tau < 1$, we determined what permeabilities between 10^{-8} to 10^{-14} m^2 were appropriate in the context of the boundary layer theory. Results are shown in Figure 3.

[21] Temperatures and velocities were then calculated using equations (15) and (16). Next, we solved for total energy transport and fluid flux over the same range of permeabilities for a 1 km or 10 km tall magma intrusion. Energy transport was calculated by integrating the advective heat flux $\rho_f c_{p,f} v(x)T(x)$ across the width of the boundary layer, as shown in equation (18):

$$Q_{bl} = \int_0^{\delta} \rho_f v T c_f dx \tag{18}$$

where v and T are given by equations (15) and (16), respectively, and δ is given by equation (17).

[22] Volume flow rate per unit length of dike, Φ_{Vol}, was then calculated using equation (19):

$$\Phi_{Vol} = \int_0^{\delta} v dx \tag{19}$$

3. Results

3.1. Heat and Volume Flow Rates

[23] Boundary layer thicknesses were calculated using equation (17) for permeabilities between 10^{-14} to 10^{-8} m^2 and those having a δ/H ratio $\leq$ 0.2 are reported in Figure 4. As Figure 4 shows, boundary layer thickness, δ, is proportional to $K^{-1/2}$ as given by equations (12) and (17). Heat and fluid mass flow rates per unit length of the dike were then calculated for systems where boundary layer theory is applicable for magma intrusion heights of 1 km or 10 km. Mass flow was then converted to volume flow by dividing by the density. Although the fluid properties α_f and μ vary with temperature, they are assumed to be constant in this model. α_f increases and μ decreases about an order of magnitude each over the temperature range within the boundary layer; however, the mass and heat flow results obtained over the range of permeabilities include the effects of varying α_f and μ with temperature, at least in an average sense. We therefore apply the high temperature values of α_f and μ to calculate heat and fluid volume flow rates per length, recognizing that the results represent an upper estimate at a given permeability. Results are shown in Figures 5a and 5b. From these figures, one can note the apparent dependence of both heat and volume flow rates on permeability. Also, the relationship between volumetric flow rates per unit length of dike and parameters such as fluid temperature and crustal permeability can be found by replacing v in equation (19) with equation (15):

$$\Phi_{Vol} = \int_0^{\delta} \left[\rho_\infty g \alpha_f (T_w - T_\infty) K/\mu\right] f'(\eta) dx \tag{20}$$

which shows that $\Phi_{Vol} \sim Ra^{1/2}$.

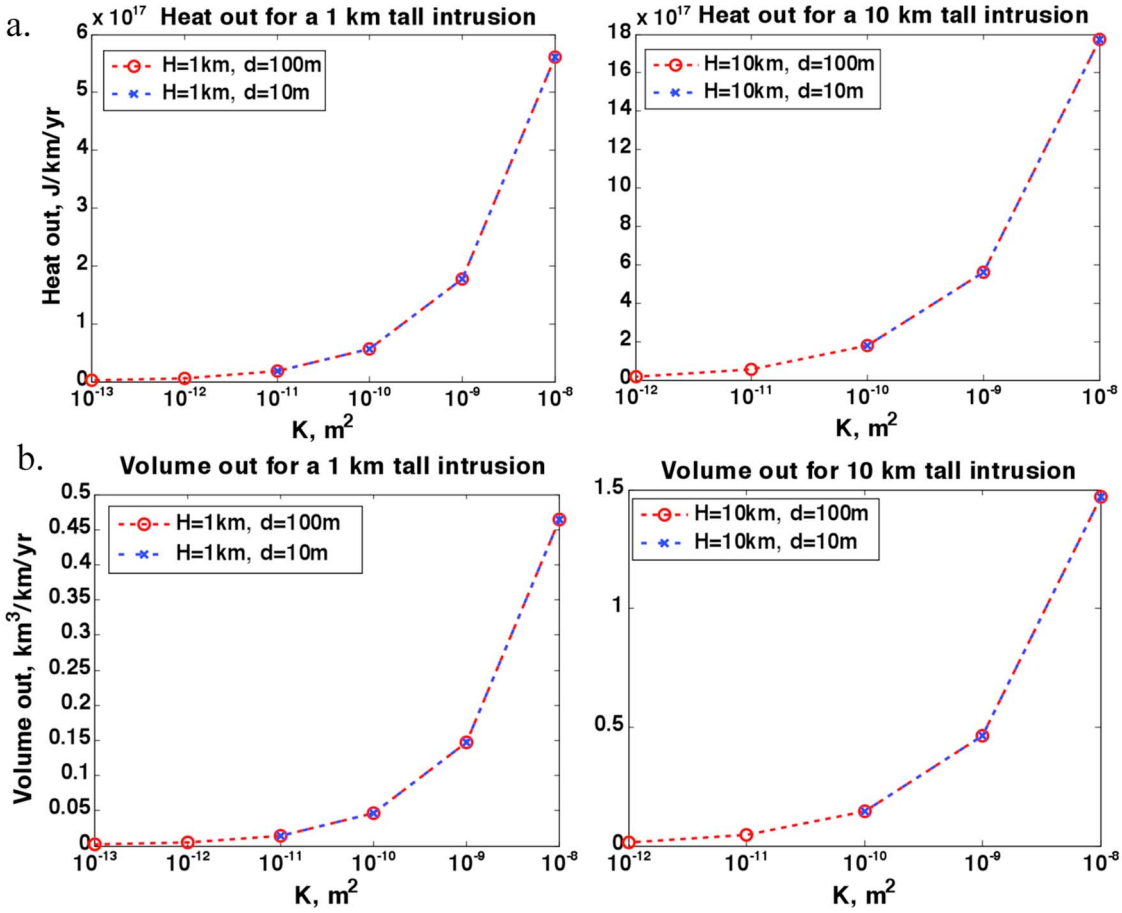

Figure 5. (a) Heat out per km and (b) volume flow rate out per km for 1 km and 10 km tall dikes with 10 m or 100 m half-widths over a range of Martian crustal permeabilities. The 1 km tall, 100 m half-width dike represents a group of ten 1 km tall, 10 m half-width dikes. Results are shown for permeabilities within the evaluated range, where boundary layer theory is applicable and where a steady state is reached in the system before the conduction lifetime limit of the dike(s) expires.

[24] Dike length can be multiplied by equation (20) to find volume flow rate along the dike and the dike's width determines the lifetime of the system and therefore the total volume output. On Mars, the dike swarms that have been identified with some certainty have lengths up to >3000 km [*Ernst et al.*, 2001]. Figures 5a and 5b show that a 1000 km long, 1 km tall and 10 m half-width magma intrusion injected into a permeable crust of 10^{-11} m^2 would produce $\sim 1.8 \times 10^{19}$ J/yr of heat and a volumetric flow of $\sim$15 km^3/yr. A 1000 km long, 10 km tall and 100 m half-width magma intrusion injected into a highly permeable crust of K = 10^{-11} m^2 would produce about 5.6×10^{19} J/yr of heat and a corresponding volumetric flow of $\sim$46 km^3/yr of fluid volume. At these fluid flow rates, total fluid volume production ranges between 45 and 13,800 km^3 over the 3 to 300 yearlong dike lifetimes that correspond to dikes between 10 and 100 m half-widths, respectively. The flow volume would be doubled considering the opposite side of the dike also produces an equal volume. The limit on the total volume of flow that results from circulation near the dike is controlled by the conductive lifetime of the dike derived from scale analysis in section 2.2. While additional fluid flow would occur after the dike has cooled beyond this time, our model does not take this into consideration because the volume of fluid would be small compared to that generated during the time when boundary layer theory is applicable.

3.2. Two-Phase Boundary Layer

[25] The boundary layer model invokes certain assumptions including that the system exists at steady state. Therefore, the decline in heat supplied by the magma intrusion as it cools over time is not considered, nor is the time required for the system to reach steady state. As a result, assuming steady state flow near an isothermal high-temperature wall overestimates the mass and heat fluxes. Another assumption inherent in boundary layer theory is that the fluid remains in the liquid phase. The critical pressure of 221 bars for pure water is reached at a depth of about 2 km beneath the Martian surface assuming an overlying layer of fractured basalt with a density around 2.8 kg/m^3 and fluid temperatures of 4°C or higher. As long as the dike exists below this depth, the adjacent fluid will always be in either the liquid or supercritical phase. However, if a portion of the dike is above the critical depth there will be a layer of vapor next to the hot dike. The enhanced heat transport resulting from boiling and transport of high enthalpy vapor

may be important during the early phase of hydrothermal circulation before the magma body has cooled significantly. Moreover, evidence suggests the groundwater on Mars is likely to be saline [*Grotzinger et al.*, 2005; *Bridges and Grady*, 2000] and two-phase flow in a saline fluid may affect the dynamics of heat and mass transport [e.g., *Lewis and Lowell*, 2009a, 2009b; *Coumou et al.*, 2009].

[26] The thickness of a vapor layer can be estimated by applying a local similarity approach, defined by *Parmentier* [1979] as:

$$\delta_v = 2\gamma\left(\frac{\xi a y_v}{Kg\rho_v}\right) \tag{21}$$

where δ_v is the layer thickness of the vapor, ξ is the dynamic viscosity of steam, γ_v is the height above the critical depth for liquid/vapor water, ρ_v is the density of the vapor, and γ is a value such that heat flux is conserved across the vapor-water interface. In this model $\gamma \approx 1$ [*Parmentier*, 1979]. In applying equation (21) for permeabilities where boundary layer is applicable, a dike that reaches a depth of 1 km below the surface (i.e., has 1 km of dike above the critical pressure depth) will have a vapor layer thickness at the top of the dike of about 7 m for $K = 10^{-11}$ m^2 and 0.2 m for $K = 10^{-8}$ m^2. If the dike reaches a depth of 100 m below the surface, the vapor layer will be 79 m thick for $K = 10^{-12}$ m^2 and 0.8 m for $K = 10^{-8}$ m^2. For a 1 km tall dike system 100 m below the surface, the vapor layer may prove significant, as the overall boundary layer thickness is smaller for the shorter dike. For shorter dikes and high permeability systems, the boundary layer analysis provides a good estimate of vapor layer thickness compared to numerical models with cell sizes larger than the layer thickness [e.g., *Gulick*, 1998]. Also, even for a dike entirely below 2 km, as high temperature water moves up to the surface the decrease in pressure may cause boiling. Therefore, some fluid may be released at the surface as steam or the vapor may cool back to the liquid phase before reaching the surface and contribute to the liquid flux there. Released vapor may condense and carve flow type features on the Martian surface or the steam may build up beneath the surface and could lead to phreatic eruptions, in a similar fashion to those suggested to occur on Earth [*Germanovich and Lowell*, 1995]. Pit craters, possible evidence of phreatic eruptions, have been observed on Mars [e.g., *Banerdt et al.*, 1992; *Wyrick et al.*, 2004].

3.3. Additional Source of Fluid—Ice Melt

[27] There is evidence of water ice beneath the surface on Mars [e.g., *Clifford*, 1993; *Baker*, 2001; *Plaut et al.*, 2007] of which a magma intrusion could melt and cause contribution of additional fluid to the system. We investigated a layer of ice or permafrost overlying our previously described dike driven hydrothermal system to estimate the volume of fluid that could be provided. Previous studies on the melting of permafrost include *Gulick* [1998], *McKenzie and Nimmo* [1999], *Harrison and Grimm* [2002], *Travis et al.* [2003] and *Ogawa et al.* [2003]. *Gulick* [1998] provided quantitative estimates for fluid flow from ice melt and investigated the energy and time required to melt through a 2 km thick permafrost layer by applying the energy supplied by the hydrothermal system and compared results to the energy required to change the ice to liquid phase. *McKenzie and Nimmo* [1999] calculated the volume of ice that could be melted as a result of conductive heat transfer from a large magmatic dike in an effort to explain flood features observed on the Martian surface. *Harrison and Grimm* [2002] calculated the time for circulating fluid next to a sill magma intrusion to melt through a 1 km thick overlying permafrost layer and predicted discharge volumes. *Travis et al.* [2003] modeled hydrothermal circulation driven by background geothermal heating beneath a permafrost layer and determined the layer's thickness as a function of location. *Ogawa et al.* [2003] considered a sill magma intrusion modeled as a constant temperature base that transferred heat to the permafrost through conduction and later by convection. The principal difference between the boundary layer analyses and *Gulick*'s [1998] analyses of ice melt stems from the relatively short lifetime of a dike compared to the intrusion assumed by Gulick as well as the fact that the boundary layer analysis investigates a range of crustal permeabilities compared to *Gulick* [1998] varying the porosity. Our ice melt model differs from *McKenzie and Nimmo* [1999] in that our model considers convective heat transfer to the base of the ice layer while *McKenzie and Nimmo* [1999] only consider conductive heat transfer. Also, the *Harrison and Grimm* [2002] model differs from ours in that the meltwater is incorporated into the hydrothermal circulation and the magma intrusion becomes permeable as it cools through its brittle-ductile transition. The *Travis et al.* [2003] and *Ogawa et al.* [2003] analyses differ from ours by considering convection within the water melt layer. Also, *Ogawa et al.* [2003] set a constant temperature at the base of the ice layer as opposed to the heat flux our model applies.

[28] Figure 6 shows the system configuration with the dike embedded in water-saturated Martian crust and overlain by a layer of permafrost. The permafrost thickness of ~2–3 km is set based on estimations of ice thickness on Mars [e.g., *Clifford*, 1993] and that for water to remain above the critical pressure of water the depth must be greater than ~2 km based on lithostatic pressure. *Clifford* [1993], who follows the lunar scale used by *Binder and Lange* [1980], suggests that the maximum depth of porous crust (where porosity > 0.01) on Mars is not likely to be greater than 11 km. *Clifford* [1993] states, however, that assuming 1 kbar to be the closure pressure is conservative considering that laboratory experiments show that fractures and pore space may be open at pressures of ~5–10 kbar [*Gold et al.*, 1971; *Todd et al.*, 1973; *Siegfried et al.*, 1977]. Therefore, circulation may be possible at greater than 11 km below the surface. Moreover, "wet" crust could retain open pore space to a depth up to about 1/3 greater than the estimated "dry crust" value of 11 km [*Hubbert and Rubey*, 1959; *Byerlee and Brace*, 1968; *Brace and Kohlstedt*, 1980; *Thompson and Connolly*, 1992], although this effect would likely only be significant at great depths on Mars where there are high temperatures and pressures [*Maxwell*, 1964; *Pettijohn*, 1975]. Higher heat flow in the Martian past [*Toksöz and Hsui*, 1978; *Davies and Arvidson*, 1981; *Schubert and Spohn*, 1990] could have provided conditions for a wetter crust with porosity at depth. We consider 1 and 10 km tall dikes beneath a maximum of 3 km of permafrost. The maximum depth of the hydrothermal system would therefore be at ~13 km and it is not unreasonable to assume that permeable crust exists to that depth at least in the Martian past.

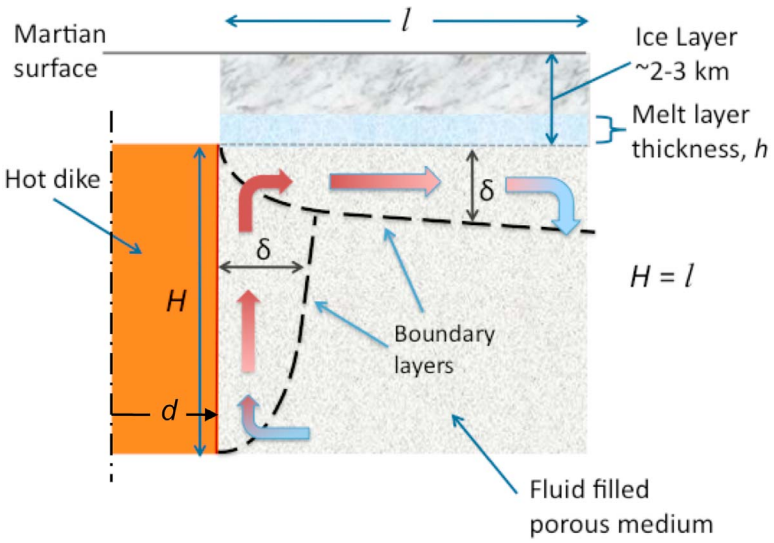

Figure 6. Ice layer overlying a Martian, magma driven hydrothermal system. Bold arrows indicate the circulation of fluid beneath the surface. Bold dashed lines denote the edge of a boundary layer with a thickness of δ. For this model, dimension l is the width of the ice layer and is equal to the height, H, of the dike intrusion. Over time a melt layer of thickness, h, forms within the ice layer.

[29] In the scenario shown in Figure 6, as the vertical boundary layer adjacent to the dike wall reaches the permafrost layer, the fluid turns and flows horizontally, cools and eventually sinks to form a complete circulation cell. The laterally flowing fluid beneath the permafrost can also be approximated as a thermal boundary layer across which heat is transferred by conduction to the overlying permafrost. Dashed black lines in Figure 6 denote the two boundary layers with the boundary layer at the base of the ice providing a heat source to the overlying ice layer. Variable definitions are given in Table 2. The total energy per length, Q_{ice}, at the base of the ice layer supplied by the vertical boundary layer over a time, τ_i, is expressed as:

$$Q_{ice} = \rho_{f,w} c_{p,f} \langle T \rangle \langle v \rangle \delta \tau_i \tag{22}$$

where $\rho_{f,w}$ is the density of water, $c_{p,f}$ is the specific heat of water, $\langle T \rangle$ is the average temperature across the vertical boundary layer of thickness δ, and $\langle v \rangle$ is the average velocity across the boundary layer. If the temperature of the overlying ice layer is at the melt temperature, then, to a first approximation, the heat energy from equation (22) melts the ice and heats the resulting water-rock mixture. Assuming a constant porosity, Φ, a horizontal dimension, l, of the horizontal boundary layer, and a thickness of the melt layer, h, over a certain time, τ_i, the heat taken up by the ice per length is written as:

$$Q_m = \left((\rho c)_m \Delta T_m + \phi \rho_i L \right) lh(\tau_i) \tag{23}$$

where $(\rho c)_m$ is the heat capacity of the water-rock mixture, ρ_i is the density of ice, L is the latent heat of fusion of ice, and ΔT_m is the temperature difference across the permafrost layer. The water-rock mixture heat capacity is defined as:

$$(\rho c)_m = \rho_{f,w} c_{p,f} \phi + \rho_r c_{p,r} (1 - \phi) \tag{24}$$

where ρ_r is the density of the rock and $c_{p,r}$ is the specific heat of the rock. If we assume the permafrost layer is at the melting temperature of ice, $\Delta T_m = 0$ and equation (23) reduces to:

$$Q_m = \phi \rho_i L hl(\tau_i) \tag{25}$$

Table 2. Definition of Variables for Overlying Ice Layer Analyses

Symbol	Definition	Value	Units
h	Thickness of melt layer	Equation (26) for given τ_i	m
L	Latent heat of fusion for ice	3.33×10^5	J kg^{-1}
l	Horizontal dimension beneath ice layer	1 or 10	km
Q_{ice}	Heat flow per length at base of ice layer	Equation (22)	kJ m^{-1}
Q_m	Heat flow per length of water-ice mixture	Equation (25)	kJ m^{-1}
ΔT_m	Temperature difference across ice layer	0	°C
$(\rho c)_m$	Heat capacity of water-ice mixture	Equation (24)	kJ m^{-3} °C^{-1}
$\rho_{f,w}$	Density of water at room temperature and pressure	1000	kg m^{-3}
ρ_i	Density of ice	916.7	kg m^{-3}
ρ_r	Density of the rock	3000	kg m^{-3}
τ_i	Time	Varies	s
ϕ	Porosity	0.1	unitless

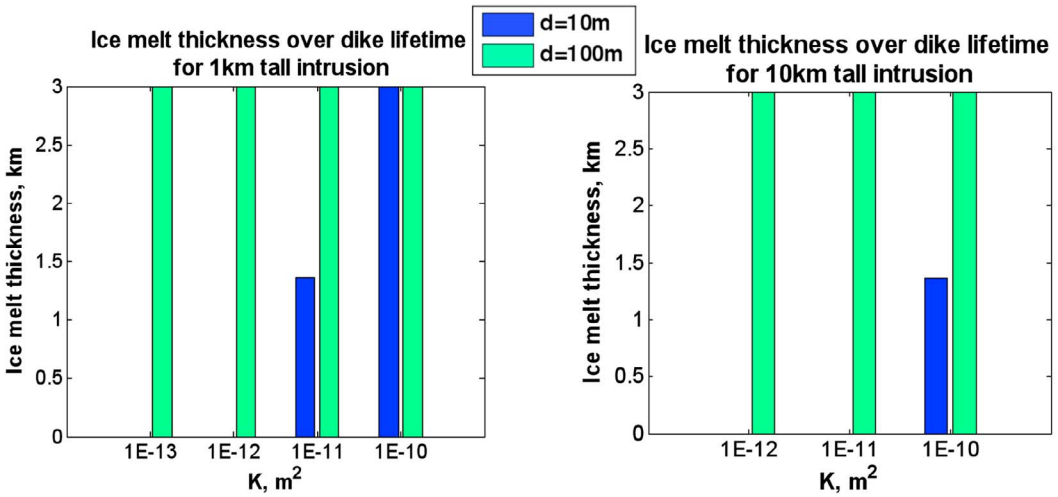

Figure 7. Ice layer thickness melted over the dike lifetime for permeabilities within the range of $10^{-14} \leq K \leq 10^{-10}$ m^2 where the system reaches steady state before the dike conductively cools and where the boundary layer thickness is ≤ 20% of the dike height. The 1 km tall, 100 m half-width dike represents a group of ten 1 km tall, 100 m half-width dikes.

Combining equations (22) and (25) by setting $Q_{ice} = Q_m$, we can determine the relationship of melt thickness, h, and time, τ_i:

$$h = \frac{\tau_i \rho_f c_{p,f} \langle T \rangle \langle v \rangle \delta}{\phi \rho_i L l} \tag{26}$$

This approach follows the description of melting in section 11.3 of *Carslaw and Jaeger* [1959] excluding the higher order terms that have minimal effect on the resulting melt thickness.

[30] Equation (26) provides an upper estimate of the melt thickness produced, as all the heat transferred from the boundary layer goes into melting the ice and none into heating the rock. As the ice melts, we assume the water flows away and the boundary layer migrates upwards through the crust, or the ice migrates downward to maintain contact. If a glacial layer of pure ice is considered instead of permafrost, the value of Φ would be 1, and the thickness melted for a given time, τ_i, will decrease, yet the volume of meltwater produced will remain the same.

[31] If the ice layer melts through to the surface, the meltwater will contribute to the volume of water released, helping to form the fluvial features observed on Mars. The melting of the ice layer may also contribute to destabilizing the crust and could result in surface flows of rock-meltwater mixture, subsidence of the surface, fracturing, and drops in pressure as the fluid melts through to the surface and leaves the system [*Wilson and Head*, 2002]. The amount of ice melted over the lifetime of a dike depends on the dike height, width and temperature, the viscosity and thermal expansion coefficient values, and the crustal permeability. Figure 7 displays ice layer thickness melted over the dike lifetime calculated for a slightly more conservative range of permeabilities of $10^{-14} \leq K \leq 10^{-10}$ m^2. The results show that a 1 km tall, 10 m half-width dike with $K = 10^{-11}$ m^2 or a 10 km tall, 10 m half-width dike with $K = 10^{-10}$ m^2 can each melt about 1.4 km of the overlying ice layer over the 3 year lifetime. For a 1 km tall, 10 m half-width dike with $K = 10^{-10}$ m^2 and for 100 m half-width dikes of either 1 or 10 km in height, and with any permeability where boundary layer theory is applicable, the entire 2 – 3 km of overlying ice can be melted over about 2 years for the 10 m half-width dike or 70 years or less for the 100 m half-width dikes, depending on permeability. Melt volume produced, however, will vary between 1 km and 10 km tall dikes as the basal heating length is assumed equal to the dike height.

4. Discussion

4.1. Comparison With Earlier Model

[32] *Gulick* [1998] considered a similar Martian hydrothermal system using the program SUTRA [*Voss*, 1984] to study circulation driven by cylindrical magma chambers of different volumes. *Gulick* [1998] determined that the maximum discharge mass flow rate for a 4 km tall magma chamber 2 km below the surface, with a volume of 50 km^3, initial temperature of 1250°C, and adjacent medium permeability of 10^{-11} m^2 was just less than 3,000 kg/s after about 600 years. Assuming that the fluid flow occurs symmetrically around the ∼12.6 km circumference of the intrusion and using an estimated boundary layer thickness from Figure 2 in *Gulick* [1998] of 1.25 km, the resulting mass flux equals about 1.8×10^2 kg/km^2/s. To compare, we used the boundary layer theory to calculate volume mass flow rates for a dike of similar length and height to *Gulick's* intrusion circumference and height, respectively. Boundary layer analysis of a 5 km tall, 12 km long, 50 m half-width constant temperature wall (dike intrusion) at 600°C with an adjacent medium permeability of 10^{-11} m^2 resulted a mass flow rate of ∼13,000 kg/s and a mass flux of $\sim 3.6 \times 10^4$ kg/km^2/s along the length of the dike.

[33] Comparison between the boundary layer analysis and *Gulick*'s [1998] results is not ideal, but provides a relevant point of reference. The boundary layer model appears to result in significantly higher flow rates than *Gulick* largely as

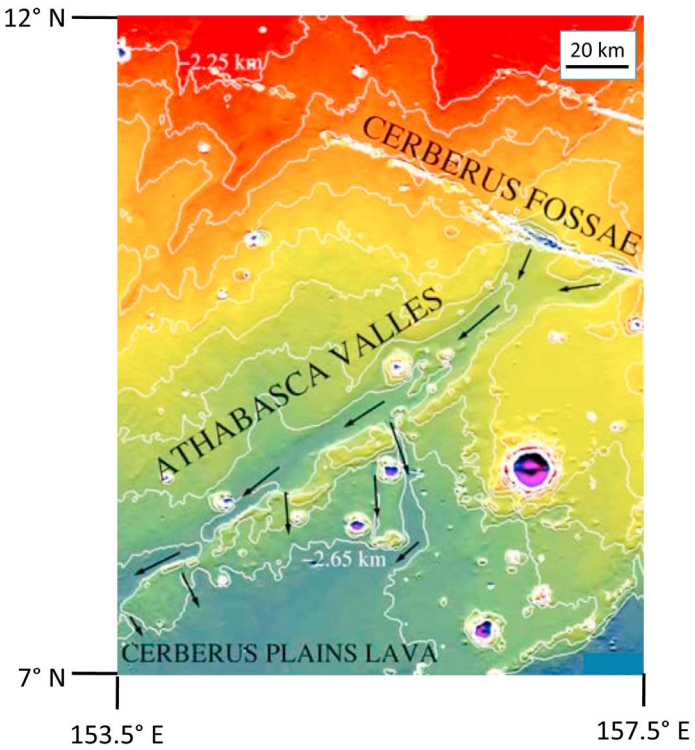

Figure 8. MOLA topography between 7° and 12° N, 153.5° and 157.5° E, interpolated to 256 pixels per degree using the methods of *Abramov and McEwen* [2004] showing the suggested source Cerberus Fossae fissure with Athabasca Valles to the southwest. Figure modified from *Burr et al.* [2002a]. Arrows indicate suggested direction of fluid flow during valley formation.

a result of the different boundary conditions at the intrusion interface in the two models. *Gulick's* time dependent circulation model assumes that the hydrothermal circulation is driven by a prescribed heat flux across the intrusion wall that decreases with time as the intrusion cools. As a result of this condition, the "spin up" time is considerable and the flow rate reaches its peak after the heat flux from the intrusion has decreased substantially. On the other hand, boundary layer theory assumes a constant temperature wall and, hence, the dike acts as an infinite heat reservoir to drive hydrothermal circulation in the boundary layer over its conductive lifetime. The flow rates derived from our steady state boundary layer model, therefore, provide an upper estimate for the flow rate near the vertical wall of an intrusion.

[34] Also, using the boundary layer analysis to estimate peak flow rates for larger intrusion thicknesses such as those investigated by *Gulick* [1998] is reasonable as the conductive time scale is so long. For the 4 km tall, 4 km diameter intrusion discussed by Gulick, the conductive time scale is $\sim 5 \times 10^5$ yr. For such an intrusion, the wall temperature remains essentially constant over the time required for the system to reach the maximum fluid flow rate. Therefore, the boundary layer analysis provides a realistic maximum flow rate estimate.

4.2. Comparison to Athabasca Valles

[35] The boundary layer model provides a reasonable first order estimate of the heat and fluid flow rates that can be expected for a Martian hydrothermal system driven by a dike-like magmatic intrusion. Comparison of these fluid flow rates to those estimated for certain surface morphology on Mars can indicate whether the hydrothermal system could be a feasible mechanism for their formation. For example, the outflow channel system, Athabasca Valles (Figure 8), appears to emanate from one of the fissures of Cerberus Fossae. Based on the fissures' morphology and studies by *Mège and Masson* [1996], *Burr et al.* [2002a] and *Head et al.* [2003], the fissures may have resulted from subsidence caused by volcanic dike intrusions. Also, a recent investigation by *Roberts et al.* [2012] suggests that geologically young boulder tracks observed in the Cerberus Fossae region indicate the recent occurrence of marsquakes and possibly volcanic activity. The intrusions may have then caused the release of subsurface groundwater/melted ice to form Athabasca Valles [e.g., *Burr et al.* 2002a; *Head et al.*, 2003]. A recent study by *Hurwitz and Head* [2012] suggests a combination of fluid flow and subsequent magma flow formed the valley. Here we only consider the water flow required to form the valley system.

[36] The source fissure for Athabasca Valles appears to be about 1000 m wide and 200 km long, though the width was likely widened by erosion and mass wasting over time [*Hanna and Phillips*, 2006]. *Hanna and Phillips* [2006] suggest an initial fissure width of 200 to 500 m. Estimates based on MOLA (Mars Orbiter Laser Altimeter) topography of the fluid flow volume to form Athabasca range from 400 km^3 to 1600 km^3 [*Hanna and Phillips*, 2006]. Upper limit flow rate estimates based on the

geomorphology of Athabasca Valles range from about 300 to 3 × 10^5 km^3/yr [*Burr et al.*, 2002a, 2002b, 2004; *Mitchell et al.*, 2005].

[37] In applying the boundary layer model to address the formation of Athabasca Valles, we note that, as mentioned previously, dikes typically have a width to height aspect ratio of 10^{-2} to 10^{-3}. Hence, a 10 km tall dike would not typically be much wider than ∼100 m. If such a dike, 200 km long, 100 m half-width intruded at Cerberus Fossae into a region where crustal permeability was ∼10^{-11} m^2, hydrothermal flow would produce ∼10 km^3/yr of fluid and approximately 3000 km^3 of fluid would be produced over the ∼300 year lifetime of the dike. Consideration of the equivalent system on the opposite side of the dike would double the flow volume. According to the estimate for volume required to form Athabasca Valles, the volume produced by one 10 km tall, 100 m half-width dike is adequate, although the flow rate of 10 km^3/yr is considerably below the required minimum rate of 300 km^3/yr. Ten km tall, 100 m half-width dike systems with K ≥ 10^{-12} m^2 can also produce fluid volumes within the range required, however for K ≤ 10^{-13} m^2 multiple dikes and/or flow from both sides of the dike are necessary. A flow rate comparable to that estimated for forming Athabasca Valles could be achieved if fluid resulting from hydrothermal circulation near a dike is first stored in a lake type reservoir and then released episodically or gradually over a period ranging from a couple of days to ∼ a year.

[38] To store 400 km^3 - 1600 km^3 would require an area beside the dike of between 500 km^2 to 2000 km^2 assuming a 2 km thick permafrost rocky-ice layer with porosity of 0.4. However, to allow for high rate outflows, we assume a subsurface lake with a depth of 2 km. The area required for lake storage to form Athabasca Valles would range from 200 km^2 to 800 km^2. For water drawn locally from around the 200 km length of the source fissure, the reservoir would have extended 1 to 4 km away, respectively, or half that distance for flow from both sides of the dike. Large glacial floods called jökulhlaups have occurred in Iceland and in the channeled scablands of western Washington where the ice acts as a trap for melted fluid that is released episodically by volcanic activity [*Carrivick et al.*, 2004]. *Weis and Newman* [1976] estimate reservoir volumes for the scabland floods at 16.8 km^3 and *Old et al.* [2005] estimate Icelandic jökulhlaup volume flows at about 0.23 km^3 per episode. The volumes are much lower than those needed to form Athabasca Valles, however volcanoes and fluvial channels on Mars are much larger than those on Earth and therefore flood mechanisms similar to jökulhlaups on a larger scale may not be unreasonable.

[39] Melting an overlying ice or permafrost layer would increase the fluid volume available for forming surface features. Our calculations show that the fluid melted by a 10 km tall, 200 km long dike system with a 2 – 3 km thick overlying permafrost layer with 10% porosity equals about 400 to 600 km^3 supplied over 45–70 years. This ice melt fluid could therefore contribute a significant volume toward the 400 to 1600 km^3 range required for forming Athabasca Valles.

[40] *Hanna and Phillips* [2006] suggest an alternative mechanism for supplying fluid to the surface through tectonic pressurization of an instantaneous dike emplacement. Their model results estimate fluid flow rates ranging from 8.9 × 10^4 m^3/s to 9.5 × 10^5 m^3/s which fall within the flow rates suggested by *Burr et al.* [2002a, 2002b] and *Mitchell et al.* [2005]. However, this nearly instantaneous dike intrusion stress induction does not take into account the time required for a dike to propagate from depth to the near surface. Dikes are typically emplaced at a rate of ∼1 m/s [*Linde et al.*, 1993; *Klein et al.*, 1977]. At this rate, it would take ∼2.8 h to emplace a 10 km tall dike and the stress field around the dike would evolve on a similar time scale. Consideration of this propagation time may result in a lower rate of fluid flow associated with dike emplacement than estimated by *Hanna and Phillips* [2006].

[41] Overall, a dike driven hydrothermal system at Cerberus Fossae appears able to supply the required volume of water to form Athabasca Valles provided the water can collect in a reservoir and be released suddenly. Ice melt is not required, yet could contribute a significant volume to the system and enable lower permeability systems as formation mechanisms. Further work to determine whether magma-driven hydrothermal fluid flow could be a feasible mechanism for the formation of other surface features is needed.

5. Summary

[42] The boundary layer method applied here to a dike-driven hydrothermal system beneath the surface of Mars provides reasonable quantification of the upper limit for heat and fluid outputs for a range of possible crustal permeabilities, dike heights of 1 or 10 km and varying dike lifetimes based on half-widths of 10 m, 100 m, or a group of dikes. Model results estimate that hydrothermal convection near a 1000 km long, 1 km tall and 10 m half-width dike-like intrusion injected into crust with a permeability of 10^{-11} m^2 would yield ∼1.8 × 10^{19} J/yr of heat and a fluid flow rate of ∼15 km^3/yr. A similar 10 km tall and 100 m half-width magma intrusion could generate about 5.6 × 10^{19} J/yr of heat and ∼46 km^3/yr of fluid flow. At these fluid flow rates, total fluid volume production can range between 45 and 13,800 km^3 over the 3 to 300 yearlong dike lifetimes that correspond to dikes between 10 and 100 m half-widths.

[43] When comparing our flow rate results with the maximum rates of *Gulick* [1998] for a 50 km^3 magmatic intrusion, the boundary layer model predicts a mass flow rate just over 4 times higher. This result mainly reflects the difference between the boundary conditions at the intrusion wall in the two models. Boundary layer theory assumes a constant wall temperature, whereas *Gulick* [1998] assumes a prescribed heat flux that decreases with time. The assumption of a constant temperature wall over the short dike lifetime of years to hundreds of years is reasonable since a 50 km^3 magmatic intrusion similar to *Gulick's* cools only very slightly in this time.

[44] Boiling near the dike for the shorter dike systems may significantly lower the water flow output to the surface. The vapor may still contribute to surface feature formation, however, by causing phreatic eruptions or surface subsidence. Boundary layer calculations find that for most of the crustal permeabilities and dike sizes considered, hydrothermal convection could melt a 2 – 3 km thick permafrost layer or an equivalent volume of pure ice beneath the Martian surface during the lifetime of the dike.

[45] The fluid flow rates predicted from the boundary layer models for 1 to 10 km tall, 200 km long dikes with 10^{-11} m^2 permeability, ≈3–10 km^3/yr, respectively. These rates are much less than the estimated 300 to 3×10^5 km^3/yr needed to produce outflow channels such as the Athabasca Valles; yet, the total fluid volume of 3,000 km^3 over a 100 m half-width dike lifetime of 300 years surpasses the 400 to 1600 km^3 volume believed necessary. Model results indicate that if fluid could be stored in a near surface reservoir until later episodic release(s), the flow rate could achieve levels sufficient to form the channel system. An overlying, near surface ice layer may help contain the reservoir until melted through, and water melted from the ice layer could contribute significantly to the fluid flow volume.

[46] **Acknowledgments.** We thank the Associate Editor, an anonymous reviewer and Oleg Abramov for their constructive criticisms and insights. This research was supported in part by NASA grant NNX10AO38G to R.P.L., a Virginia Space Grant Award to K.L.C. and the Virginia Tech Multicultural Awards and Opportunities Program funding to K.L.C.

References

Abramov, O., and D. A. Kring (2005), Impact-induced hydrothermal activity on early Mars, *J. Geophys. Res.*, *110*, E12S09, doi:10.1029/2005JE002453.

Abramov, O., and A. S. McEwen (2004), An evaluation of interpolation methods for MOLA data, *Int. J. Remote Sens.*, *25*(3), 669–676, doi:10.1080/01431160310001599006.

Baker, V. R. (2001), Water and the Martian landscape, *Nature*, *412*, 228–236, doi:10.1038/35084172.

Baker, V. R., R. G. Strom, V. C. Gulick, J. S. Kargel, G. Komatsu, and V. S. Kale (1991), Ancient oceans, ice sheets and the hydrological cycle on Mars, *Nature*, *352*, 589–594, doi:10.1038/352589a0.

Baker, V. R., M. H. Carr, V. C. Gulick, C. R. Williams, M. S. Marley (1992), Channels and valley networks, in *Mars*, edited by H. H. Kieffer et al., pp. 493–522, Univ. of Ariz. Press, Tucson.

Banerdt, W. B., M. P. Golombek, and K. L. Tanaka (1992), Stress and tectonics on Mars, in *Mars*, edited by H. H. Kieffer et al., pp. 249–297, Univ. of Ariz. Press, Tuscon.

Barnhart, C. J., F. Nimmo, and B. J. Travis (2010), Martian post-impact hydrothermal systems incorporating freezing, *Icarus*, *208*, 101–117, doi:10.1016/j.icarus.2010.01.013.

Baross, J. A., and S. E. Hoffman (1985), Submarine hydrothermal vents and associated gradient environments as sites for the origin and evolution of life, *Orig. Life*, *15*, 327–345, doi:10.1007/BF01808177.

Bejan, A. (1995), *Convection Heat Transfer*, 2nd ed., 639 pp., Wiley, New York.

Bibring, J.-P., et al. (2004), OMEGA: Observatoire pour la Minéralogie, l'Eau, les Glaces et l'Activité, in *Mars Express: The Scientific Payload*, edited by A. Wilson, pp. 37–49, ESA Publ. Div., Noordwijk, Netherlands.

Binder, A. B., and M. A. Lange (1980), On the thermal history, thermal state and related tectonism of a moon of fission origin, *J. Geophys. Res.*, *85*, 3194–3208, doi:10.1029/JB085iB06p03194.

Brace, W. F., and D. L. Kohlstedt (1980), Limits on lithospheric stress imposed by laboratory experiments, *J. Geophys. Res.*, *85*, 6248–6252, doi:10.1029/JB085iB11p06248.

Brakenridge, G. R., H. E. Newsom, and V. R. Baker (1985), Ancient hot springs on Mars: Origins and paleoenvironmental significance of small Martian valleys, *Geology*, *13*, 859–862, doi:10.1130/0091-7613(1985)13<859:AHSOMO>2.0.CO;2.

Bridges, J. C., and M. M. Grady (2000), Evaporite mineral assemblages in the nakhlite (Martian) meteorites, *Earth Planet. Sci. Lett.*, *176*, 267–279, doi:10.1016/S0012-821X(00)00019-4.

Burr, D. M., A. S. McEwen, and S. E. H. Sakimoto (2002a), Recent aqueous floods from the Cerberus Fossae, Mars, *Geophys. Res. Lett.*, *29*(1), 1013, doi:10.1029/2001GL013345.

Burr, D. M., J. A. Grier, A. S. McEwen, and L. P. Keszthelyi (2002b), Repeated aqueous flooding from the Cerberus Fossae: Evidence for very recently extant, deep groundwater on Mars, *Icarus*, *159*, 53–73, doi:10.1006/icar.2002.6921.

Burr, D. M., P. A. Carling, R. A. Beyer, and N. Lancaster (2004), Flood-formed dunes in Athabasca Valles, Mars: Morphology, modeling, and implications, *Icarus*, *171*, 68–83, doi:10.1016/j.icarus.2004.04.013.

Byerlee, J. D., and W. F. Brace (1968), Stick-slip stable sliding and earthquakes: Effect of rock type, pressure, strain rate and stiffness, *J. Geophys. Res.*, *73*, 6031–6037, doi:10.1029/JB073i018p06031.

Carrivick, J. L., A. J. Russell, F. S. Tweed, and D. Twigg (2004), Paleohydrology and sedimentary impacts of jokulhlaups from Kverkjoukull, Iceland, *Sediment. Geol.*, *172*, 19–40, doi:10.1016/j.sedgeo.2004.07.005.

Carslaw, H. S., and J. C. Jaeger (1959), *Conduction of Heat in Solids*, 2nd ed., Clarendon Press, Oxford, U. K.

Cheng, P., and W. Minkowycz (1977), Free convection about a vertical flat plate embedded in a porous medium with application to heat transfer from a dike, *J. Geophys. Res.*, *82*, 2040–2044, doi:10.1029/JB082i014p02040.

Christensen, P. R., et al. (2001), Mars Global Surveyor Thermal Emission Spectrometer experiment: Investigation description and surface science results, *J. Geophys. Res.*, *106*, 23,823–23,871, doi:10.1029/2000JE001370.

Christensen, P. R., et al. (2004), The Thermal Emission Imaging System (THEMIS) for the Mars 2001 Odyssey mission, *Space Sci. Rev.*, *110*, 85–130, doi:10.1023/B:SPAC.0000021008.16305.94.

Clifford, S. M. (1993), A model for the hydrologic and climatic behavior of water on Mars, *J. Geophys. Res.*, *98*, 10,973–11,016, doi:10.1029/93JE00225.

Coumou, D., T. Driesner, P. Weis, and C. A. Heinrich (2009), Phase separation, brine formation, and salinity variation at Black Smoker hydrothermal systems, *J. Geophys. Res.*, *114*, B03212, doi:10.1029/2008JB005764.

Craddock, R., and T. Maxwell (1993), Geomorphic evolution of the Martian highlands through ancient fluvial processes, *J. Geophys. Res.*, *98*, 3453–3468, doi:10.1029/92JE02508.

Craft, K. L. (2008), Boundary layer models of hydrothermal circulation on Earth and Mars, M.S. thesis, Ga. Inst. of Technol., Atlanta.

Davies, G. F., and R. E. Arvidson (1981), Martian thermal history, core segregation and tectonics, *Icarus*, *45*, 339–346, doi:10.1016/0019-1035(81)90039-7.

Edmond, J. M., C. Measures, R. E. McDuff, L. H. Chan, R. Collier, B. Grant, L. I. Gordon, and J. B. Corliss (1979), Ridge crest hydrothermal activity and the balances of the major and minor elements in the ocean: The Galapagos data, *Earth Planet. Sci. Lett.*, *46*, 1–18, doi:10.1016/0012-821X(79)90061-X.

Ehlmann, B. L., et al. (2009), Identification of hydrated silicate minerals on Mars using MRO-CRISM: Geologic context near Nili Fossae and implications for aqueous alteration, *J. Geophys. Res.*, *114*, E00D08, doi:10.1029/2009JE003339.

Ehlmann, B. L., J. F. Mustard, S. L. Murchie, J.-P. Bibring, A. Meunier, A. A. Fraeman, and Y. Langevin (2011), Subsurface water and clay mineral formation during the early history of Mars, *Nature*, *479*, 53–60, doi:10.1038/nature10582.

Elderfield, H., and A. Schultz (1996), Mid-ocean ridge hydrothermal fluxes and the chemical composition of the ocean, *Annu. Rev. Earth Planet. Sci.*, *24*, 191–224, doi:10.1146/annurev.earth.24.1.191.

Ernst, R. E., E. B. Grosfils, and D. Mège (2001), Giant dike swarms: Earth, Venus, and Mars, *Annu. Rev. Earth Planet. Sci.*, *29*, 489–534, doi:10.1146/annurev.earth.29.1.489.

Fisher, A. T. (1998), Permeability within basaltic oceanic crust, *Rev. Geophys.*, *36*(2), 143–182, doi:10.1029/97RG02916.

Germanovich, L. N., and R. P. Lowell (1995), The mechanism of phreatic eruptions, *J. Geophys. Res.*, *100*, 8417–8434, doi:10.1029/94JB03096.

Gold, T., B. T. OLeary, and M. Campbell (1971), Some physical properties of Apollo 12 lunar samples, *Proc. Lunar Sci. Conf.,2nd*, *3*, 2173–2181.

Grotzinger, J. P., et al. (2005), Stratigraphy and sedimentology of a dry to wet eolian depositional system, Burns formation, Meridiani Planum, Mars, *Earth Planet. Sci. Lett.*, *240*, 11–72, doi:10.1016/j.epsl.2005.09.039.

Gudmundsson, A. (2001), Fluid overpressure and flow in fault zones: Field measurements and models, *Tectonophysics*, *336*, 183–197, doi:10.1016/S0040-1951(01)00101-9.

Gulick, V. C. (1993), Magmatic intrusions and hydrothermal systems: Implications for the formation of Martian fluvial valleys, PhD thesis, Univ. of Ariz., Tucson.

Gulick, V. C. (1998), Magmatic intrusions and a hydrothermal origin for fluvial valleys on Mars, *J. Geophys. Res.*, *103*, 19,365–19,387, doi:10.1029/98JE01321.

Gulick, V. C., and V. R. Baker (1993), Fluvial erosion on Mars: Implications for paleoclimatic change, *Lunar Planet. Sci. XXIV*, Abstract 1295.

Gulick, V. C., D. Tyler, C. P. McKay, and R. M. Haberle (1997), Episodic ocean-induced CO_2 pulses on Mars: Implications for fluvial valley formation, *Icarus*, *130*, 68–86, doi:10.1006/icar.1997.5802.

Hall, J. L., S. C. Solomon, and J. W. Head (1986), Elysium region, Mars: Test of lithospheric loading models for the formation of tectonic features, *J. Geophys. Res.*, *91*, 11,377–11,392, doi:10.1029/JB091iB11p11377.

Hamilton, C. W., S. A. Fagents, and T. Thordarson (2011), Lava–ground ice interactions in Elysium Planitia, Mars: Geomorphological and geospatial analysis of the Tartarus Colles cone groups, *J. Geophys. Res.*, *116*, E03004, doi:10.1029/2010JE003657.

Hanna, J. C., and R. J. Phillips (2006), Tectonic pressurization of aquifers in the formation of Mangala and Athabasca Valles, Mars, *J. Geophys. Res.*, *111*, E03003, doi:10.1029/2005JE002546.

Hannington, M. D., I. R. Jonasson, P. Herzig, and S. Petersen (1995), Physical and chemical processes of seafloor mineralization at mid-ocean ridges, in *Seafloor Hydrothermal Systems*, *Geophys. Monogr. Ser*, vol. 91, edited by S. E. Humphis et al., pp. 115–157, AGU, Washington, D. C., doi:10.1029/GM091p0115

Harrison, K. P., and R. E. Grimm (2002), Controls on Martian hydrothermal systems: Application to valley network and magnetic anomaly formation, *J. Geophys. Res.*, *107*(E5), 5025, doi:10.1029/2001JE001616.

Head, J. W., L. Wilson, and K. Mitchell (2003), Generation of recent massive water floods at Cerberus Fossae, Mars by dike emplacement, cryospheric cracking, and confined aquifer groundwater release, *Geophys. Res. Lett.*, *30*(11), 1577, doi:10.1029/2003GL017135.

Hedenquist, J. W., and J. B. Lowenstern (1994), The role of magmas in the formation of hydrothermal ore deposits, *Nature*, *370*, 519–527, doi:10.1038/370519a0.

Hubbert, M. K., and W. W. Rubey (1959), Role of fluid pressure in mechanics of overthrust faulting, *Geol. Soc. Am. Bull.*, *70*, 115–166, doi:10.1130/0016-7606(1959)70[115:ROFPIM]2.0.CO;2.

Hurwitz, D. M., and J. W. Head (2012), Testing the late-stage outflow channel origin hypothesis: Investigating both water erosion and lava erosion origins for Athabasca Valles, Mars, *Lunar Planet. Sci.*, *XLIII*, Abstract 1056.

Jakosky, B. M., and R. J. Phillips (2001), Mars' volatile and climate history, *Nature*, *412*, 237–244.

Klein, F. W., P. Einarsson, and M. Wyss (1977), The Reykjanes Peninsula, Iceland, earthquake swarm of September 1972 and its tectonic significance, *J. Geophys. Res.*, *82*, 865–888, doi:10.1029/JB082i005p00865.

Lewis, K. C., and R. P. Lowell (2009a), Numerical modeling of two-phase flow in the NaCl-H_2O system: Introduction of a numerical method and benchmarking, *J. Geophys. Res.*, *114*, B05202, doi:10.1029/2008JB006029.

Lewis, K. C., and R. P. Lowell (2009b), Numerical modeling of two-phase flow in the NaCl-H_2O system: 2. Examples, *J. Geophys. Res.*, *114*, B08204, doi:10.1029/2008JB006030.

Linde, A. T., K. Agustsson, I. S. Sacks, and R. Stefansson (1993), Mechanism of the 1991 eruption of Hekla from continuous borehole strain monitoring, *Nature*, *365*, 737–740, doi:10.1038/365737a0.

Lowell, R. (1991), Modeling continental and submarine hydrothermal systems, *Rev. Geophys.*, *29*(3), 457–476, doi:10.1029/91RG01080.

Lowell, R. P., and P. A. Rona (2004), Tectonics/Hydrothermal activity, in *Encyclopedia of Geology*, edited by R. C. Selley, L. R. M. Cocks, and I. R. Plimer, pp. 362–372, Elsevier, Oxford, U. K.

Manga, M. (2004), Martian floods at Cerberus Fossae can be produced by groundwater discharge, *Geophys. Res. Lett.*, *31*, L02702, doi:10.1029/2003GL018958.

Marzo, G. A., A. F. Davila, L. L. Tornabene, J. M. Dohm, A. G. Fairén, C. Gross, T. Kneissl, J. L. Bishop, T. L. Roush, and C. P. McKay (2010), Evidence for Hesperian impact-induced hydrothermalism on Mars, *Icarus*, *208*, 667–683, doi:10.1016/j.icarus.2010.03.013.

Maxwell, J. C. (1964), Influence of depth, temperature, and geologic age on porosity of quartzose sandstones, *Am. Assoc. Pet. Geol. Bull.*, *48*, 697–709.

McEwen, A. S., et al. (2011), Seasonal flows on warm Martian slopes, *Science*, *333*, 740–743, doi:10.1126/science.1204816.

McKenzie, D., and F. Nimmo (1999), The generation of Martian floods by the melting of ground ice above dykes, *Nature*, *397*, 231–233, doi:10.1038/16649.

Mège, D., and P. Masson (1996), A plume tectonics model for the Tharsis province, Mars, *Planet. Space Sci.*, *44*, 1499–1546, doi:10.1016/S0032-0633(96)00113-4.

Mitchell, K. L., F. Leesch, and L. Wilson (2005), Uncertainties in water discharge rates at the Athabasca Valles paleochannel system, Mars, *Lunar Planet. Sci.*, *XXXVI*, Abstract 1930.

Mouginis-Mark, P. J. (1990), Recent water release in the Tharsis region of Mars, *Icarus*, *84*, 362–373, doi:10.1016/0019-1035(90)90044-A.

Murchie, S., et al. (2007), Compact Reconnaissance Imaging Spectrometer for Mars (CRISM) on Mars Reconnaissance Orbiter (MRO), *J. Geophys. Res.*, *112*, E05S03, doi:10.1029/2006JE002682.

Murchie, S. L., et al. (2009), Compact Reconnaissance Imaging Spectrometer investigation and data set from the Mars Reconnaissance Orbiter's primary science phase, *J. Geophys. Res.*, *114*, E00D06, doi:10.1029/2009JE003342.

Nehlig, P., and T. Juteau (1988), Flow porosities, permeabilities and preliminary data on fluid inclusions and fossil thermal gradients in the crustal sequence of the Sumail ophiolite (Oman), *Tectonophysics*, *151*, 199–221, doi:10.1016/0040-1951(88)90246-6.

Ogawa, Y., Y. Yamagishi, and K. Kurita (2003), Evaluation of melting process of the permafrost on Mars: Its implication for surface features, *J. Geophys. Res.*, *108*(E4), 8046, doi:10.1029/2002JE001886.

Old, G. H., D. M. Lawler, and Á. Snorrason (2005), Discharge and suspended sediment dynamics during two jökulhlaups in the Skaftá river, Iceland, *Earth Surf. Processes Landforms*, *30*, 1441–1460, doi:10.1002/esp.1216.

Parmentier, E. M. (1979), Two phase natural convection adjacent to a vertical heated surface in a permeable medium, *J. Heat Mass Transfer*, *22*, 849–855, doi:10.1016/0017-9310(79)90025-5.

Pettijohn, F. J. (1975), *Sedimentary Rocks*, 3rd ed., Harper and Row, New York.

Plaut, J. J., et al. (2007), Subsurface radar sounding of the South Pole layered deposits of Mars, *Science*, *316*, 92–95, doi:10.1126/science.1139672.

Pollack, J. B., J. F. Kasting, S. M. Richardson, and K. Poltakoff (1987), The case for a wet, warm climate on early Mars, *Icarus*, *39*, 88–110.

Pollard, D. D. (1987), Elementary fracture mechanics applied to the structural interpretation of dykes, in *Mafic Dyke Swarms*, edited by H. C. Halls and W. H. Fahrig, *Geol. Assoc. Can. Spec. Pap.*, *34*, 5–24.

Rathbun, J., and S. Squyres (2002), Hydrothermal systems associated with Martian impact craters, *Icarus*, *157*, 362–372, doi:10.1006/icar.2002.6838.

Roberts, G. P., B. Matthews, C. Bristow, L. Guerrieri, and J. Vetterlein (2012), Possible evidence of paleomarsquakes from fallen boulder populations, Cerberus Fossae, Mars, *J. Geophys. Res.*, *117*, E02009, doi:10.1029/2011JE003816.

Saar, M. O., and M. Manga (2004), Depth dependence of permeability in the Oregon Cascades inferred from hydrogeologic, thermal, seismic, and magmatic modeling constraints, *J. Geophys. Res.*, *109*, B04204, doi:10.1029/2003JB002855.

Schmidt, M. E., et al. (2008), Hydrothermal origin of halogens at Home Plate, Gusev Crater, *J. Geophys. Res.*, *113*, E06S12, doi:10.1029/2007JE003027.

Schubert, G., and T. Spohn (1990), Thermal history of Mars and the sulfur content of its core, *J. Geophys. Res.*, *95*, 14,095–14,104, doi:10.1029/JB095iB09p14095.

Seibert, N. M., and J. S. Kargel (2001), Small-scale polygonal terrain: Implications for Martian liquid surface water, *Geophys. Res. Lett.*, *28*(5), 899–902, doi:10.1029/2000GL012093.

Siegfried, R. W., G. Simmons, D. Richter, and F. Horz (1977), Microfractures produced by a laboratory scale hypervelocity impact into granite, *Proc. Lunar Sci. Conf.*, *8th*, 1249–1270.

Squyres, S., D. Wilhelms, and A. Moosman (1987), Large-scale volcano–ground ice interactions on Mars, *Icarus*, *70*, 385–408, doi:10.1016/0019-1035(87)90085-6.

Squyres, S. W., et al. (2008), Detection of silica-rich deposits on Mars, *Science*, *320*, 1063–1067, doi:10.1126/science.1155429.

Stillman, D. E., and R. E. Grimm (2011), Radar penetrates only the youngest geological units on Mars, *J. Geophys. Res.*, *116*, E03001, doi:10.1029/2010JE003661.

Thompson, A. B., and J. A. D. Connolly (1992), Migration of metamorphic fluid: Some aspects of mass and heat transfer, *Earth Sci. Rev.*, *32*, 107–121, doi:10.1016/0012-8252(92)90014-K.

Todd, T., D. A. Richter, G. Simmons, and H. Wang (1973), Unique characterization of lunar samples by physical properties, *Proc. Lunar Sci. Conf.*, *4th*, 2639–2662.

Toksöz, M. N., and A. T. Hsui (1978), Thermal history and evolution of Mars, *Icarus*, *34*, 537–547, doi:10.1016/0019-1035(78)90043-X.

Travis, B. J., N. D. Rosenberg, and J. N. Cuzzi (2003), On the role of widespread subsurface convection in bringing liquid water close to Mars' surface, *J. Geophys. Res.*, *108*(E4), 8040, doi:10.1029/2002JE001877.

van Everdingen, D. A. (1995), Fracture characteristics of the Sheeted Dike Complex, Troodos ophiolite, Cyprus: Implications for permeability of oceanic crust, *J. Geophys. Res.*, *100*, 19,957–19,972, doi:10.1029/95JB01575.

Voss, C. I. (1984), SUTRA, *U.S. Geol. Surv. Water Resour. Invest. Rep.*, *84–4369*, 409 pp.

Watters, T. R., et al. (2007), Radar sounding of the Medusae Fossae Formation Mars: Equatorial ice or dry, low-density deposits?, *Science*, *318*, 1125–1128, doi:10.1126/science.1148112.

Weis, P. L., and W. L. Newman (1976), *The Channeled Scablands of Eastern Washington: The Geologic Story of the Spokane Flood*, 23 pp., U.S. Geol. Survey, Washington, D. C.

Wilcock, W. S. D., and A. McNabb (1996), Estimates of crustal permeability on the Endeavour segment of the Juan de Fuca mid-ocean ridge, *Earth Planet. Sci. Lett.*, *138*, 83–91, doi:10.1016/0012-821X(95)00225-2.

Wilson, L., and J. W. Head (2002), Heat transfer and melting in subglacial basaltic volcanic eruptions: Implications for volcanic deposit morphology and meltwater volumes, in *Volcano-Ice Interaction on Earth and Mars*, edited by J. L. Smellie and M. G. Chapman, *Geol. Soc. Special Publ.*, *202*, 5–26, doi:10.1144/GSL.SP.2002.202.01.02.

Wyrick, D., D. A. Ferrill, A. P. Morris, S. L. Colton, and D. W. Sims (2004), Distribution, morphology, and origins of Martian pit crater chains, *J. Geophys. Res.*, *109*, E06005, doi:10.1029/2004JE002240.

Yen, A. S., et al. (2008), Hydrothermal processes at Gusev Crater: An evaluation of Paso Robles class soils, *J. Geophys. Res.*, *113*, E06S10, doi:10.1029/2007JE002978.

3 Shallow water sill formation on Europa

Abstract

Recent work has suggested that lithospheric flexure and flanking fractures observed along some ridges on Europa are best explained by the initial presence of a shallow liquid water sill. The emplacement of a sill suggests certain conditions existed that were favorable for water flow from a subsurface ocean into an overlying ice shell. These include: stresses that could initiate a fracture in the ice shell and provide a conduit for liquid water to ascend from the ocean through a substantial portion of the shell; a stress field in the region where the vertical fracture halts that would allow horizontal fracturing for sill emplacement; and an environment that would enable a sill lifetime of ~ 1000s of years. Here, we investigate whether these conditions could occur and result in sill formation.

Previous models of the stresses resulting from ice shell thickening on Europa indicated that fractures can initiate within the shell and propagate both upward toward the surface and downward to the ice-ocean interface. For an ~10 km thick ice shell, we determined that flow velocities for ocean water driven up a vertical fracture by the release of lithostatic pressure are adequate for reaching the subsurface before freezing occurs. We propose the next step for sill emplacement could occur through horizontal fracturing. Nominally, the stress field in a material under lithostatic load is conducive to vertical crack propagation. Factors exist, however, that can change the stress field and encourage horizontal crack propagation.

Seismically imaged terrestrial sills beneath mid-ocean ridges often occur in areas with extensive cracking and/or faulting, suggesting crack interactions may play a key role. Through application of a finite element program we tested the influence of four stress changing mechanisms on Europa: (1) mechanical layering, (2) shallow surface cracks in the ice, (3) deep cracks initiated in a similar manner as our sill-forming fracture or by mechanisms such as upward propagating water-filled cracks and (4) a combination of mechanisms (2) and (3). We propagated a pressurized fracture through a 10 km thick ice shell and results determined that all mechanisms can cause a degree of turn in propagation direction, with Model 4 (both shallow and deep cracks) enabling the greatest turn to ~ horizontal. The horizontal extent of the fracture propagation, however, only reaches a width of ~ 100s meters, whereas a sill of ~ 4 km width was determined necessary for formation of the flanking fractures at their observed locations on the ridges.

A recent study suggests a liquid water sill would need to exist for 1000s of years to enable the lithosphere flexure observed. Assessment of sill lifetime finds that a 10 – 100 m thick sill will convect and transfer its heat away over ~ hours to a few days, respectively. One possible mechanism to extend the sill lifetime could involve liquid water replenishment from the ocean driven by brine migration, although the lifetime may still prove challenging to achieve.

Overall, our analyses suggest sill emplacement may be possible by liquid ocean water flow up an open vertical fracture to the subsurface and fracture propagation turned horizontal by stress field change factors such as shallow and deep cracks. However, sill width and lifetime remain a challenge to achieve.

3.1 Introduction

The Jovian moon Europa sparks our curiosities with the promise of a vast, salty and thermally mixing ocean that may harbor life beneath its icy exterior [*Vance and Goodman*, 2009]. Data returned by the Voyager and Galileo spacecrafts enabled the determination of the differentiation achieved within Europa. A vast water ocean topped with an icy shell overlies a rocky layer with a metallic core. The layer of water and ice is estimated to range between 105 and 160 km thick, as constrained by composition and structural differences in the rocky layer beneath [*Kuskov and Kronrod*, 2005; *Cammarano et al.*, 2006]. Model estimates for ice shell thickness based on thermal analyses, impact studies and mechanical calculations were summarized in *Billings and Kattenhorn* [2005]. Estimates for the total shell thickness ranged from ~ 0.25 km [*Tufts*, 1998] to less than a few tens of km [*Schenk and McKinnon*, 1989; *Lucchitta and Soderblom,* 1982; *Rathbun et al.,* 1998; *Sotin et al.*, 2004]. Flexure models suggest an elastic thickness of the ice shell of ~ 2 km [*Williams and Greeley*, 1998; *Pappalardo,* 1999].

Tectonic features cover Europa indicating a structurally active history that may have provided an avenue for deeper material to interact with the surface. One prominent tectonic feature on Europa is the double ridge. Double ridge features are ubiquitous on Europa and can run fairly linearly for greater than 1000 km, however their formation process is still not completely understood. Through improving our understanding of how ridges can form, further characterization of Europa's ice shell is possible and provides indications about the ocean structure below. Double ridge morphology typically exhibits marginal troughs and subparallel flanking fractures occur at some ridges. Figure 3.1 shows the double ridge, Androgeous Linea, with arrows indicating locations of flanking fractures. Several studies suggest these fractures result from the load of the ridge causing flexure in a generally thin elastic lithosphere estimated

to be between a couple hundred meters up to about 6 km thick [*Billings and Kattenhorn*, 2005; *Hurford et al.*, 2005; *Nimmo et al.,* 2003]. As determined by *Dombard et al.* [2013; 2007], a thin elastic lithosphere of ~ 100 m to 1 km requires a heat flow of about 1 W/m^2 which is inconsistent with the estimated heat flow for Europa of ~50 - 200 mW/m^2 [*Pappalardo 1999*, *Ruiz and Tejero*, 1999; *Ruiz and Tejero*, 2000]. This discrepancy suggests a local, shallow heat source is necessary [cf. *Dombard et al.*, 2007]. Several proposed ridge formation mechanisms provide a local thermal source through subsurface liquid water associated with dikes, diapirs and/or frictional heating and are consistent with the presence of flanking fractures. *Kadel et al.* [1998] proposed ridge building by way of cryoclastic eruptions through a preexisting open fissure to the surface. *Pappalardo and Coon* [1996] suggested tidal forcing could squeeze material up through a crack, a model developed further by *Greenberg et al.* [1998] and *Tufts et al.* [2000]. *Fagents* [2003] described the presence of volatiles or pressurization of a subsurface reservoir as a means to expel fluid on the surface. Most recently, *Dombard et al.* [2007, 2013] also suggested a cryovolcanic mechanism but added formation of a water sill beneath the ridge. For both the diapir mechanism employed by *Head et al.* [1999] and the shear heating model suggested by *Gaidos and Nimmo* [2000], *Nimmo and Gaidos* [2002] and *Han and Showman* [2008], the ridges are raised up as a consequence of thermal expansion along a plane in the ductile region of the ice shell beneath a brittle region with the central preexisting crack. *Dombard et al.* [2013] evaluated these ridge-forming mechanisms and argued that only a shallow cryovolcanic sill could provide a thermal anomaly of the required lateral extent to cause flanking fractures to occur at the observed distances from the central trough (Figure 3.2). The question then remains as to how to emplace a water sill at depth of ~1-2 km in the ice shell on Europa.

To form the shallow water sill suggested by *Dombard et al.* [2013] within the ice shell of Europa, we employ the idea of a fracture, hereafter referred to as the 'primary fracture', that initiates as a dry crack within the shell and propagates vertically upwards some distance and down to the ocean. Once open to the ocean, water then flows up the primary fracture to a shallow depth beneath the surface, turns horizontally and propagates a fracture to form a sill. Primary fracture initiation could occur in the shallow subsurface through the build up of tensile stresses as a result of volume expansion and thermal contraction of ice as the shell cools and thickens over time [*Nimmo*, 2004]. Model results of *Nimmo* [2004] show that for an ~ 10 km thick shell, the tensile stresses peak at ~ a few MPa within 1 – 2 km of the surface. *Manga and Wang* [2007] determined that a primary fracture initiated within Europa's ice shell could propagate up to the surface and down to the ocean, providing a pathway for ocean water to rise towards the surface. With an open primary fracture, *Manga and Wang* [2007] investigated the height to which ocean water could flow, considering the lithostatic (ice shell) load and additional pressure supplied from shell expansion during cooling and thickening. Their models suggested that the pressurized ocean could not drive the water the entire distance to the surface, given the density difference between ice and water and a small pressure increase from the ice volume expansion (exasperated by the likelihood of high porosities near the surface and briny ocean water). For an ~ 10 km thick ice shell, the highest point water could reach is ~ 10 m above the neutral buoyancy depth of around 1 km (see calculation in Section 3.3). Though the water will not reach the surface driven by lithostatic and ice shell expansion pressures, a sill might still be emplaced at the neutral buoyancy, or greater, depths to enable ridge flexure.

We build on the stress accrual and fracturing analyses by *Manga and Wang* [2007] and *Nimmo* [2004] for a cooling and thickening ice shell to explore the viability of sill emplacement

in the shallow subsurface (~ 1 - 2 km depth) of Europa. Figure 3.3 depicts our proposed steps for sill emplacement. We suggest that once a primary fracture initiates (Figure 3.3a) and propagates vertically down to the ocean (Figure 3.3b), water is then driven through the fracture to a shallow depth of ~ 1 - 2 km (Figure 3.3c) where a change in the stress field causes an ~ horizontal fracture to initiate and propagate laterally to form a sill (Figure 3.3d). To determine the soundness of the process we determine: (1) whether the ocean water travels quickly enough to reach the subsurface before freezing; (2) whether a weakened or altered stress region in the ice could enable a change in the primary fracture propagation direction from vertical to horizontal; and (3) whether a water sill, once emplaced, could remain warm long enough to thin the overlying lithosphere and cause ridge flexure.

Details of our study are described in Sections 3.2 – 3.5. Section 3.2 evaluates the flow velocity that occurs up the vertical primary fracture and Section 3.3 investigates the process of forming a sill through horizontal fracturing. In Section 3.4 we investigate heat transfer from the cooling sill by thermal convection and calculate the resulting lifetime. Section 3.5 concludes the paper with discussion of the results and suggestions for further studies.

3.2 Vertical Flow Velocity

Once a vertical fracture opens in the shallow subsurface in Europa's ice shell and connects to the ocean below, the pressure due to ice shell overburden will drive the ocean water up through the fracture (Figure 3.3c). To emplace a shallow sill, the ocean water must be able to flow upwards and reach the desired depth before freezing occurs. Overburden pressure at the base of the ice shell, P_0, is a function of ice shell thickness, H:

$$P_0 = \rho_{ice} g H \tag{1}$$

where ρ_{ice} is the density of the ice and g is the gravitational acceleration (Table 3.1). For H = 10 km we find a driving pressure of P_0 = 11.7 MPa at the ice shell base.

We estimate the time for cooling and freezing of the water according to the conductive time scale, τ_d:

$$\tau_d \approx w^2 / \kappa \tag{2}$$

where w is fracture width and κ is thermal diffusivity of water (Table 3.1). The expected width can be determined using crack aspect ratio relationships relating internal fluid pressure, surrounding stresses, and host medium stiffness. Based on cracks observed in terrestrial volcanic dikes, *Pollard* [1987] and *Rubin* [1995] describe the relationship between crack aspect ratio, (w/l), and ratio of driving pressure, (P_f - σ_x), to host medium stiffness, $G/(1-\nu)$:

$$\frac{w}{l} \approx \frac{(P_f - \sigma_x)}{G/(1-\nu)} \tag{3}$$

where l is the dike height, P_f is the internal fluid pressure, σ_x is the horizontal compressive lithostatic stress and G and ν are the shear modulus and Poisson's ratio of the host medium, respectively. σ_x increases with depth, d as:

$$\sigma_x = \nu/(1-\nu)*\sigma_y = \nu/(1-\nu)*\rho_{ice} g d \tag{4}$$

where σ_y is the vertical lithostatic load, $\sigma_L = \rho_{ice} g d$. For a Young's modulus of $E \sim 5$ GPa and $\nu \sim 0.3$, terrestrial sea ice typically has a $G \sim 2$ GPa as described by *Weeks and Assur* [1967]. Then, for an ice shell with thickness of ~ 10 km, the difference in fluid pressure and horizontal stress will range from ~ 1 to 5 MPa. These values applied in Equation (3) give a crack aspect ratio of ~ 10^{-3} that indicates a dike width of ~ 10 m for the ~ 10 km tall dike. Typical terrestrial crack aspect ratios observed also include values of 10^{-2} [*Rubin*, 1995]. Therefore, we considered fracture widths of 10 and 100 m. Equation (2) indicates a conductive lifetime range from ~3 to 30 years, for the 10 and 100 m widths, respectively.

We then calculated the velocity the fluid would travel up the vertical fracture to determine the time required to reach a shallow depth of ~ 1 – 2 km. First, we used the Reynolds number relationship (Equation 5) to determine whether the flow in a 10 – 100 m wide fracture would be laminar or turbulent. If flow is turbulent, eddies occur that affect fluid viscosity (see Section 3.5 - Discussion) and may need to be considered. The Reynolds number relationship is expressed as:

$$\mathrm{Re} = \frac{\rho_w v w}{\mu} \tag{5}$$

where $\rho_w = 1000$ kg/m^3, v is the water velocity and μ is the dynamic viscosity of water = 10^{-3} Pa s. For flow between parallel plates, laminar flow occurs when Re < 1400. Rearranging equation (5) to solve for v and setting Re ~ 1400:

$$1400 > \frac{\rho_w v w}{\mu}$$
$$v < \frac{1400\mu}{\rho_w w} \tag{6}$$

we find the flow velocity in a 10 – 100 m wide fracture would need to be below ~ 10^{-7} m/s to have laminar flow. Applying the Navier-Stokes equation for incompressible flow:

$$\rho_w\left(\frac{\partial \vec{v}}{\partial t} + \vec{v}\cdot\nabla\vec{v}\right) = -\nabla P + \mu\nabla^2\vec{v} + \vec{f} \tag{7}$$

where t is time, P is the pressure and f represents the body forces. Laminar flow in the fracture would be controlled by the viscosity term, μ. Then, assuming a constant flow velocity over time and laminar flow, equation (7) reduces to:

$$\nabla P = \mu\nabla^2\vec{v} \tag{8}$$

where the pressure gradient ∇P is caused by the overburden of the ice shell on the ocean ~ $\rho_{ice}gH/H$, where H, is the ~ 10 km thick ice shell. Assuming a constant pressure difference along the fracture height (y-direction), $\partial P/\partial y$, and a vertical flow velocity, v, that only changes across the fracture width, we can solve for the maximum water velocity (assumes constant pressure gradient), which provides an upper estimate for flow speed:

$$\frac{\partial P}{\partial y} = \mu\frac{\partial^2 v}{\partial x^2} \tag{9}$$

where x is across the width of the fracture. Integrating equation (9) twice and setting $\partial P \sim \rho_{ice} g H$ and $\partial y = H$, we can solve for v_{max}:

$$v_{\max} = \frac{\rho_{ice} g w^2}{8\mu} \tag{10}$$

For ρ_{ice} = 900 kg/m^3, g = 1.3 m/s^2 and w = 10 m, we find a vertically velocity of v_{max} = 1.4 x 10^8 m/s. This extremely high value is not realistic and indicates that flow will be turbulent. We then apply the Navier-Stokes equation to calculate the velocity based on turbulent flow.

The term, $\vec{v} \cdot \nabla \vec{v}$, controls the flow in turbulent flow and for constant velocity over time, equation (7) reduces to:

$$\frac{\rho_w v_{\max}^2}{H} \sim -\nabla P \tag{11}$$

Remembering $-\nabla P \sim \rho_{ice} g H/H$, we solve for v_{max}:

$$v_{\max} = \sqrt{\frac{\rho_{ice} g H}{\rho_w}} \tag{12}$$

For H ~ 10 km, a fluid velocity of ~ 108 m/s results. The speed of sound in water is ~ 1500 m/s, from $c = (B/\rho_w)^{1/2}$, where B = 2.2 x 10^9 Pa is the bulk modulus of water. Therefore, the flow will be subsonic and will take about 1.5 minutes to reach the shallow depth of ~ 1 - 2 km in the shell.

For this upper end flow velocity estimate, comparison of the 1.5 minutes to the fracture conductive lifetime of ~3 years shows there is little need for concern of freezing before reaching the ~ 1 - 2 km deep subsurface. However, the velocity will decrease as the fluid rises in the fracture as a result of the decrease in driving pressure as the water moves upward. These factors and their effects are addressed in Section 3.5 – Discussion.

3.3 Sill Emplacement Through Fracturing

Once the ocean water reaches the top of the open fracture, the fracture may continue to propagate to the point of neutral buoyancy or turn horizontally at a deeper location to form a sill. Sill emplacement depends on the presence of a stress field around the fracture favorable for horizontal propagation and a fracture pressure with tip stresses that can overcome the ice tensile strength and surrounding lithostatic load. We perform finite element analyses to investigate the stress field around a central fracture connected to the Europan ocean for a variety of ice shell subsurface configurations based on suggested terrestrial sill emplacement mechanisms.

First, to determine the minimum possible depth of sill emplacement, we calculate the point of neutral buoyancy. This occurs where the driving pressure, due to lithostatic load of the ice shell, $P_0 = \rho_{ice} g H$ (Equation 1), equals the water column load, $\rho_w g h$. Solving for neutral buoyancy location as height above the base of the ice shell, h:

$$h = \frac{\rho_{ice}}{\rho_w} H \tag{13}$$

For plausible values (Table 3.1) of ρ_{ice}, ρ_w and H, h = 9 km. A sill might become emplaced at this neutral buoyancy level, although fracturing processes are not likely since no driving pressure remains there. At a depth greater than neutral buoyancy, pressure exists to drive the flow horizontally some distance [e.g. *Collins et al.*, 2000] provided the stress field is favorable.

On Earth, we observe the presence of magmatic sills in ophiolites, structures believed to be remnant sections of ocean ridges. The evidence suggests sills may be a common intrusion type in the mid to lower oceanic crust [*Ildefonse et al.*, 1993; *Kelemen et al.*, 1997]. Sills are also seismically imaged beneath ocean ridge segments [e.g. *Hansen and Cartwright*, 2006; *Kent et al.,* 2000]. Although observations and seismic images confirm the existence of sills, the emplacement mechanism is not completely understood. According to fracture mechanics, cracks will propagate perpendicular to the least principal compressive stress (or maximum principal tensile stress), σ_3. In a homogenous crust, lithostatic stress (ρgd) occurs in all directions, yet measurements of terrestrial in-situ stress record a lower horizontal stress value, assumed to occur due to the partially constrained horizontal expansion of the crust and/or extensional stresses such as at ridge spreading centers and rifts. The least compressive stress, therefore, occurs horizontally, nominally and vertical crack growth is expected. However, given that sills do occur, other factors must cause a change in σ_3 from horizontal to vertical. Proposed mechanisms include (Figure 3.4): mechanical layering [e.g. *Kavanagh et al.,* 2006], shallow subsurface cracking and faults [*Hansen and Cartwright*, 2012], magmatic surge and multiple dike intrusions [*Fialko*, 2001; *Ildefonse et al.,* 1993], and/or lateral stress gradients caused by thickening of the brittle crust layer with increasing distance from the axial magma source [*Grandin et al.,* 2012].

In this study, we concentrated on the aspects of sill emplacement that involve fracturing and surrounding stress generation by testing four models that employ 3 of the 4 proposed stress

change mechanisms: Model 1- two layers with different material properties, Model 2- shallow cracks, Model 3- deep cracks at the base of the ice shell, and Model 4- shallow and deep cracks combined. Our analyses determine the effects that each of the mechanisms has on the stress field and propagation direction of a central fracture open to the Europan ocean. We do not model the *Grandin et al.* [2012] lateral stress gradient mechanism here, but describe it in detail in the discussion section. Before describing details of the models and their results (Section 3.3.2), we begin by providing the background motivation for investigating each mechanism for enabling sill emplacement, based on terrestrial observations or material experiments (Section 3.3.1.1) and explain the fracture mechanics theory for crack propagation (Section 3.3.1.2).

3.3.1 *Horizontal fracturing processes*

3.3.1.1 Mechanisms for stress field change

Mechanical layering could enable horizontal fracture propagation by providing a change in the stress field [e.g. *Grandin et al.*, 2012], forming a weakened avenue for fluid flow [e.g. *Thomson*, 2007] or for fracturing delamination [*Gudmundsson,* 2011]. *Grandin et al.* [2012] suggest the increase in depth of the brittle to ductile transition in the lithosphere causes a stress gradient that enables dike intrusions to move laterally from the magma source. On Europa, the water-filled vertical fracture reaching from the ocean would act as a thermal anomaly and cause a thinning of the overlying elastic layer in the ice shell. The elastic layer would then thicken with distance from the fracture in a similar fashion to that observed in *Grandin et al.* [2012]. This layer thickening may then act to encourage horizontal crack growth.

Layer contacts allowing delamination and weakened stress regions could be caused by differences in mechanical properties resulting from higher porosity near the surface [*Nimmo et*

al., 2003], the increase in ice stiffness with lower temperatures as distance to Europa's surface decreases, brine pockets postulated to exist in the subsurface based on observed surface salts [e.g. *Gaidos and Nimmo*, 2000; *Travis et al.*, 2012], and/or shallow cracks. Delamination could occur, particularly in the shallow subsurface regions with lower overburden, where fracture tip induced tensile stresses open the contact interface ahead of the propagating fracture [*Gudmundsson*, 2011]. A t-shaped fracture that grows along the interface could then extend as far as adequate driving pressure remained. Delamination occurs often with composite materials [e.g. *Wang and Xu*, 2006; *Kim et al.*, 2006; *Xu et al.*, 2003] and has been shown experimentally [*Xu et al.*, 2003] and through theoretical analyses [*He and Hutchinson*, 1989].

Using the *Dundurs* [1969] elastic mismatch parameters, α and β, which describe the mechanical change across an interface, the likelihood of deflection of the fracture into a contact region can be determined. The Dundurs parameters, as defined by *Hutchinson* [1996] and *Freund and Suresh* [2003], are:

$$\alpha = \frac{E_1^* - E_2^*}{E_1^* + E_2^*} \tag{14}$$

$$\beta = \frac{1}{2}\frac{G_1(1-2\nu_2) - G_2(1-2\nu_1)}{G_1(1-\nu_2) + G_2(1-\nu_1)} \tag{15}$$

where G is the shear modulus, ν is Poisson's ratio, $E^* = E/(1-\nu)$ is the plain-strain Young's modulus, subscript 2 denotes the layer containing the hydrofracture, while subscript 1 indicates the material on the other side of the interface from layer 2. Equation (14) quantifies the difference in extensional or uniaxial stiffness, while equation (15) calculates volumetric or areal stiffness mismatch [*Freund and Suresh*, 2003]. As described by *Gudmundsson* [2011], for a

layer of greater stiffness overlying a less stiff layer α is positive and the fracture has a greater likelihood of deflecting into the contact region. With increased stiffness of the overlying layer relative to the lower layer, α becomes more positive and the chances of deflection increase.

Cracks proximal to the central fracture may also provide a weakened region that could encourage horizontal fracture propagation. Surface cracks abound on Europa and observations suggest that some penetrate down through the elastic layer (~ a few kilometers) [e.g. *Lee et al.,* 2005; *Rudolph and Manga,* 2009] with others possibly reaching entirely through to the ice-ocean interface [e.g. *Greenberg et al.*, 1998; *Hoppa et al.*, 2000]. If the bottoms of shallow cracks reach close to the top of the central fracture from the ocean, the stress fields around the fracture and cracks can interact and possibly cause changes in propagation direction. The interaction of stress fields induced by the cracks has been observed in lab experiments by e.g. *Olson and Pollard*, [1991]. A terrestrial analog for sill emplacement near cracked subsurface regions occurs beneath the ocean floor within the NE Atlantic Møre Basin. There, *Hansen and Cartwright* [2006] imaged the Solsikke sill complex and fractures/faults and suggest the igneous intrusions formed sills due to the interactions with the fractures/faults and their surrounding damage zones.

Additional cracks may occur at the base of the ice shell due to the cooling of the ice shell through time and/or tidal stresses. The cracks may take the form of water-filled intrusions propagating upwards from the ocean as described by *Crawford and Stevenson* [1988]. These cracks may also alter the stress field near a central fracture to one that enables horizontal propagation. *Ildefonse et al.* (1993) suggest that, on Earth, dikes may also enable stress field change through intermittent magma surges below ocean ridges that temporarily overcome the far-field tensional stress from plate separation and cause the least compressive stress to change from horizontal to vertical. Similarly, on Europa, the surge of water from the ocean into the

open central fracture might cause a temporary high pressure that could surpass the overburden stress and encourage fracture initiation in a more horizontal direction.

Section 3.2 describes the four models investigated using on these proposed stress-change mechanisms and their results. First, though, in the following Section (3.1.2) we discuss the mechanics necessary to enable fracture initiation and propagation through the ice crust.

3.3.1.2 The mechanics of fracture propagation

Minimally, for a horizontal fluid filled fracture, called a "hydrofracture," to initiate in the subsurface the fluid pressure must exceed the vertical overburden load, σ_L, plus the tensile strength of the host medium, T_0:

$$P_f \geq \sigma_L + T_0 \tag{16}$$

where P_f is the fluid pressure in the reservoir [*Gudmundsson,* 2011]. This pressure varies with height above the base of the ice shell, h, as:

$$P_f = P_0 - \rho_w g h \tag{17}$$

where P_0 is the pressure due to σ_L at the shell base = $\rho_{ice} g H$. Values for P_f range from 1.17 x 10^7 Pa at the shell base down to 0 at the neutral buoyancy depth of 1 km, dropping by 1.3 MPa per km. Lithostatic loads also start at 1.17 x 10^7 Pa at the shell base, but only decreases by 1.17 MPa for each km increase. Therefore, nominally in a pure water ice shell, the fluid pressure is always less than the vertical overburden load. However, there may be mechanisms within Europa's ice

shell that change the direction of the stress field such that the vertical overburden is decreased (e.g. porosity, brines, cracks, etc.).

Once a crack does initiate, fracture mechanics theory and laboratory tests dictate a fracture can propagate in a material if the stress intensity factor, K, is greater than the critical stress intensity value, K_c [e.g. *Anderson,* 2005]. For a crack opening, Mode I, type of fracture process in a linear elastic material, where the crack faces move straight apart (see Figure 3.5a), the stress intensity factor, K_I, for a through crack (Figure 3.5b) is defined as:

$$K_I = \sigma\sqrt{\pi a} \tag{18}$$

where a is the half-width of the crack, σ is the opening tensile stress and the material width is assumed to be much greater than the crack width. If we assume a small initial horizontal crack protruding from the main central fracture connecting to Europa's ocean that simulates an edge crack into the ice shell (depicted in Figure 3.6), we can modify equation (18) to determine the critical stress intensity factor, K_{Ic}, needed to initiate a Mode I horizontal fracture (and emplace a sill). For an edge crack in a semi-infinite plate, the stress intensity increases ~ 12% over the through crack value [*Anderson*, 2005]:

$$K_I = 1.12\sigma\sqrt{\pi a} \tag{19}$$

where σ is the opening stress and a is the crack length. To determine the value of K_{Ic} for a fracture in Europa's ice shell, we use equation (19) and assume σ equals the tensile strength of ice, T_0, plus the lithostatic load, σ_L that varies with depth = $\rho_{ice}gD$. The strength of ice varies with

lab samples fracturing at ~ MPa and natural sheets on the ocean and porous ice having strengths as low as ~ 10^4 Pa [e.g. *Dempsey et al.,* 1999; *Lee et al.,* 2005]. For this strength range and an assumed initial crack length of a = ~10 m, K_{Ic} ranges between ~ 1.1 x 10^7 to 1.7 x 10^7 Pa $m^{1/2}$, respectively for horizontal crack propagation at a depth of 1500 m.

The determination of fracture propagation can be simplified from equation (19) given that for a certain fracture length, the opening stress, σ, must be greater than the tensile strength of ice and the lithostatic load acting against opening. The finite element program described below enables assessment of fracture growth by determining the direction of preferred propagation and crack tip stress values and stresses surrounding the crack. If crack tip stress, σ_t, is greater than the lithostatic load normal to the path of propagation, σ_{Ln}, plus the tensile strength of the ice:

$$\sigma_t \geq \sigma_{Ln} + T_0 \tag{20}$$

then fracture propagation can occur.

3.3.2 *Finite element models*

In order to assess the stresses surrounding a fracture in Europa's ice shell and the viability of sill emplacement by propagating the fracture, we perform analyses using a finite element program, FRANC2d (FRacture ANalysis Code) that was designed for incremental fracture analyses in two dimensions [*Wawrzynek and Ingraffea*, 1987]. The FRANC2d program calculates displacements/deformation due to imposed loads, specified boundary conditions, and material properties for a body of certain geometry. Stresses are calculated from the displacements and used with fracture mechanics theory to determine the direction and distance

that fractures can travel. Figure 3.7 depicts the base model we analyze for sill emplacement. A grid 20 km wide by 10 km deep (vertical dimension, H) represents the ice shell under plane strain mode, where the dimension in the third direction (into page), z, is assumed to be much larger than the dimensions in the horizontal, x, and vertical, y, directions. Boundary conditions restrict the left and right sides to no movement in the horizontal direction and the bottom boundary is fixed in the vertical direction. Material properties are set at expected values for Europa: for Young's Modulus, $E = 5 \times 10^9$ Pa [*Haynes,* 1978]; Poisson's ratio, $v = .3$ [*Williams and Greeley*, 1998]; and $\rho_{ice} = 900$ kg/m^3 [*Nimmo*, 2004]. The gravitational acceleration is applied as a body load, $g = 1.3$ m/s^2 in the negative y direction. An initial vertical fracture is then emplaced from ~ 2 km below the top edge (Europa's surface), based on locations of high tensile stresses modeled by *Nimmo* [2004], and extended down to the bottom edge to represent a fracture that opens to the ocean. This vertical fracture is pressurized hydrostatically to represent the presence of the ocean water inside (see Equation 17).

At any depth within the ice shell, emplacing a horizontal crack proves challenging as the overburden pressure from the ice ($\rho_{ice}g(H-h)$) will be greater than P_f and this may prevent a positive opening stress. However, an area of the shell may have a weakened or altered stress field from the vertical fracture emplacement itself, nearby subsurface cracks, and/or mechanical layering where a less dense layer overlies the fracture and lowers the overburden there. These factors would change the directions and values of the principal stresses and may enable horizontal crack growth. Here we modify the base model to analyze four factors that cause stress change and determine their sill emplacement capabilities: (1) layers with different material properties, (2) shallow cracks, (3) deep cracks at the base of the ice shell, and (4) shallow and deep cracks combined.

3.3.2.1 Model 1: Mechanical layering

Using FRANC2d we formed two distinct material layers: one for the upper 2 km and the second below. The uppermost layer's density was set to ρ_{pi} = 855 kg/m^3 to represent a porosity of ϕ = 0.05 as determined necessary for band topography formation by *Nimmo et al.* [2003] for an ~ 2 km thick elastic lithosphere. This porosity value of 5% falls within the range observed in terrestrial glacier ice, although Earth-based 3.5- and 13-cm radar backscatter observations of Europa estimate higher porosities ranging from 33 to 94%, respectively [*Black et al.*, 2001]. We apply the lower porosity to remain conservative with porosity in this model and to allow consideration of a stiff upper layer. The effects of higher porosities will be considered in future work. The depth of the 5% porosity can be estimated at about half of the 3 km deep brittle layer following calculations by *Nimmo et al.* [2003]. The lower ice layer in our 2-layer finite element model has a density set at a higher value of ρ_{bi} = 1120 kg/m^3 to represent briny ice [*Williams and Greely*, 1998]. The upper and lower layers were also assigned Young's modulus values such that there was a difference of 2 orders of magnitude between them in order to represent a significantly colder, stiffer layer above a warmer layer. This magnitude difference in stiffness stems from terrestrial observations of gabbros and basalts layered with volcanic tuffs (numerical models by *Gudmundsson and Brenner* [2004]) and laboratory experiments of layered gelatins by *Kavanagh et al.* [2006].

Model results show that the fracture can propagate since the stress in front of the fracture is tensile and greater than the tensile strength of ice (Figure 3.8a). Also, the analysis shows that the central fracture begins to turn slightly as it approaches the material interface (Figure 3.8b). Once the fracture propagates across the interface and into the upper layer, the propagation

direction turns significantly towards horizontal (> 45° turn). At this point, the FRANC2d program cannot continue to calculate fracture propagation across the material interface, but it is apparent that the material change from a less stiff and denser material to a stiffer, less dense material results in a significant change in the stress field and causes the fracture propagation direction to turn closer to horizontal. This analysis shows that material layering can indeed cause sizeable propagation direction changes. Results of experiments by *Kavanagh et al.* [2006] exploring water intruded into layers of gelatin with contrasting stiffness support these results.

3.3.2.2 Model 2: Shallow subsurface cracks

We also investigated a uniform ice shell with a pervasively fractured subsurface containing 16 cracks from the surface down to 1500 m. The central vertical fracture was emplaced at a depth of 2400 m to the shell base. Figure 3.9a shows this initial model set-up. The fracture was then hydrostatically pressurized and again, the stress field in front of the crack is tensile and greater than T_0, which enables crack growth. Propagation occurred in 100 m steps. Figure 3.9b shows how the fracture path traveled vertically until approaching the shallow crack tips, where just a slight turn occurred. Fracture theory predicts that the crack interaction between the central fracture and shallow crack tips will draw the central fracture towards the shallow cracks (e.g. *Anderson*, 2005; *Gudmundsson,* 2011), though this analysis shows that the turn is only slight and does not enable a ~km-wide sill to form.

3.3.2.3 Model 3: Deep cracks at base of ice shell

The third model investigated the suggestion of *Fialko* [2001] that multiple dike intrusions could change the stress field such that a subsequent intrusion would turn horizontal and emplace

a sill. First, ten cracks were placed in the ice, extending from the base of the model up to a depth of 2300 m. Then, a central, hydrostatically pressurized fracture was emplaced reaching from the base of the ice shell up to a depth of 2500 m. Figure 3.10a shows the base model and Figures 3.10b and 3.10c show the path of subsequent propagation. Surrounding stresses are tensile and greater than ice tensile strength, which enables crack growth. For the first four steps (100 m each), the fracture moves vertically. After this point, the fracture begins to turn slightly to the right. Then, at a depth of ~ 1500 m the fracture turns more significantly until at a depth of ~ 1366 m propagation occurs horizontally (Figure 3.10b). The orange line shows the direction of further propagation. After only one step (100 m) in the horizontal direction, the fracture begins to propagate downward (Figure 3.10d). Figures 3.10b and c also show contours for the values of the principal stress, σ_1, where positive values are tensile and negative are compressive. This downward growth occurs as a result of the low pressure in the fracture and the higher density of water vs. ice that causes a change in the direction of least compressive principal stress/highest tensile principal stress.

As with the shallow crack model, from the knowledge of how cracks in a certain proximity to one another interact and affect the surrounding stress field, we did expect that the central fracture would gravitate towards the nearby crack tips (e.g. *Anderson*, 2005; *Gudmundsson,* 2011). The horizontal turn occurred more for the deep crack model than for the shallow one, indicating that the deep cracks had a more pronounced effect on the stress field surrounding the central fracture. The fracture turn likely occurred due to the low position of the deep cracks that acted to draw the main fracture downwards. This effect can be seen in Figures 3.11 a and b, which show the stress field surrounding the central fracture for the shallow crack model and the deep crack model, respectively. In the shallow crack model, tensile stresses

occurred only at the very tip of the fracture, but in the deep crack model the tensile stresses occurred along a much larger portion of the fracture.

3.3.2.4 Model 4: Shallow and deep cracks

Building on the results found in Models 2 and 3, we employed both the shallow and deep cracks simultaneously in an attempt to achieve significant propagation direction turn towards horizontal and to increase the horizontal propagation distance achieved. Twelve shallow cracks from the surface to 1 km depth were added above 10 deep cracks running from the base of the ice shell up to 2300 m depth (Figure 3.12a). We then emplaced a central, hydrostatically pressurized fracture from the ocean up to 2500 m depth and propagated it towards the surface. Figures 3.12 b and c show the path of crack propagation. One can observe how the fracture turns towards the left and reaches a horizontal distance of ~ 250 m from the starting point. This horizontal extent occurs at a depth of ~ 1200 m where the fracture then begins to propagate downwards due to the low remaining internal pressure (~ 2 x 10^5 Pa) and the surrounding stress field as the fracture approaches the shallow crack. Further propagation can occur, although with increasing fracture length the internal pressure will continue to drop.

We can gain insight into why the fracture turned and was able to propagate more horizontally by noticing the change in stress over the course of fracture propagation. Figure 3.13 show snapshots of the σ_1 stress field throughout the fracture propagation from a depth of 1700m up to 1213 m. One can note the area of positive tensile stresses that occur surrounding the fracture tip and that extend towards the shallow subsurface cracks. The stress fields around the deep cracks from the base of the ice shell are a negative compressive stress (dark red) and contribute to the crack turning horizontally as also occurred for the deep crack model (Model 3).

As previously mentioned, the theory of fracture mechanics and observations in crustal structures on Earth support these findings, as stress fields surrounding cracks will interact and change stress fields that may then enable horizontal crack propagation [e.g. *Gudmundsson*, 2011]. Here, our finite element model shows that the presence of the deep cracks at the base of the ice shell enables the fracture to turn more horizontal and the interaction of the stresses at the propagating fracture tip with the nearby shallow cracks allows further ~ horizontal propagation before being drawn downwards.

3.4 Sill Lifetime

In addition to mechanical issues concerning the formation of a liquid water sill within Europa's ice shell, there are potential thermal issues concerning a sill's lifetime in the liquid state. The sill must remain liquid long enough to transfer heat to and thin, the overlying lithosphere in order for fractures to form alongside the ridges. According to thermal models performed by *Dombard et al.*, [2013; 2007], a sill must heat the overlying ice for ~ 100 thousand years. To determine the sill lifetime, we first calculated if the water would convect. For a layer of fluid between parallel plates, convection will occur if the Rayleigh number, *Ra*, is greater than ~1000 (*Bejan,*1995). *Ra* for the sill is defined as:

$$Ra = \frac{g\rho_w a D^3 \Delta T}{\mu\kappa} \tag{21}$$

where a is the thermal expansion coefficient, D is the sill thickness, and ΔT is the temperature difference between the water and ice. Applying values expected for Europa of g = 1.3 m/s^2, ρ_w =

1000 kg/m^3, a = 10^{-4} 1/°C, D = 10 m, a small ΔT = 1°C, μ = 10^{-3} Pa s, and κ = 10^{-7} m^2/s, a Ra = 10^{13} results and indicates convection. Heat lost over time, τ_s, then follows the relationship:

$$q \sim \frac{k\Delta T}{D} Ra^{1/3} \tag{22}$$

$$\tau_s \approx \frac{\rho_w L D}{q} \tag{23}$$

where q is heat out, k is the thermal conductivity and L is the latent heat. Calculations show sill lifetime for a 10 - 100 m thick sill to be on the order of ~ 10 hours to a few days for k = 0.5 W/(m °C) and L = 3.3 x 10^3 J/kg. These are much shorter lifetimes than the ~ 100 kyrs suggested as needed to thin the overlying lithosphere for double ridge flexure formation. A thicker sill and/or replenishment of the sill with the warmer ocean water from below may increase the lifetime. These possibilities are explored further in the following discussion section.

3.5 Discussion

In this project, we suggested a mechanism for emplacing a shallow water sill in Europa's ice shell and investigated three essential components of the process to assess its viability: (1) vertical water flow speed, (2) horizontal fracture propagation and (3) sill lifetime. With a vertical fracture in place, ocean water driven by the ice layer overburden can flow up to a shallow depth below the surface (up to about neutral buoyancy at 1 km depth). We find that the flow of water up the ~ 10 km tall fracture will be subsonic and turbulent at an estimated upper-end speed of ~ 100 m/s. The actual water velocity will flow at a somewhat slower speed, however, due to the friction along the fracture walls and the fact that driving pressure will

decrease as the flow moves upwards. An average between the velocity of 100 m/s at the initial driving pressure and the final velocity of ~50 m/s (approximated at ~ 2 km depth) at the lower driving pressure is about 75 m/s. An average speed horizontally within the fracture will range from ~ 50 m/s at the base to ~ 25 m/s at 2 km depth. An overall average speed is then approximately 50 m/s. At this lower estimated vertical velocity, the time for the water to reach a shallow depth of a couple kilometers is only about 3.33 minutes. At the slowest speed of 25 m/s, the water would reach the shallow subsurface in ~ 6.66 minutes. These times are much shorter than the estimated conductive lifetime of ~ 3 years.

In considering turbulent fluid flow, eddies occur that decrease flow speed within a thin layer near the fracture walls. For fluid flows, research shows that eddies essentially increase the viscosity of the flow, though the effects are non-linear and difficult to estimate. Typically, wind-tunnel tests are performed or in-situ data is collected to determine turbulent eddy viscosity and its effects. For this analysis, we determine that the fluid flow will have to reach a very slow speed of ~ 8 x 10^{-5} m/s to take the ~ 3 years of conductive lifetime to reach the ~ 2 km deep location. The turbulent eddies should not decrease the flow to such an extreme and therefore complete freezing will not occur before the ocean water reaches the shallow subsurface.

Once the water reaches a shallow depth within the ice shell, a change in the surrounding stress field could cause the water to fracture the ice in a more horizontal direction. We applied finite element models to determine the effects of mechanical layering, shallow surface cracks, multiple deep crack events, and the combination of shallow and deep cracks on the stress field near the central fracture (Figures 3.7-3.13). In all model cases, the stress surrounding the crack is tensile and high enough to overcome the ice tensile strength in order to initiate a crack. Results of the mechanical layering model showed that increased porosity in the shallow subsurface and

briny ice in the deeper layers are two possible factors that can change the overall stress field to one that enables a turn in propagation direction towards horizontal as the fracture crosses the material contact. Our analyses, however, requires further work to determine the action of the crack after crossing the contact.

Three additional models considered the effects of shallow and/or deep cracks. Model 2 with shallow cracks only resulted in a slight propagation direction turn and short horizontal propagation distance. Model 3 with deep cracks only, resulted in a larger propagation direction turn, but only a small horizontal propagation distance. Last, results for Model 4, that contains both shallow and deep cracks, showed a significant fracture propagation turn towards horizontal out to a distance of ~ 250 m. This result is promising and the effect of distance between the shallow and deep cracks will be analyzed further in future work to determine if a certain crack spacing might enable ~ km wide sills.

The last factor investigated for sills related to double ridge flanking fracture formation was sill lifetime. *Dombard et al.* [2013] finds that a shallow sill, ~ 1 km below the surface, needs to transfer heat to the overlying brittle layer for thousands of years to cause appropriate thinning. However, our analysis finds that an ~ 10 – 100 m thick sill will convect and transfer all it's heat out in a matter of ~10 hrs to a few days. The fracture may remain open to the ocean for a period of time that would allow water replenishment and extend the sill lifetime. Brine formation during freezing of the sill edges could possibly drive replenishment and assist with keeping the fracture open.

The stress field could also be altered by the thickening of the brittle-elastic layer with increasing distance from the warm vertical fracture, similar to a mechanism suggested by *Grandin et al.* [2012] for lateral dike propagation beneath terrestrial rifts and mid-ocean ridges.

There, thickening of the brittle crust thickness with increased distance from the magma source induces a horizontal stress gradient that *Grandin et al.* [2012] suggests causes the lateral dike propagation. This mechanism could occur on Europa where the transition between elastic and ductile ice that occurs at around 1-2 km below the surface and the brittle ice layer thickens with increasing horizontal distance from the warmer, fluid-filled vertical fracture. This mechanism was not investigated here, but will be explored further in future analyses.

3.6 Conclusions

Overall, our analyses show that the emplacement of a shallow, ~ few km wide sill with a lifetime on the order of 1000s of years in Europa's ice shell proves challenging but shows promise. Fracturing from the shallow subsurface (as analyzed by *Manga and Wang* [2007]) enables ocean water to reach the shallow subsurface before freezing would occur (flow velocity analysis in Section 3.2). Finite element models show that the stress field surrounding a fracture in Europa's ice shell would be tensile and at levels greater than the tensile strength of ice at 10^4 to 10^6 Pa. Also, a change in stress field due to mechanical layering and/or shallow and deep subsurface cracks could enable horizontal fracture propagation (Section 3.3). Mechanisms such as that suggested by *Grandin et al.* [2012] warrants further analysis to determine the ability to enable horizontal fracturing. The greatest challenge for sill emplacement and contribution to double ridge flanking fractures, however, lies in the short sill lifetime (~ days; see Section 3.4) compared to the needed 1000s of years to achieve adequate thinning of the overlying lithosphere (as determined by *Dombard et al.* [2013]).

Tables

Table 3.1 Symbols – Roman characters

Symbol	Definition	Value	Units
a	thermal expansion coefficient	10^{-3}	1/C
B	bulk modulus of water	2.2×10^{9}	Pa
c	speed of sound in water	~ 1500	m/s
D	sill thickness	10 - 100	m
d	depth	varies	m
E	Young's modulus of ice	5.00E+09	Pa
E^*	Plane-strain Young's modulus	$= E/(1-v)$	Pa
f	body forces	n/a	varies
G	ice shear modulus (*Weeks and Assur* 1967)	2	GPa
g	acceleration due to gravity	1.3	$m\ s^{-2}$
l	dike height	~ 10	km
K	Stress intensity factor	n/a	$Pa\ m^{1/2}$
K_c	Critical stress intensity factor	n/a	$Pa\ m^{1/2}$
K_I	Mode I stress intensity factor	Equations 18 & 19	$Pa\ m^{1/2}$
K_{Ic}	Mode I critcal stress intensity factor	varies	$Pa\ m^{1/2}$
k	thermal conductivity	0.5	$W\ (m\ C)^{-1}$
L	latent heat	3.3×10^{3}	$J\ kg^{-1}$
P	pressure	varies	Pa
P_0	pressure at ice shell base	Equation 1	Pa
P_f	fracture internal fluid pressure	Equation 17	Pa
q	heat out	Equation 21	$W\ m^{-2}$
Ra	Rayleigh number	Equation 21	n/a
Re	Reynolds number	Equation 5	n/a
ΔT	Temperature difference	1	C
T_0	Tensile strength of host medium (ice)	10^4 to 10^6	Pa
t	time	n/a	s
v_{max}	fluid velocity at fracture base	Equations 6, 10 & 12	$m\ s^{-1}$
w	fracture width	10 to 100	m
y	vertical direction	n/a	n/a
z	direction into page	n/a	n/a

Table 3.2 Symbols – Greek characters and other

Symbol	Definition	Value	Units
α	Dundur parameter - difference in extensional or uniaxial stiffness	Equation 14	n/a
β	Dundur parameter - volumetric or areal stiffness mismatch	Equation 15	n/a
κ	thermal diffusivity of water (*Blumm et al.*, 2007)	10^{-7}	$m^2 s^{-1}$
μ	dynamic viscosity of water	10^{-3}	Pa s
ν	Poisson's ratio for ice	0.3	n/a
ρ_{ice}	density of ice	900	kg m^{-3}
ρ_w	density of water	1000 or 1200	kg m^{-3}
σ	stress	varies	Pa
σ_L	vertical lithostatic stress	$\rho_{ice} gD$	Pa
σ_{Ln}	lithostatic load normal to direction of propagation	varies	Pa
σ_t	crack tip stress	varies	Pa
σ_x	horizontal stress	Equation 4	Pa
σ_y	vertical stress	varies	Pa
σ_3	least compressive principal stress/ maximum tensile principal stress	varies	Pa
τ_d	dike heat transfer time	Equation 2	s
τ_s	sill heat transfer time	Equation 23	s
subscript 1	layer 1 - top layer		
subscript 2	layer 2 - bottom layer		

Figures

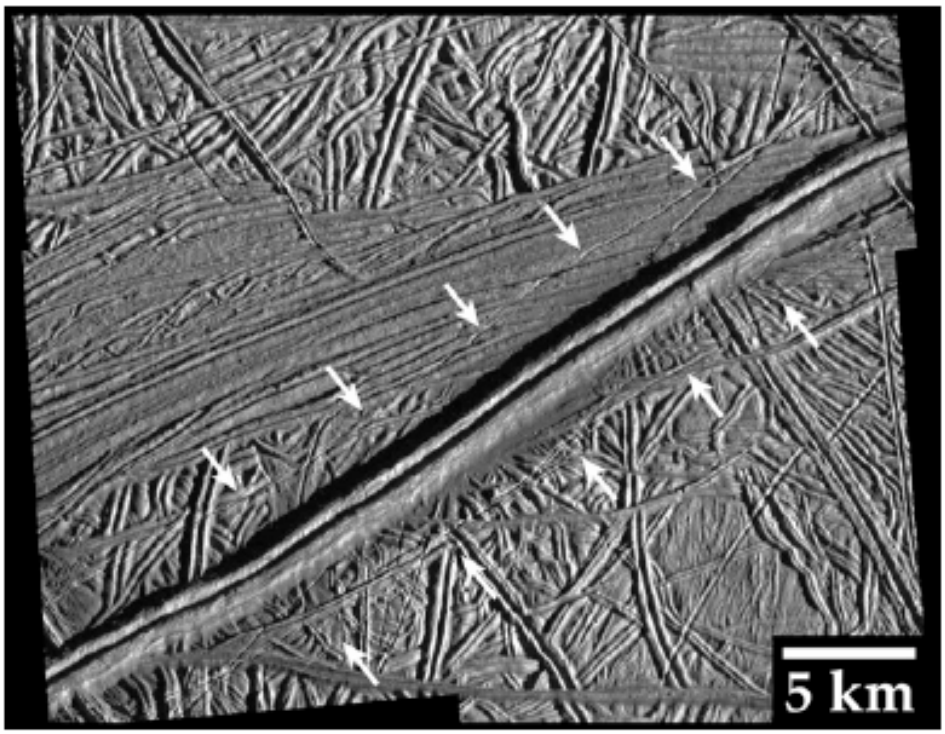

Figure 3.1 Image of the Androgeos Linea double ridge morphology on Europa's surface (14.7°N 273.4°W). Arrows indicate the locations of flanking, subparallel fractures. (From *Dombard et al.*, 2013)

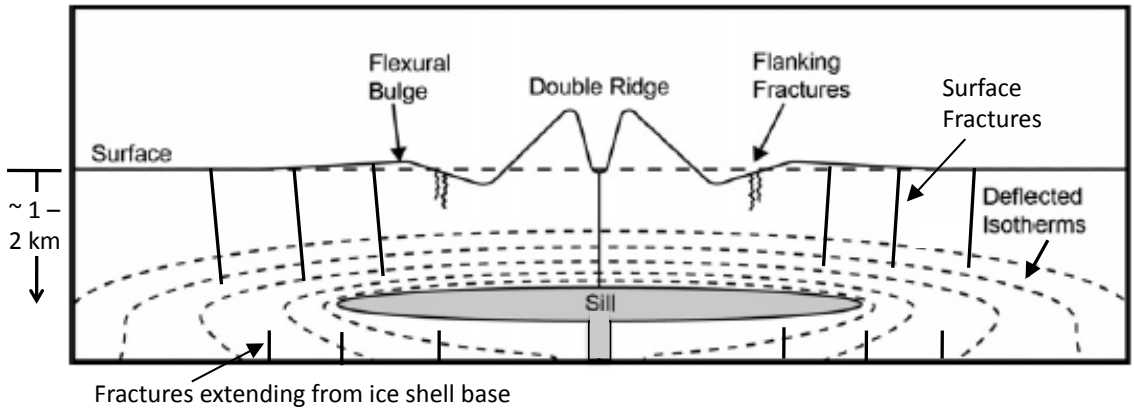

Figure 3.2 Cross-sectional sketch of the double ridge morphology (modified from *Dombard et al.*, 2013) showing a shallow (~1 - 2 km deep) cryomagmatic sill in the subsurface. As modeled by *Dombard et al.* (2013), heat transferred from the sill (represented by dashed isotherms) locally thins the overlying ice layer and enables surface flexure and formation of flanking fractures from ridge loading.

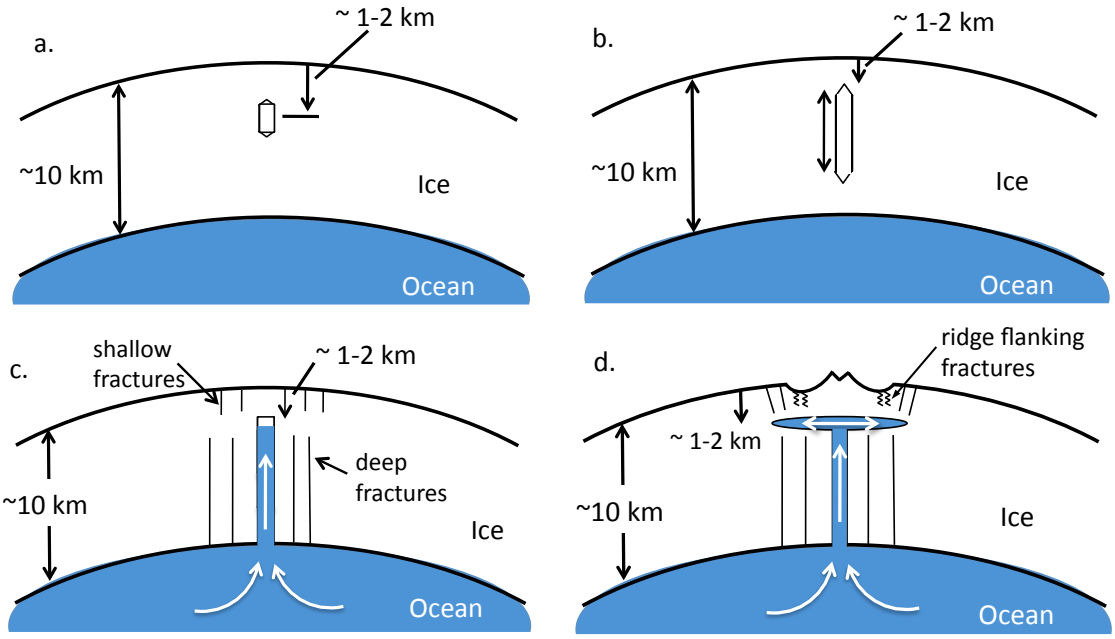

Figure 3.3 Sill emplacement steps: a. Stress grows in cooling, thickening ice shell and vertical fracture initiates; b. Vertical fracture propagates up and down; c. Fracture reaches ocean and water flows up to ~ 1-2 km depth; d. Sill grows horizontally through fracturing

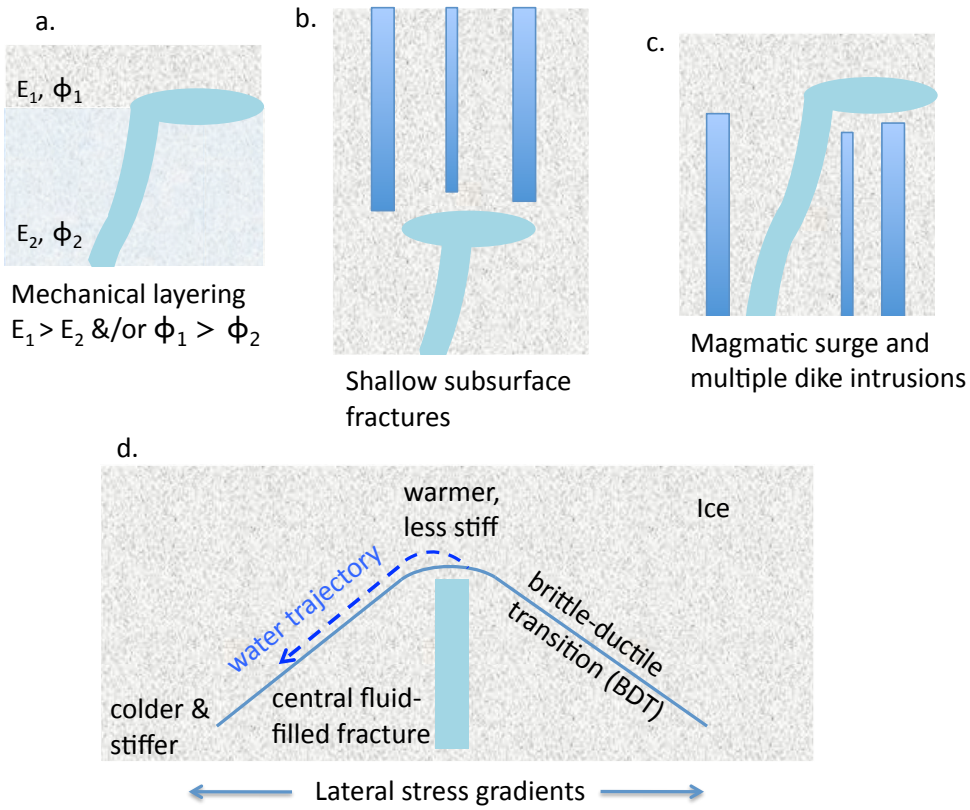

Figure 3.4 Sill emplacement mechanisms: a. Mechanical layering, b. Shallow cracks, c. Deep cracks, d. Thickening of brittle-ductile layer

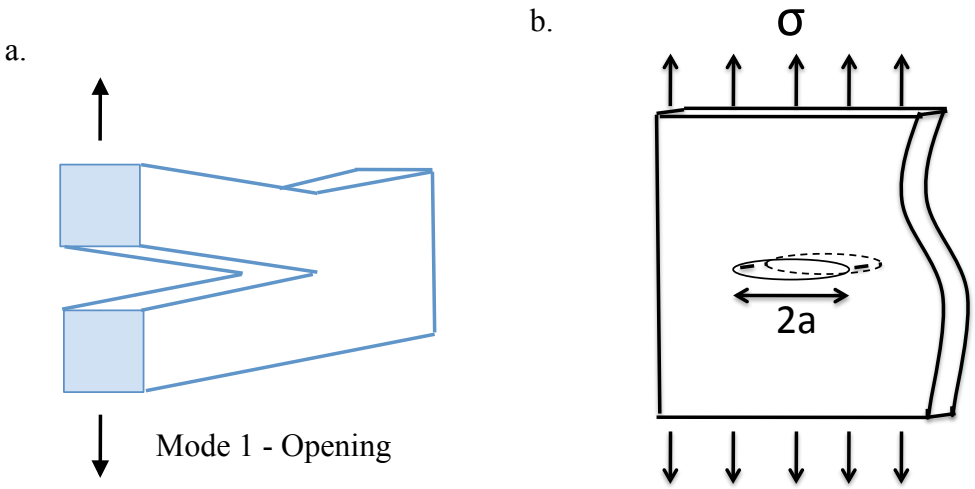

Figure 3.5 a. Shows Mode I – opening fracture type **b.** Through crack in infinite plate

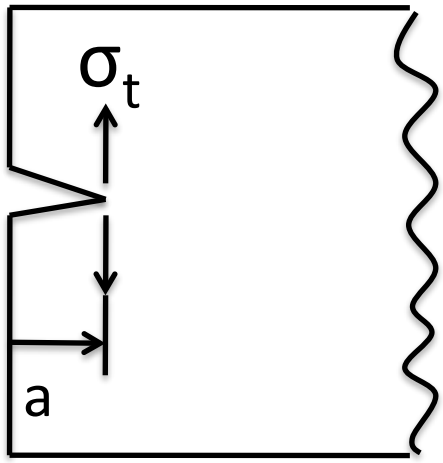

Figure 3.6 Edge crack in semi-infinite plate – could represent start of horizontal sill off vertical fracture into ice shell. a is the crack length and σ_t is the opening stress at the crack tip that must be greater than the lithostatic load + tensile strength of ice (see Equation 18).

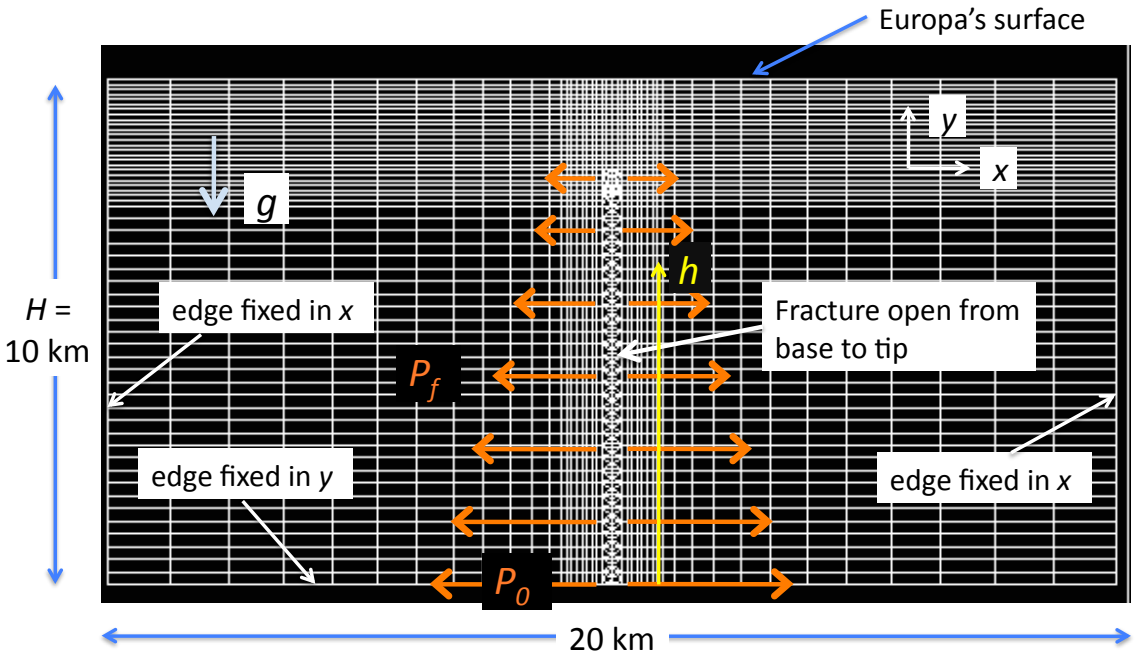

Figure 3.7 Base model setup. 10 km x 20 km grid representing the ice shell on Europa. A vertical fracture extends from the base edge to 2 km below the surface and is pressurized hydrostatically, P_f, starting at $P_0 = \rho_{ice}gH$ at the base, then decreasing as $P_0 - \rho_w gh$. Remaining pressure may drive horizontal fracturing if a change in stress field is encountered.

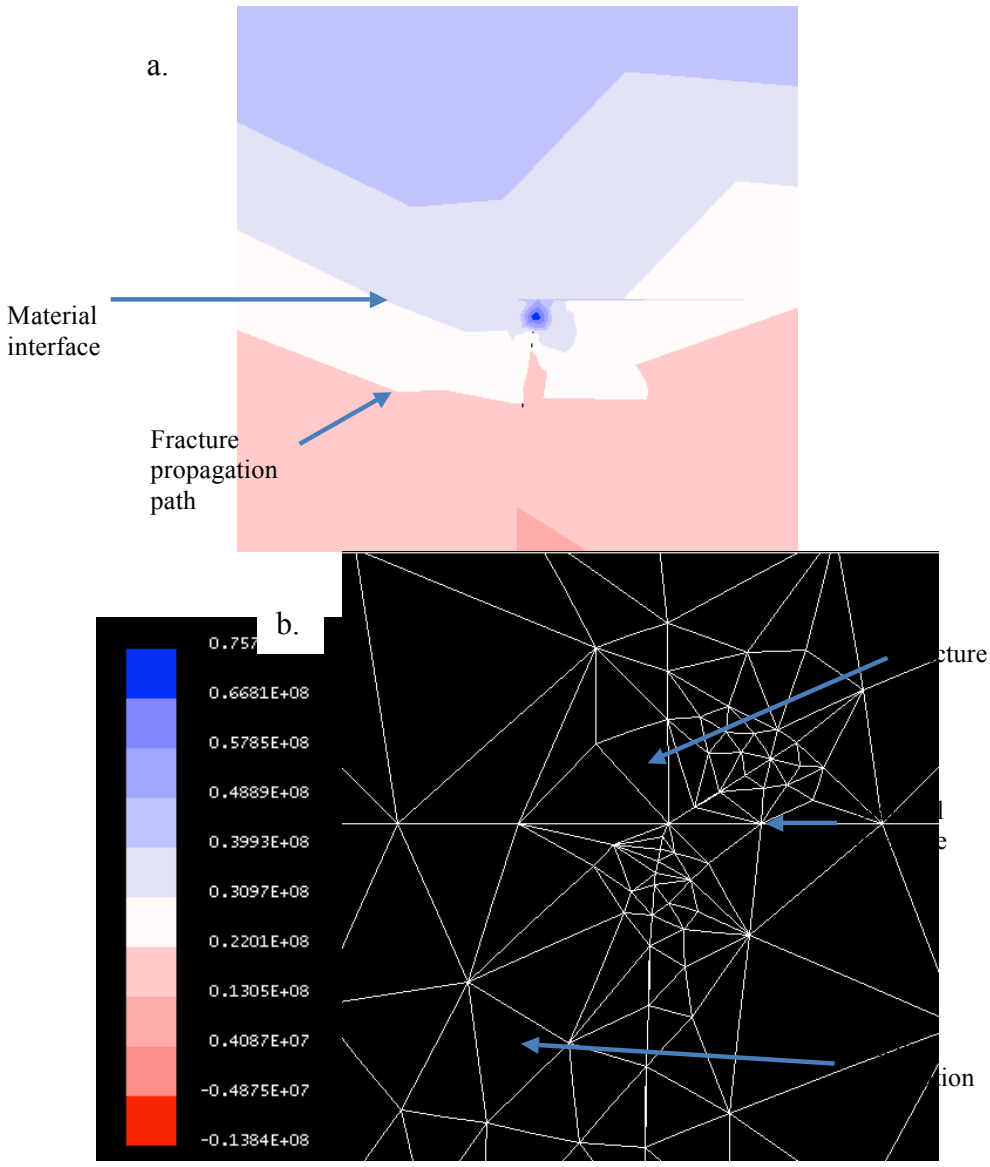

Figure 3.8. Mechanical layering model. Uppermost 2 km have a density of ρ_{pi} = 855 kg/m^3 to represent a porosity of ϕ = 0.05 [*Nimmo et al.,* 2003] and the lower 8 km material has a density of ρ_{bi} = 1120 kg/m^3 to represent briny ice [*Williams and Greely*, 1998]. The top layer has a Young's modulus of E_1 = 5e11 Pa to represent a stiffer, colder upper layer and the lower layer has E_2 = 5e9 Pa [*Haynes,* 1978]. **a.** σ_1 field around fracture at 2005 m depth (just below material interface) **b.** One can note the turn in the fracture direction just before the material interface and the increased turn after crossing the interface. Franc2d does not allow further computation after the interface crossing.

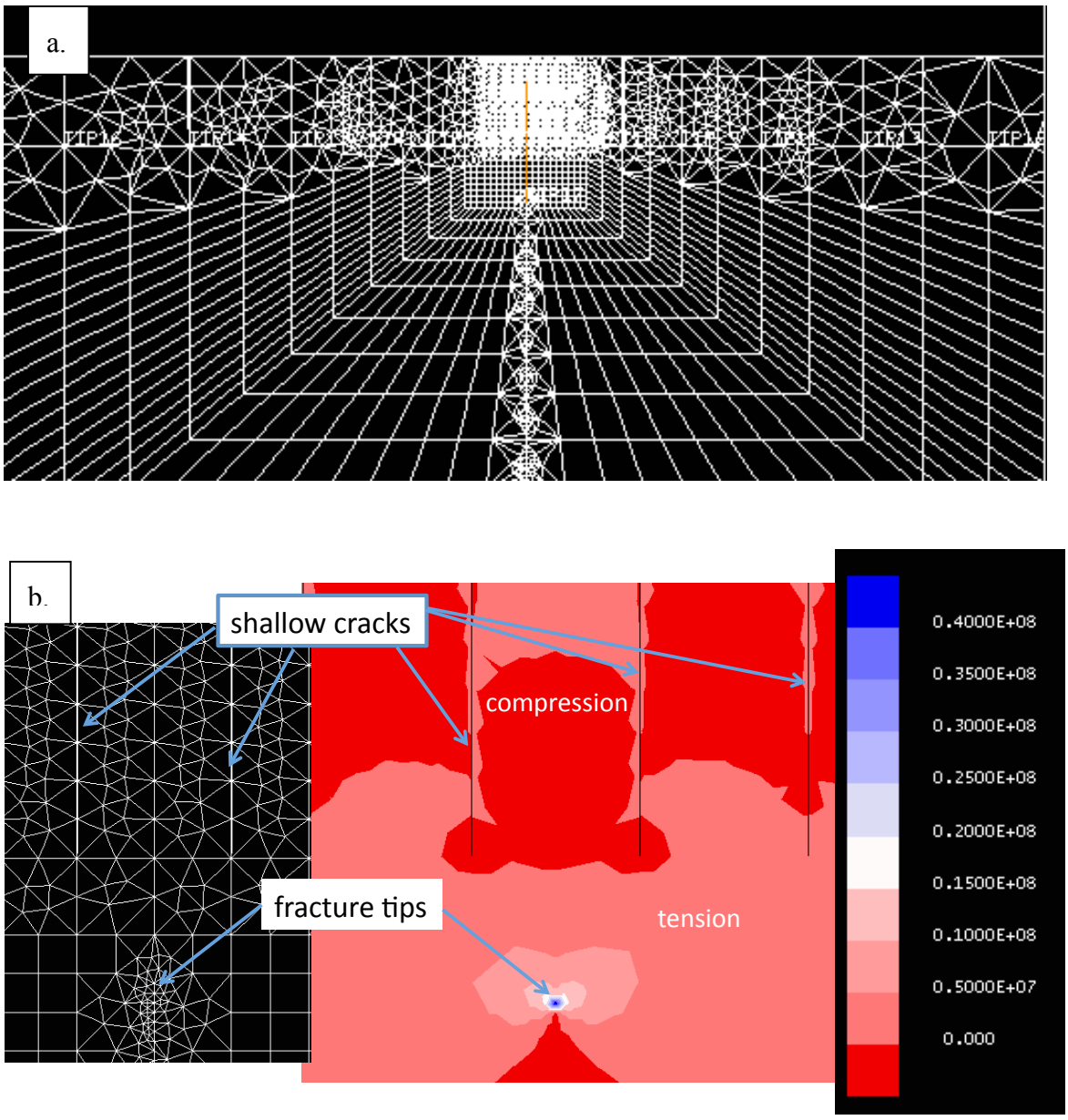

Figure 3.9. Shallow subsurface crack model: 16 cracks from surface to 1500 m depth. **a.** Orange line shows propagation direction when tip of central, pressurized fracture is at 2400 m depth. **b.** Fracture only turns slightly to left (< 1m) when approaching base of crack tips

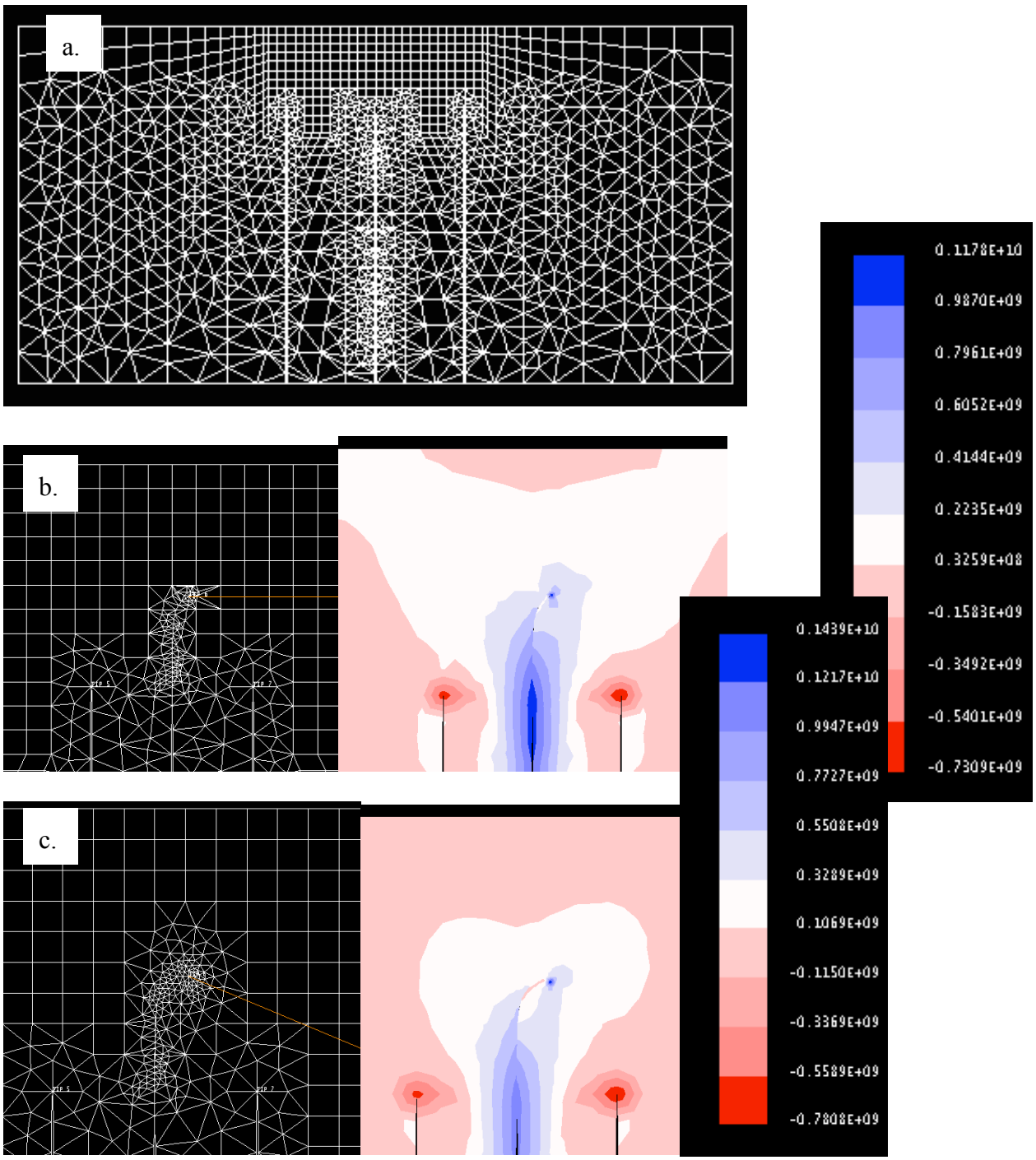

Figure 3.10 a. Deep crack model with cracks reaching up to 2300 m depth and central, pressurized fracture tip at 2500 m depth. **b.** Fracture propagates upwards until turning horizontal at depth of ~ 1360 m (orange line indicates direction of further propagation). Right side shows contour of principal stress, σ_1, with positive values denoting tensile stress and negative values indicating compressive stresses. **c.** propagates one step horizontally (100 m step size), then turns downward (orange line indicates direction). Right side shows contour of principal stress, σ_1 (sign convention same as for b.)

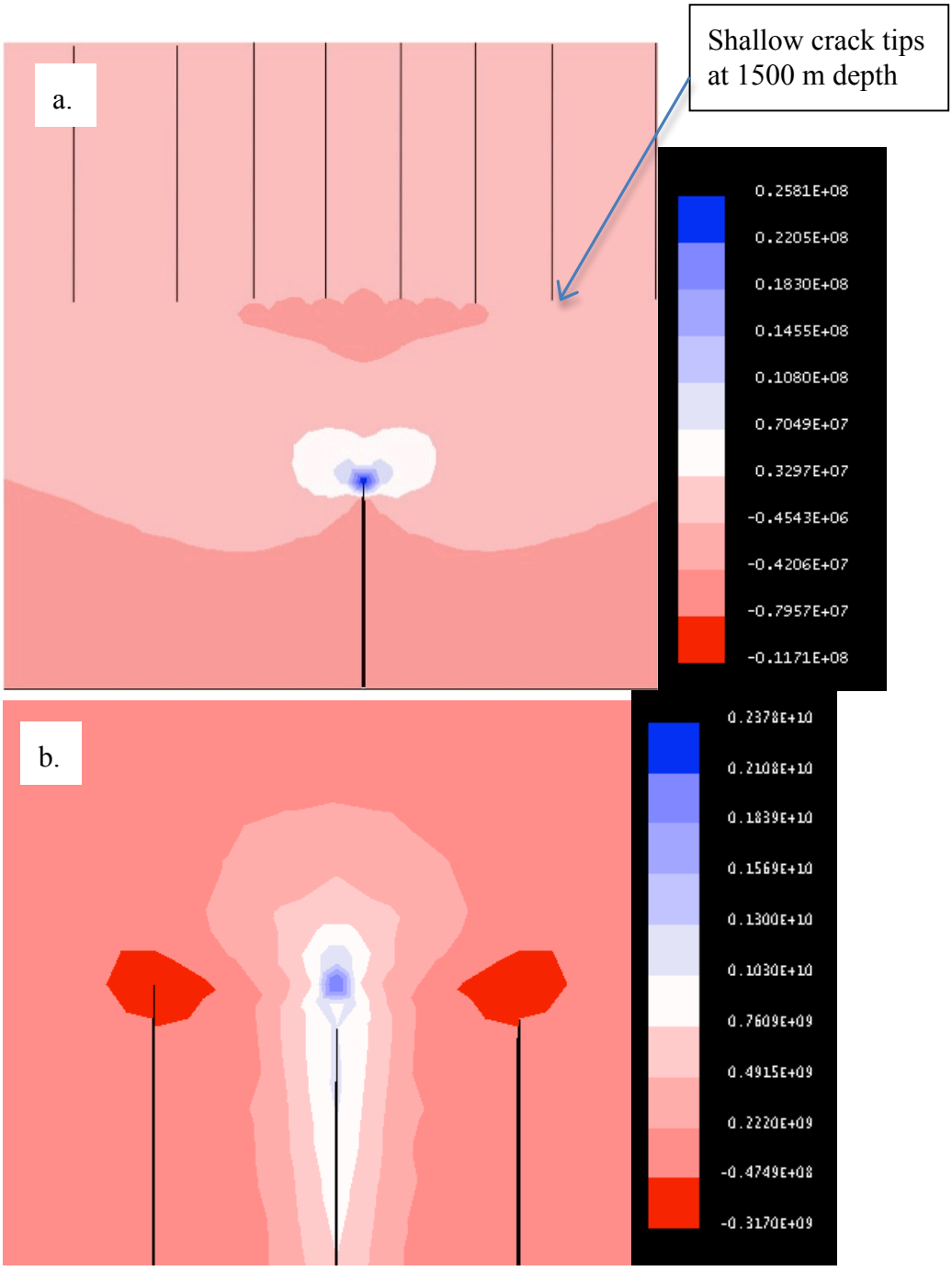

Figure 3.11 Zoomed in view of σ_1 values for the **a.** Shallow crack model **b.** Deep crack model Central fracture tip is located at (0, -2400m) (Positive values = tensile, negative values = compressive)

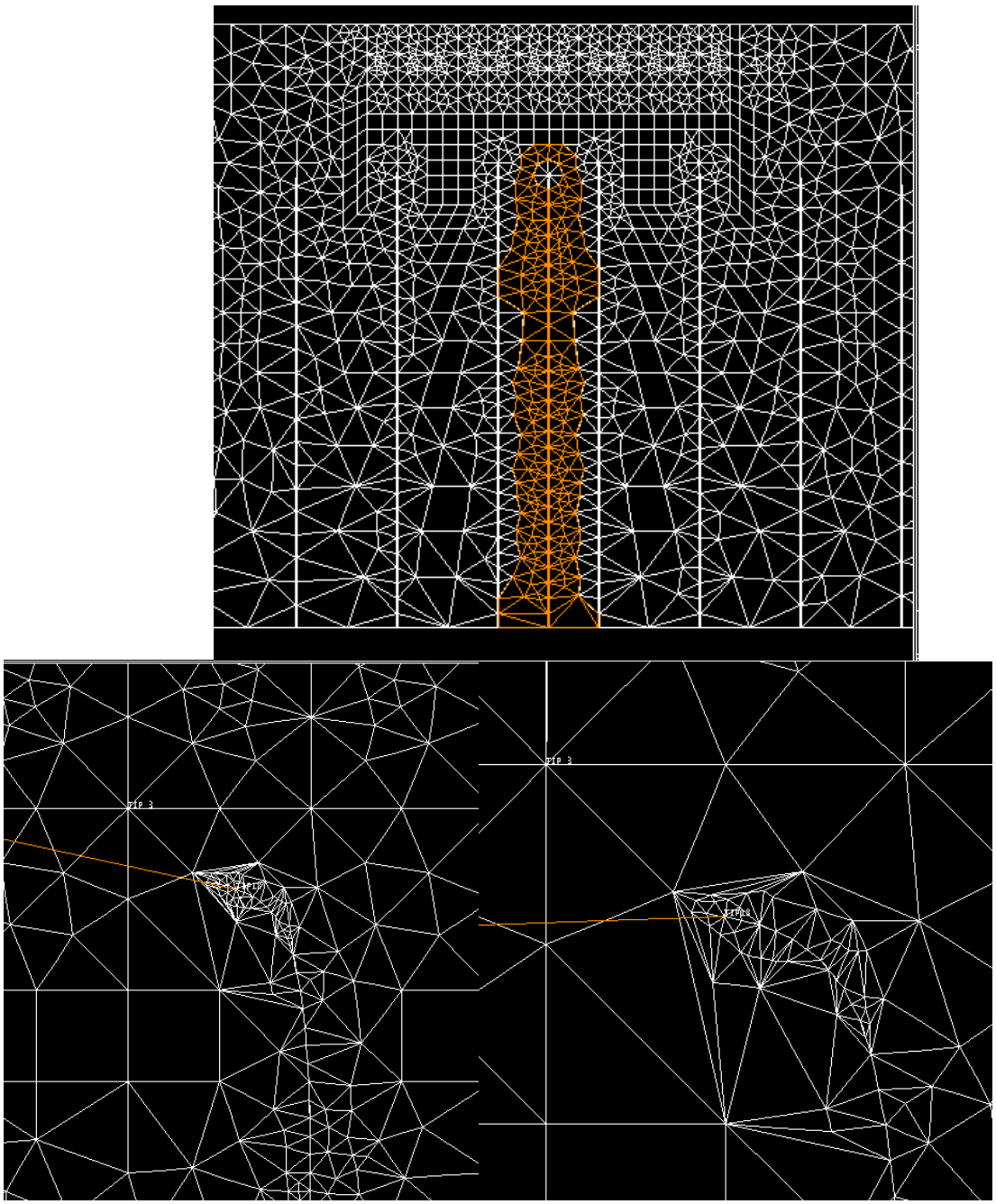

Figure 3.12 a. Shallow and Deep Cracks model. Orange mesh shows area around central fracture. **b.** Propagation path of central fracture nearing subsurface crack (orange line indicates direction of propagation) **c.** After reaching ~ 250 m of horizontal propagation distance, the propagation begins to occur in a downward direction but continues to propagate until ~ 400 m horizontally.

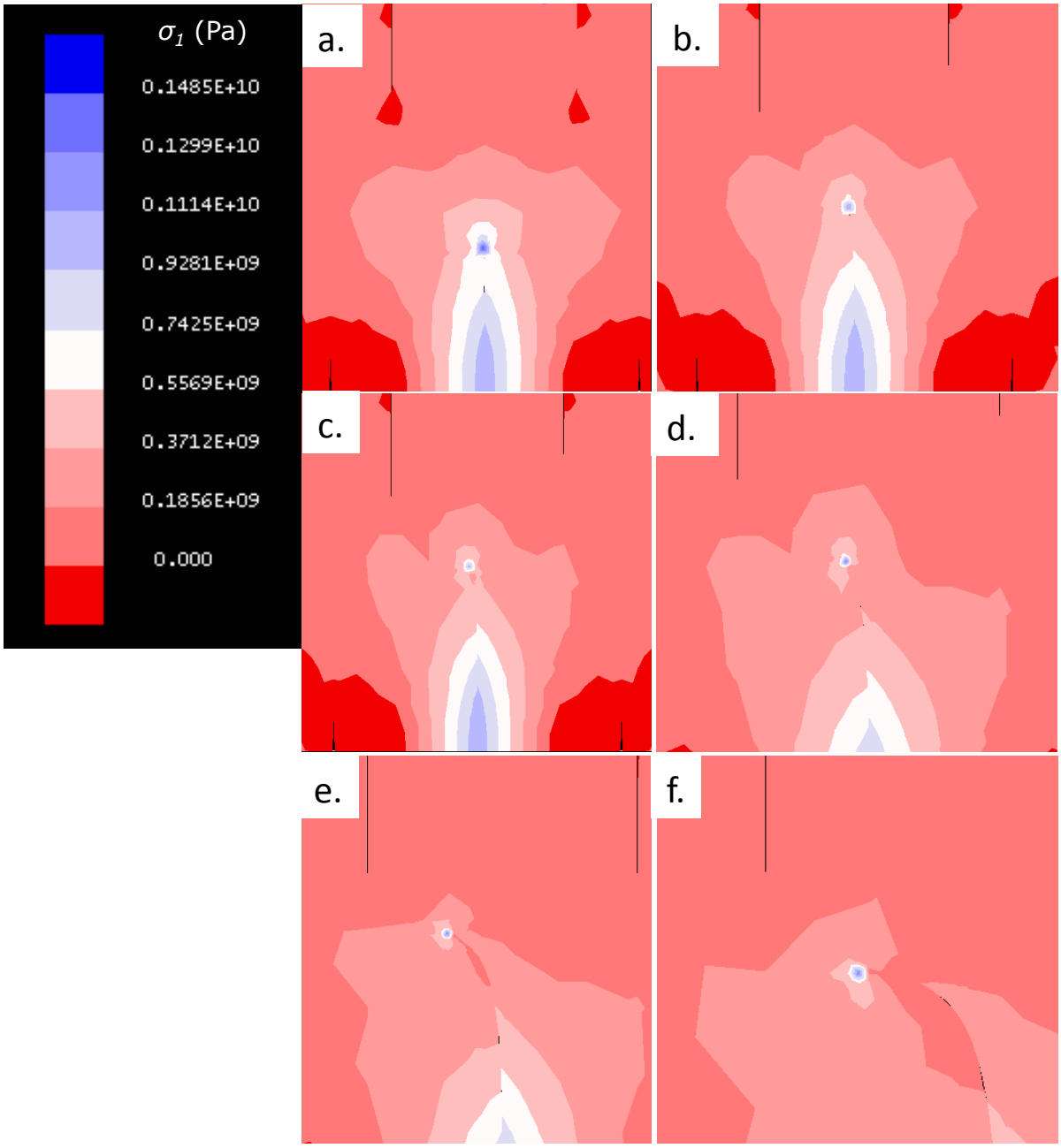

Figure 3.13 σ_1 field for propagation of fracture in the Shallow and Deep Cracks model. Fracture begins propagation at (0, -2400). Depths of fracture tip at: **a.** -1700 m **, b.** -1501 m, **c.** -1403 m. **d.** Fracture begins traversing horizontally around this depth. Fracture tip is at: (-86, -1311), **e.** (-203, -1222) **f.** (-302, -1213)

References

Anderson, T. L. (2005), *Fracture Mechanics*, 3rd ed., 621 pp., Taylor and Francis Group, Boca Raton.

Bejan, A. (1995), Convection Heat Transfer, 2nd ed., 639 pp., Wiley, New York.

Billings, S. E. and S. A. Kattenhorn (2005), The great thickness debate: Ice shell thickness models for Europa and comparisons with estimates based on flexure at ridges, *Icarus, 177*, 397-412.

Black, G. J., D. B. Campbell, S. J. Ostro (2001), Icy Galilean satellites: Modeling radar reflectivities as a coherent backscatter effect, *Icarus, 151*, 167-180.

Blumm, J., A. Lindemann and S. Min (2007), Thermal characterization of liquids and pastes using the flash technique, *Thermochimica Acta*, *455,* 26-29.

Brown, M. E. and K. Hand (in press), Salts and radiation products on the surface of Europa, *Astrophysical Journal.*

Cammarano, F., V. Lekic, M. Manga, M. Panning, and B. Romanowicz (2006), Long-period seismology on Europa: 1. Physically consistent interior models, *J. Geophys. Res. (Planets), 111*, E12009.

Collins, G. C. et al. (2000), Evaluation of models for the formation of chaotic terrain on Europa, *J. Geophys. Res., 105*, E1, 1709-1716.

Crawford, G. D. and D. J. Stevenson (1988), Gas-driven water volcanism and the resurfacing of Europa, *Icarus*, *73*, 66-79, 10.1016/0019-1035(88)90085-1

Dempsey, J. P., R. M. Adamson, and S. V. Mulmule (1999), Scale effects on the in-situ tensile strength and fracture of ice. Part II: First-year sea ice at Resolute, N. W. T., *Int. J. Fract., 95*, 347– 366.

Dombard, A. J., G. W. Patterson, A. P. Lederer and L. M. Prockter (2013), Flanking fractures and the formation of double ridges on Europa, *Icarus, 223,* 74-81.

Dombard, A.J., G. W. Patterson, L. M. Prockter (2007), Sill injection on icy satellites inferred from ridge-induced flexure on Europa, *Eos (Fall Suppl.), 88*, P21B-0549.

Dundurs, J. (1969), Edge-bonded dissimilar orthogonal wedges, *J. App. Mech., 36,* 650-652.

Fagents, S. A. (2003), Considerations for effusive cryovolcanism on Europa: the post-Galileo perspective, *J. Geophys. Res., 108, E12,* 5139, doi:10.1029/2003JE002128.

Fialko, Y. (2001), On origin of near-axis volcanism and faulting at fast spreading mid-ocean ridges, *Earth and Planet. Sci. Lett., 190*, 31-39.

Freund, L. B. and S. Suresh (2003), *Thin film materials: Stress, defect formation and surface evolution*, 750 pp., Cambridge University Press, Cambridge.

Gaidos, E. J. and F. Nimmo (2000), Tectonics and water on Europa, *Nature, 405,* 637.

Golombek, M. P. and W. B. Banerdt (1990), Constraints on the subsurface structure of Europa, *Icarus, 83* 441-452.

Grandin et al. (2012), Elastic thickness control of lateral dyke intrusion at mid-ocean ridges, *Earth and Planet. Sci. Lett., 319-320*, 83-95.

Greenberg et al. (1998), Tectonic processes on Europa: tidal stresses, mechanical response, and visible features, *Icarus, 135*, 64-78.

Gudmundsson, A. (2011), Rock Fractures in Geological Processes, Cambridge University Press, Cambridge, UK.

Gudmundsson, A. and S. L. Brenner (2004), How mechanical layering affects local stresses, unrests, and eruptions of volcanoes, *Geophys. Res. Lett., 31*, 10.1029/2004GL020083

Han, L. and A. P. Showman (2008), Implications of shear heating and fracture zones for ridge formation on Europa, *Geophys. Res. Lett., 35*, L03202, doi:10.1029/2007GL031957.

Hansen, D. M. and J. Cartwright (2006), Saucer-shaped sill with lobate morphology revealed by 3D seismic data: implications for resolving a shallow-level sill emplacement mechanism, *J. Geol. Soc., London, 163*, 509-523.

Haynes, J. (1978), Effect of Temperature on the Strength of Snow-Ice, *USA CRREL Rep. 78-27*, Cold Reg. Res. and Eng. Lab., Hanover, N.H.

He, M. Y. and J. W. Hutchinson (1989), Crack deflection at an interface between dissimilar elastic materials, *International J. Solids and Structures, 25,* 1053-1067.

Head, J. W., R. T. Pappalardo, and R. Sullivan (1999), Europa: Morphological characteristics of ridges and triple bands from Galileo data (E4 and E6) and assessment of a linear diapirism model, *J. Geophys. Res., 104*, E10, 24223-24236.

Hoppa, G. et al. (2000), Distribution of strike-slip faults on Europa, *J. Geophys. Res., 105,* E9, 22617-22627.

Hurford, T. A. et al. (2005), Flexure of Europa's lithosphere due to ridge-loading, *Icarus, 177*, 380-396.

Hutchison, J. W. (1996), Stresses and failure modes in thin films and multilayers, *Notes for a DCAMM Course,* Lyngby: Technical Univ. of Denmark, 1-45.

Ildefonse, B., A. Nicolas, F. Boudier (1993), Evidence from the Oman ophiolites for sudden stress changes during melt injection at oceanic spreading centers, *Nature, 366,* 673-675.

Kadel, S. D., S. A. Fagents, R. Greeley, and the Galileo SSI Team (1998), Trough-bounding ridge pairs on Europa – Considerations for an endogenic model of formation, *LPSC XXIX,* Abstract #1078, LPI, Houston, TX.

Kavanagh, J. L., T. Menand and R. S. J. Sparks (2006), An experimental investigation of sill formation and propagation in layered elastic media, *Earth and Planet. Sci. Lett., 245,* 799–813.

Kelemen, P. B., K. Koga, N. Shimizu (1997), Geochemistry of gabbro sills in the crust-mantle transition zone of the Oman ophiolites: Implications for the origin of the oceanic lower crust, *Earth Planet. Sci. Lett., 146*, 475-488.

Kent, G. M., S. C. Singh, A. J. Harding, M. C. Sinha, J. A. Orcutt, P. J. Barton, R. S. White, S. Bazin, R. W. Hobbs, C. H. Tong and J. W. Pye (2000), Evidence from three-dimensional seismic reflectivity images for enhanced melt supply beneath mid-ocean-ridge discontinuities, *Nature, 406*, 614 - 618.

Kim, J. W., S. Bhowmick, I. Hermann and B. R. Lawn (2006), Transverse fracture of brittle bilayers: relevance to failure of all-ceramic dental crowns, *J. Biomed. Mat. Res., 79B*, 58-65.

Kuskov, O. L., Kronrod, V. A. (2005), Internal structure of Europa and Callisto, *Icarus, 177*, 550–569.

Lee, S., R. T. Pappalardo, and N. C. Makris (2005), Mechanics of tidally driven fractures in Europa's ice shell, *Icarus, 177,* 367-379.

Lucchitta, B.K., Soderblom, L.A. (1982), Geology of Europa, in *Satellites of Jupiter*, ed. Morrison, D., Univ. of Arizona Press, Tucson, AZ, pp. 521–555.

Manga, M. and C.-Y. Wang (2007), Pressurized oceans and the eruption of liquid water on Europa and Enceladus, *Geophys. Res. Lett., 34,* L07202, doi:10.1029/2007GL029297.

Nimmo, F. (2004), Stresses generated in cooling viscoelastic ice shells: Application to Europa, *J. Geophys. Res.*, *109*, E12001, doi:10.1029/2004JE002347.

Nimmo, F. and E. Gaidos (2002), Strike-slip motion and double ridge formation on Europa, *J. Geophys. Res., 107,* E4*,* 5021, doi:10.1029/2000JE001476.

Nimmo, F., R. T. Pappalardo, and B. Giese (2003), On the origins of band topography, Europa, *Icarus, 166,* 21-32.

Olson, J. E. and D. D. Pollard (1991), The initiation and growth of en échelon veins, *J. Struct. Geol., 13,* no. 5, 595-608.

Pappalardo et al. (1999), Does Europa have a subsurface ocean? Evaluation of the geological evidence, *J. Geophys. Res., 104,* E10, 24015-24055.

Pappalardo, R. and M. D. Coon (1996), A sea ice analog for the surface of Europa, *LPSC XXVII,* abstract #1499, LPI, Houston, TX.

Pollard, D. D. (1987), Elementary fracture mechanics applied to the structural interpretation of dykes, in *Mafic Dyke Swarms*, edited by H. C. Halls and W. H. Fahrig, *Geol. Assoc. Can. Spec. Pap., 34*, 5–24.

Rathbun, J.A., Musser Jr., G.S., Squyres, S.W., 1998. Ice diapirs on Europa: Implications for liquid water. *Geophys. Res. Lett, 25*, 4157–4160.

Rubin, A. M. (1995), Propagation of magma-filled cracks. *Annu. Rev. Earth Planet. Sci., 23*, 287-336.

Ruiz, J. and R. Tejero (2000), Heat flows through the ice lithosphere of Europa, *J. Geophys. Res., 105,* E12, 29283-29289.

Ruiz, J. and R. Tejero (1999), Heat flow and brittle-ductile transition in the ice shell of Europa, *LPSC XXX,* abstract #1031, LPI, Houston.

Schenk, P. M. and W. B. McKinnon (1989), Fault offsets and lateral crustal movement of Europa: Evidence for a mobile ice shell. *Icarus, 79,* 75-100.

Sotin, C., G. Choblet, J. W. Head, A. Mocquet, G. Tobie (2004), Thermal evolution of Europa's icy crust. In: *Workshop on Europa's Icy Shell: Past, Present, and Future, LPI Contribution No. 1195*. LPI, Houston, pp. 84-85.

Thomson, K. (2007), Determining magma flow in sills, dykes and laccoliths and their implications for sill emplacement mechanisms, *Bull. Volcanol., 70*, 183–201.

Travis, B. J., J. Palguta, and G. Schubert (2012), A whole-moon thermal history model of Europa: Impact of hydrothermal circulation and salt transport, *Icarus, 218,* 1006-1019.

Tufts, B. R. (1998), Lithospheric displacement features on Europa and their interpretation, PhD thesis, University of Arizona, Tuscon.

Tufts, B. R. et al. (2000), Lithospheric Dilation on Europa, *Icarus, 146,* 75-97, doi:10.1006/icar.2000.6369.

Vance, S. and J. Goodman (2009), Oceanography of an ice-covered moon, in *Europa,* ed. R. T. Pappalardo, W. B. McKinnon, and K. Khurana, U. of Ariz. Press, Tucson., Tucson, AZ.

Wang, P. and L. R. Xu (2006), Dynamic interfacial debonding initiation induced by an incident crack, *International J. Solids and Structures, 43,* 6535-6550.

Wawrzynek, P. A. and A. R. Ingraffea (1987), Interactive finite element analysis of fracture processes: An integrated approach, *Theoret. App. Frac. Mech., 8,* 137-150.

Weeks, W. and A. Assur (1967), Mechanical properties of sea ice, Science/Engineering-2-C3, *Cold Regions Research and Engineering Lab,* Hanover, NH.

Williams, K. K. and R. Greeley (1998), Estimates of ice thickness in the Conamara Chaos region of Europa, *Geophys. Res. Lett., 25,* no. 23, 4273-4276.

Xu, L. R., Y. Y. Huang and A. J. Rosakis (2003), Dynamics of crack deflection and penetration at interfaces in homogeneous materials: experimental studies and model predictions, *J. Mechanics Physics of Solids*, *51*, 461-486.

4 Dike induced stress and permeability changes: Implications for hydrothermal fluid flux on Earth and Mars

Abstract:

We apply a finite element program to investigate the effects of dike propagation on permeability and stress in the adjacent crust on Earth and Mars. The model presented here provides a more complete picture of the effects of dike emplacement on stress and permeability change as a process for driving water and heat to the surface in terrestrial and Martian environments. Previous studies applied permeability change within a dike damage zone to assess fluid and heat outputs at mid-ocean ridges [*Germanovich et al.,* 2000; *Lowell and Germanovich*, 1995; *Germanovich et al.,* 2011] and beneath dike induced fissures on Mars [*Hanna and Phillips*, 2006]. By considering both damage zone increased permeability and dike induced decreases in permeability outside of the damage zone, our models determine where boundary layer will flow and assess if flow can occur at adequate rates and with sufficient volumes to produce the event plumes at terrestrial mid-ocean ridges and flooding events on Mars. Results determine that heat out for a 200 km long dike releasing heat over a day provides ~ 5 x 10^{16} J which falls within the expected event plume range of 10^{14} – 10^{16} J. Our models also find that flow next to a dike on Mars would occur mainly through the damage zone at adequate flow rates for formation of Athabasca Valles. Total volume required, however, requires recharging to occur between flood events. Comparison of stresses from dike emplacement with those calculated by Hanna and Phillips finds fairly good agreement.

4.1 Introduction

As mentioned previously, hydrothermal systems exist abundantly on Earth [e.g. *Lowell et al.*, 2008; *Germanovich et al.*, 2000] and likely exist on many planetary bodies in our solar system [*Gulick et al.,* 1997; *Craft and Lowell,* 2012]. Combining the hydrothermal circulation and fracture modeling methods applied in Chapters 2 and 3, dike-driven hydrothermal systems can be explored from the stage of initial dike emplacement through to the hydrothermally driven expulsion of water to the surface (or seafloor). Here, I apply finite element modeling to determine the change of permeability of the crust adjacent to a dike intrusion for both a terrestrial mid-ocean ridge system and an analogous system on Mars. Permeability change results are then applied in hydrothermal circulation models and used to determine the likelihood of dike formation as a driving mechanism for event plumes observed at mid-ocean ridges and for formation of fluvial features on Mars.

At mid-ocean ridges, large, sudden increases in heat output have been recorded during event plumes suggesting that an increase in permeability of the crust could enable increased fluid flow. *Lowell and Germanovich* [1995] and *Germanovich et al.* [2000] argue that during dike emplacement, a damage zone forms at the dike margins with greatly increased permeability and that the increased permeability along with thermal buoyancy can result in the formation of event plumes. Here we consider the effects of higher permeability along the dike margin as well as stress-induced permeability changes at a mid-ocean ridge following a diking event using the dike propagation approach of *Sim* [2004]. *Germanovich et al.* [2000] do not consider the effects of dike-induced compressive stresses on crustal permeability or pressurization of the crustal aquifer.

Dike intrusion has also occurred on Mars and hydrothermal activity likely resulted at some

locations over Mars's history and possibly also in the geologically recent past. Evidence of hydrothermal activity includes observations of abundant volcanic formations and orbiter and rover observations of deposits indicated to be of hydrothermal origin [e.g. *Murchie et al.*, 2007; 2009; *Bibring et al.*, 2004; *Squyres et al.,* 2008; *Yen et al.,* 2008; *Schmidt et al.,* 2008]. The largest volcano in the solar system, Olympus Mons, resides on Mars along with many others. Geologically recent volcanic activity has also occurred, with surface evidence suggesting volcanic flows as recent as within the last few tens of millions of years [*Hauber et al.,* 2011]. Morphology also suggests dikes have propagated near the volcanic uplift regions, forming faults, fissures and grabens [e.g. *Wilson and Head*, 2002]. The dikes may have induced circulation of subsurface water (ice and/or liquid) forming a hydrothermal system capable of driving water to the surface and forming morphology observed there [e.g. *Craft and Lowell*, 2012].

Our second investigation focuses on the Athabasca Valles region of Mars (Figure 4.1) that was likely carved out by groundwater flooding episodes emanating from fissures formed by subsurface dike emplacements [*Burr et al.,* 2002a; *Head et al.*, 2003]. This work stems in part from the analysis of *Hanna and Phillips* [2006] who modeled the stresses resulting from an ~ instantaneous dike emplacement and the ensuing pore pressure distribution to determine if a sufficient amount of water could be rapidly forced to the surface to form the flood features Mangala and Athabasca Valles. Their analyses assume instantaneous dike emplacement and predicts an initial, approximately infinite stress near the dike margin resulting in initially high discharge rates. By considering that dike propagation occurs over time, a more gradual permeability change with depth likely results and leads to a closer approximation to initial fluid flow rates. Terrestrial basaltic dike growth rates are estimated at between ~1 m/s and 10 m/s [*Spera*, 1980; *Spence and Turcotte,* 1985]. Moreover, *Hanna and Phillips* investigate only the

fluid flow resulting from pressurization of the groundwater aquifer as a result of diking. They do not consider changes in crustal permeability in the damage zone (except to make the assumption that water flow will not meet any resistance there), nor the changes in permeability resulting from dike induced compressive stresses away from the dike margin.

Our models of dike emplacement consider the gradual stress changes over the propagation period and relate these to permeability change for two planetary environments, a terrestrial mid-ocean ridge system and a dike-driven system on Mars. The Methodology section below describes: the application of a finite element program, FRANC2d, to emplace a dike and determine the surrounding stress field (Section 4.2.1); how changes in crustal stresses relate to changes in permeabilities (Section 4.2.2); description of damage zone permeability change caused by a dike intrusion following work by *Germanovich et al.* [2000] (Section 4.2.3); and how the permeability changes are implemented into boundary layer calculations for water and heat flux calculations in the adjacent hydrothermal system (Section 4.2.4). Section 4.3, Terrestrial Ocean-Ridge System, describes the investigation of a magmatic lens emplaced below the seafloor, subsequent dike propagation, and resulting crustal permeabilities, water and heat fluxes. The heat output results are compared with data recorded for event plume (megaplume) heat outputs of 10^{14} to 10^{17} J that occur in a matter of days [*Baker et al.* 1987; 1989; 1995; *Baker*, 1998]. A similar study for a Martian dike-driven hydrothermal system is then described in Section 4.4. Water flow rates and discharge volumes are compared to values estimated for the formation of Athabasca Valles. We also compare our models with the previous dike emplacement study by *Hanna and Phillips* [2006]. We end with discussion and conclusions on the effects of dike emplacement on permeability and water flow for both terrestrial and Martian dike-driven hydrothermal systems.

4.2 Methodology

4.2.1 *Dike emplacement and stress field calculation*

The 2-D finite element program FRANC2D (FRacture ANalysis Code) was employed to propagate a dike from a subsurface magma body through the crust. FRANC2d calculates displacements and stresses expected within a body of certain geometry under imposed loads and specified boundary conditions and material properties [*Wawrzynek and Ingraffea*, 1987]. FRANC2d can then determine the direction of propagation for a fracture using the calculated stress results. In fracture mechanics, cracks are known to propagate perpendicular to the direction of greatest principal tensile stress (or least principal compressive stress) [e.g. *Anderson*, 2005; *Gudmundsson*, 2011]. Our investigations here propagate a dike from a magmatic lens pressurized 1% over the lithostatic load. The dike is pressurized hydrostatically during propagation. The pressure inside the crack varies with depth as:

$$P_d = P_1 - \rho_m g h \tag{1}$$

where P_d is the dike pressure, P_1 is the pressure at the base of the dike = 1.01 * σ_L, ρ_m is the density of magma, and h is the distance above the lens. Tables 4.1a and 4.1b list the values for the Roman and Greek variables, respectively. Once the dike is emplaced, we query the resulting stresses surrounding the dike to calculate changes in permeability.

4.2.2 *Calculations of crustal permeability change*

Changes in crustal permeability in the region adjacent to the dike were determined by calculating the effect of the stress change induced by dike emplacement on the in-situ cracks present there. Here we present the derivation of the relationship between initial permeability and the change under an applied stress/outside force as described by *Germanovich* [personal comm., 2013]. Figure 4.2a shows the geometry assumed for an initial set of vertical, parallel cracks in the crust. The permeability for this region of cracks is calculated as:

$$K_z = \frac{w^3}{12S} \tag{2}$$

where K_z, is the permeability through the cracks, w is the crack width, and S is the average spacing between cracks. Applying Darcy's law that considers viscous flow through a porous medium, we can express fluid flow rate through the cracks, $q(z)$, as:

$$q(z) = -\frac{K_z}{\mu}\frac{\partial P}{\partial z} \tag{3}$$

where μ is the fluid viscosity and P is the driving pressure. The flow rate normal to the set of cracks is defined as:

$$q(x) = -\frac{1}{2\mu}x(x-w)\frac{\partial P}{\partial z} \tag{4}$$

The effective fluid flow rate, $\langle q \rangle$, across cracks can be expressed as:

$$\langle q \rangle = \frac{1}{S} \int_S q dS = -\frac{K_*}{\mu} \frac{\partial P}{\partial z} \tag{5}$$

where K_* is the effective permeability. Following equation (2) we can express K_* as:

$$K_* = \frac{w^3}{12S} \tag{6}$$

Then, combining equations (5) and (6):

$$\langle q \rangle = -\frac{w^3}{12S\mu} \frac{\partial P}{\partial z} \tag{7}$$

which can be rewritten as $\langle q \rangle = \frac{w}{S} \bar{q}$ and average flow rate, $\bar{q}$:

$$\bar{q} = -\frac{w^2}{12\mu} \frac{\partial P}{\partial z} \tag{8}$$

Now, looking at a larger area where a group of sparsely located (non-intersecting) cracks occur (as shown in Figure 4.2b), $\langle q \rangle$ can be expressed as the integral of q over the volume, V, or in this 2D case, the area A:

$$\langle q \rangle = \frac{1}{V}\int_V q dV = \frac{1}{A}\int_A q dA \tag{9}$$

where, for each individual crack with an area, A_1, and flow rate, q_1, for a number of cracks, n, in the area, A:

$$\langle q \rangle = \frac{1}{A} n \int_{A_1} q_1 dA_1 \tag{10}$$

The number of cracks per unit area is defined as $N = n/A$. Then we can solve for $\langle q \rangle$ as:

$$\langle q \rangle = N\int_{-a}^{a} dy \int_{-w/2}^{w/2} q(y,z) dz = N\int_{-a}^{a} dy w(y)\overline{q}(y) \tag{11}$$

where a is the half-length of the crack centered at the origin (0,0) (see Figure 4.2b). Combining equation (11) with equation (8) gives:

$$\langle q \rangle = -N\int_{-a}^{a} dy \frac{w^3(y)}{12\mu}\frac{\partial P}{\partial x} dy \tag{12}$$

Then for $w(y) = w_{\max}\sqrt{1 - y^2/a^2}$, where w_{max} is the maximum crack width,

$$\langle q \rangle = \frac{-N}{12\mu}\frac{\partial P}{\partial x} w_{\max}^3 \int_{-a}^{a} \left(1 - \frac{y^2}{a^2}\right)^{3/2} dy$$

$$\frac{-N}{12\mu}\frac{\partial P}{\partial x}w_{\max}^3 a\int_{-a}^{a}\left(1-\frac{y^2}{a^2}\right)^{3/2}d\frac{y}{a}$$

$$\frac{-N}{12\mu}\frac{\partial P}{\partial x}w_{\max}^3 a\int_{-1}^{1}\left(1-u^2\right)^{3/2}du \tag{13}$$

If we let $I=\int_{-1}^{1}\left(1-u^2\right)^{3/2}du$, then equation (13) is expressed:

$$\langle q\rangle=-\frac{Naw_{\max}^3}{12\mu}\frac{\partial P}{\partial x}I \tag{14}$$

Following equations (6), (7) and combining with (14) we can write an expression for the new permeability, K_*, as:

$$K_*=-\frac{Naw_{\max}^3}{12}I \tag{15}$$

For an initial crack that is pulled apart by outside forces, the width, w, and length, l, scale with the acting force, P, and Young's modulus, E, of the matrix the crack resides in as:

$$\frac{w}{l}=C\frac{P}{E} \tag{16}$$

where C is a constant defined as $C\approx 2\ (1-\nu^2)$, and ν is Poisson's ratio. The ratio w/l is the crack aspect ratio, β. For a crack with some initial opening, w_0, under opening force, P_0, $w_{max}=w_0+\Delta w$,

and $P_x=P+\Delta P$. Then

$$\Delta w = C\frac{P}{E}l \tag{17}$$

and

$$w_{\max} = w_0 + C\frac{\Delta P}{E}l \tag{18}$$

then combining equation (15) and (18):

$$K_* = \frac{NaI}{12}\left(w_0 + C\frac{\Delta P}{E}l\right)^3 \tag{19}$$

where for

$$K_0 = \frac{NaI}{12}w_0^3 \tag{20}$$

equation (19) is now expressed as:

$$K_* = K_0\left[1 + \frac{C}{\beta}\frac{\Delta P}{E}\right]^3 \tag{21}$$

which relates initial permeability, K_0, and the change in stress perpendicular to the dike, ΔP, before and after dike emplacement.

Typical terrestrial crack aspect ratios range from 10^{-2} to 10^{-5} [*Rubin*, 1995; *Germanovich pers. comm.* 2013] and we assume the cracks in the Martian crust will also fall within this range as the Martian crust has similar rock properties and stress fields to those observed at mid-ocean ridges. In this study, we investigate the sensitivity of permeability change to a range of aspect ratios and Young's Modulus, particular to each hydrothermal environment (terrestrial mid-ocean ridge or Mars). Initial permeability, K_0, of the crust for the terrestrial systems is estimated at 10^{-13} m^2, following the study by *Germanovich et al.* [2000] of a terrestrial mid-ocean ridge system and at $K_0 = 10^{-12}$ m^2 for the Martian system following the model by *Hanna and Phillips* [2006].

4.2.3 *Description of damage zone permeability change*

Dike propagation through the crust will cause disruption and fracturing of the surrounding material. Observations of an increased density of cracks close to the dike margin and their absence at a distance of more than a few dike widths such as at the Susanville ophiolite in California [*Coleman*, 1977; *Xenophontos and Bond*, 1978] led *Germanovich et al.* [2000] to suggest that the high density of cracks near the dike were formed during the new dike's intrusion into a colder dike complex. An increased permeability zone may therefore occur along the sides of a dike as the dike propagates through the crust. Based on field observations by *Germanovich et al.,* [2000] damage zone permeabilities are estimated to range from $K = 10^{-10}$ to 10^{-8} m^2 in a zone where the original permeability was $K = 10^{-13}$ m^2. We apply this change in permeability ($\Delta K = \sim 10^3$ to 10^5) to damage zone permeability change in terrestrial mid-ocean ridge and Martian settings. We also follow the observations of *Germanovich et al.* [2000] that estimate the

damage zone width is equal to about one dike width.

4.2.4 *Water flow rate and heat flux calculations*

Following dike emplacement, and assuming adjacent water saturated porous crust, heat from the dike will induce circulation and drive water to the surface. Figure 4.3 depicts the dike-driven hydrothermal system. Depending on the width of the boundary layer, we apply the permeabilities determined by Equation (21) and/or damage zone permeabilities and implement boundary layer calculations, as described below, to determine fluid and heat flow rates of the hydrothermal systems. These calculations are for a steady-state, single-phase (liquid) system and so provide an upper limit estimate for the fluid and heat flow rates. A thorough description of the boundary layer theory with application to Mars is given in *Craft and Lowell* [2012] and for a terrestrial mid-ocean ridge system in *Craft and Lowell* [2009]. The essential equations applied here include the vertical water velocity, v:

$$v = \left[\rho_\infty g \alpha_f \left(T_w - T_\infty\right) K / \mu\right] f'(\eta) \tag{22}$$

and temperature, T:

$$T = f'(\eta)\left(T_w - T_\infty\right) + T_\infty \tag{23}$$

where ρ_∞ is the density of the water at an infinite distance from the dike wall, g is the acceleration due to gravity, α_f is coefficient of thermal expansion for water, T_w is the temperature at the dike wall, T_∞ is the temperature of the water at an infinite distance from the dike wall, K is the permeability of the crust, μ is the dynamic viscosity of water, and $f'(\eta)$ is the dimensionless

function that is equal to the dimensionless temperature function, $\theta(\eta)$:

$$\theta(\eta) = \frac{T - T_\infty}{T_w - T_\infty} \tag{24}$$

where $f(\eta)$:

$$f(\eta) = \frac{\psi}{\kappa Ra^{1/2}} \tag{25}$$

where ψ is the stream function, κ is the effective thermal diffusivity = $\lambda/(\rho_\infty c_f)$, λ is the thermal conductivity of the rock-water mixture, c_f is the specific heat of the water, and η is the dimensionless parameter:

$$\eta = Ra^{1/2}\, x/y \tag{26}$$

where x and y are the horizontal and vertical distances with origins at the dike wall and base, respectively, and Ra is the Rayleigh number:

$$Ra = \frac{\rho_\infty g \alpha_f K (T_w - T_\infty) y}{\mu \kappa} \tag{27}$$

The values for $f'(\eta)$ are given in Figure 4.4. The thickness of the boundary layer, δ, can be calculated:

$$\delta = \frac{\eta_\delta y}{Ra^{1/2}} \tag{28}$$

where η_δ is the value of η at the boundary layer edge, which we assume to be when $\theta = f'(\eta) =$ 0.01, or in other words, within 1% of the edge. According to the values shown in Figure 4.4 and given in Tables 1a and 1b, $\eta_\delta = 6.6$. For boundary layer theory to be applicable to a system, the ratio of the layer thickness to dike height, δ/H must be < 0.1. As noted by Equations (27 and 28), δ varies as $K^{-1/2}$ and therefore we will verify that each dike height and permeability combination meets the $\delta/H < 0.1$ criteria for boundary layer modeling.

Heat flow, Q, can be calculated by integrating the advective heat flux across the boundary layer:

$$Q = \int_0^\delta \rho_f v T c_f dx \tag{29}$$

where ρ_f is the density of water. Water volume flow rate per unit length of the dike is calculated across the boundary layer:

$$\Phi_{Vol} = \int_0^\delta v dx \tag{30}$$

Total water flow volumes can then be calculated over the lifetime of the dike, which is estimated as the conductive lifetime:

$$\tau \sim \frac{w^2}{\kappa} \tag{31}$$

where w is the dike width. For our terrestrial model, we compare heat flux results to the terrestrial ocean ridge estimates for event plumes of ~ 10^{14} to 10^{17} J (*Baker et al.* 1987; 1989; 1995; *Baker*, 1998). Water flow rates and total water volume discharge values are calculated for Mars to compare to estimated values for formation of the flood feature, Athabasca Valles. We also calculate the expected stress change response of the crust to the dike induced stresses for comparison to the values obtained by the *Hanna and Phillips* [2006] tectonic-hydrologic model for formation of Athabasca Valles.

4.3 Terrestrial Dike Emplacement

At mid-ocean ridges, large, sudden increases in heat output of ~10^{14} - 10^{17} J, have been recorded during event plumes that last over a few days. Studies by *Lowell and Germanovich* [1995] and *Germanovich et al.* [2000] suggest that a damage zone can form during dike emplacement that increases permeability at the dike margins from an initial 10^{-13} m^2 to between 10^{-10} – 10^{-8} m^2, and that, in combination with a zone of porosity ≥ 1%, would enable a significant event plume to occur with a heat output of ~ 10^{17} J. The initial permeability was approximated through field observations of crack patterns in ophiolites [*Nehlig and Juteau,* 1988; *van Everdingen*, 1995] and hydrothermal system models [e.g. *Lowell and Germanovich*, 1995; *Wilcock and McNabb*, 1996; *Cherkaoui et al.*, 1997] to range between 10^{-13} to 10^{-8} m^2. Our study adds to the flow calculations of *Germanovich et al.* [2000] and *Lowell and Germanovich* [1995] and provides a more complete understanding of the effects of dike emplacement on the

hydrothermal system below a mid-ocean ridge by also considering stress and permeability change outside of the damage zone. Dike emplacement causes compressional stress in the crust that can decrease permeability. Our study calculates the dike-induced permeabilities and applies boundary layer theory to estimate steady-state water flow rates and heat output for comparison to event plume heat outputs.

4.3.1 *Model Set-up*

We began our study by modeling the emplacement of a terrestrial ocean ridge dike intrusion with the finite element program, FRANC2d. Figure 4.5a shows the model set-up. The investigation followed the model by *Sim* [2004] of a 1-km wide, 100-m thick magmatic lens emplaced 1 km below the seafloor and pressurized at 1% over the vertical load (lithostatic + seawater pressure). The lens was placed within a 20 km wide x 70 km deep grid representing the oceanic crust. Boundary conditions included fixing the left and right grid boundaries in the x (horizontal) direction and fixing the bottom boundary in the y (vertical) direction, while the top boundary remained free. Terrestrial gravity, $g_E = 10$ m/s^2, was applied in the negative y direction and the density of the rock, $\rho_r = 2700$ kg/m^3, the magma, $\rho_m = 2600$ kg/m^3, a Young's modulus of $E = 6.144 \times 10^{10}$ Pa and Poisson's ratio, $v_E = 0.264$, were specified. Elastic parameters were estimated from a crustal velocity structure modeled by *Vera et al.* [1990] at the East Pacific Rise (EPR). Lithostatic load, σ_L, increased downwards with depth below the surface, d, as $\rho_r g_E d$.

We then propagated a fracture from the corner of the lens (location of highest tensile principal stress, Figure 4.5b) up to the seafloor. Figure 4.6a shows our model's propagation results, which are essentially identical to the propagation result found by *Sim* (Figure 4.6b). This replication along with the success of *Ramondenc et al.* [2008]'s model using FRANC2d to match

the location of a propagated dike to the location of observed earthquake hypocenters provides additional confidence in our application of FRANC2d to simulate dike emplacement fracturing processes.

4.3.2 *Stress induced permeability change*

Horizontal stress values, σ_x, were surveyed at 100 m depth intervals both before and after dike emplacement using the FRANC2d program. Figure 4.7 shows the horizontal stress field, σ_x, around the sill before dike growth and Figure 4.8 shows the completed dike propagation's resulting σ_x stress field. The stress changes were then used with Equation (21) to determine the effects on permeability. In applying Equation (21), we considered a range of typical terrestrial crack aspect ratios from $\beta = 10^{-2}$ to 10^{-4} [*Rubin*, 1995] to test model sensitivity.

Results for permeability change, K_*/K_0, with depth are listed in Table 4.2. Values between 0 and 1 denote decreases in permeability while negative values indicate such a large decrease that resulting permeability is essentially 0. Permeability decreased approximately one order of magnitude for $\beta = 10^{-2}$ at all depths and for $\beta = 10^{-3}$ when $d = 100$ m. For $\beta = 10^{-3}$ and $d = 200$ - 700 m, permeabilities decreased from 2 to 5 orders of magnitude. For $d > 700$ m and $\beta = 10^{-3}$ and for all depths when $\beta = 10^{-4}$, permeability was essentially zero. Therefore, assuming a starting permeability of 10^{-13} m^2, dike emplacement decreased surrounding crustal permeability (outside of the damage zone) to 10^{-14} to 10^{-18} m^2 or lower.

Alternatively, if a dike stalls at some depth below the surface, tensile stresses at the crack tip will occur and cause an increase in permeability. *Germanovich et al.* [2011] suggest that a noneruptive dike emplaced beneath a MOR, could cause an increase in permeability and enable elevated fluid vent temperatures, as observed at the East Pacific Rise 9°50′N. Considering this,

we performed a simulation that limited dike propagation at ~ 225 km from the surface (Figure 4.9a) and then queried the surrounding σ_x stresses. We calculated the changes in permeability for the stress changes induced by shallow dike emplacement and calculate hydrothermal heat and water fluid flux values. Figure 4.9b shows σ_x results for the shallow dike model, and how the stress field is in tension from the crack tip to the surface (except for a small region directly over the crack that is in compression), extending laterally ~ 10 km to each side. Calculations suggest an increase in permeability of ~ 10^2 for this tensile region. Therefore, the tensional stresses above an emplaced dike also agree well with increasing permeability and enabling elevated vent temperatures to reach the seafloor, as higher permeabilities focus flow and increase heat and water flow rates (discussed in following section). Assuming a porosity of 1% for this ~20 km x 225 m x 200 km increased permeability region above the dike, a volume of ~ 9 x 10^{11} m^3 is available for high flow rates. The water within the damage zone will also flow quickly in the high permeability. For a 10 m wide dike this is 10 m x 775 m x 200 km = 3.1 x 10^9 m^3. According to *Baker et al.* [1995], observed event plume volumes ranged from ~ 1.3 to 4 x 10^{10} m^3 at the Juan de Fuca ridge. Our system would therefore provide adequate water volume for an event plume. Variations on raised permeability region volume would occur for longer/shorter dike segments and/or deeper/shallower dike tip depths.

4.3.3 *Water and heat out rates*

For the water and heat flow calculations, we first determined the width of the boundary layer assuming a hot wall temperature of 600 °C that represents the dike and assessed the permeability within the boundary layer following calculations described previously in Sections 4.2.3 and 4.2.4. Results are provided in Table 4.3. Dike widths considered follow typical crack

aspect ratios of 10^{-2} to 10^{-3}, estimating a 1 – 10 m width range for a 1 km tall dike. Since damage zones are expected to extend from the edge of a dike equal to the distance of about one dike width, the damage zone width for this shallow dike was assumed to be 1 - 10 m. Figure 4.10 shows the boundary layer thicknesses for a range of permeabilities that would occur within a damage zone and shows the 1 m dike damage zone boundary. If flow occurred within the damage zone, permeabilities between 10^{-10} to 10^{-8} m^2 applied. For flow in the boundary layer outside the damage zone, permeabilities determined by the compressive dike stresses (listed in Table 4.2) were applied. For the 1 m wide dike and $K = 10^{-10}$ m^2, part of the flow occurred outside the damage zone at permeabilities between 10^{-14} to 10^{-18} m^2 depending on depth and crack aspect ratio. The boundary layer outside of the damage zone would be much wider due to the lower permeability as δ scales as $\sim K^{-1/2}$ (see Equations (27) & (28)) but flow would occur at a much slower rate (see Table 4.3).

For the model of a dike stalled beneath the surface, the permeability above the dike would change from the assumed $K_0 = 10^{-13}$ m^2 to $K_* = 10^{-11}$ m^2. Flow rates at this permeability are ~ 5 km^3/yr or 153 m^3/s. Heat outputs for an initial crustal permeability of 10^{-13} m^2 and those for 10^{-11} m^2 are given in Table 4.4. With such a large tensile and higher permeability area outside the damage zone, the heated water from next to the dike will travel more easily and quickly to the sea floor. Also, water from the tensile region can move more easily to circulate and add volume to the system. These results for a tensile region above a stalled dike, support and expand the dike emplacement mechanism for enabling elevated vent temperatures as suggested by *Germanovich et al.* [2011] who looked only at damage zone permeability increases.

4.4 Martian Dike Emplacement

The fracture mechanics of dike growth on Mars will occur similarly to those on Earth. Diking events have been suggested as the driving mechanism for water flow to the surface for several flood features emanating from surface fissures including Athabasca Valles, Mangala Valles, Marte Valles, Grjo´ta´ Valles and Granicus Valles [*Ernst et al.*, 2001; *Mège et al.,* 2003; *Wilson and Head*, 2002; *Burr et al.*, 2002a; *Plescia*, 2003; *Mouginis-Mark* et al., 1984]. These tectonic events change stresses and temperatures in the subsurface and can induce hydrothermal flow in adjacent water saturated crust. The hydrothermal flow can reach the surface and help form morphology observed there. *Hanna and Phillips* [2006] modeled the crustal stress increase expected on Mars for an approximately instantaneous dike emplacement and calculated the expected pressurization of an adjacent subsurface aquifer. The pressurized water was suggested to then travel along the dike and faults to reach the surface and form flood features including Athabasca Valles. We expect that the near infinite stresses that occurred in the *Hanna and Phillips* [2006] model were due to the nearly instantaneous insertion of the dike. They recognize that infinite stresses would not actually occur and take flow rate values after 10^3 s. However, terrestrial dike growth rates occur between ~ 0.01 and 10 m/s [*Spera*, 1984; *Spence and Turcotte*, 1985] and would therefore require at least 30 minutes to grow from a depth of 20 km to the surface and pressure the adjacent aquifer. Therefore, we expect a dike on Mars requires > 10^3 s (~16 min) for complete emplacement and would pressurize an adjacent aquifer gradually over time. Our models of dike emplacement and resulting stress and permeability changes consider growth rate of the dike and the effects of the stress and permeability changes on water flow rates and volumes.

While the water inside a crack will act back against dike-induced forces, we assume that

pressure to be negligible compared to the higher applied stresses. Therefore, we do not consider the effects of pressurization on driving the fluid to the surface as in *Hanna and Phillips* [2006], but instead consider that the dike will heat the adjacent water and cause hydrothermal circulation through the permeable crust we evaluated. We do, though, perform a comparison of our stresses to those found by *Hanna and Phillips* [2006] in Section 4.5.3 below, to changes caused by dike emplacement.

We begin by performing a set of models that propagate a dike upwards from a deep sill. We then make measurements of the changes in the crustal stress to estimate permeability change (Equation 21) outside of the damage zone, that then allows a greater understanding of how water in the adjacent saturated crust could flow to the surface and possibly form the morphology observed there. Water flow rate and volume results are calculated as hydrothermal flow driven by the dike heat using boundary layer theory and are compared to estimates for formation of the valley system Athabasca Valles (see Section 4.5.2) and to rates driven by pore pressure increase calculated in *Hanna and Phillips* [2006] (see Section 4.5.3).

4.4.1 *Model Set-up*

In our study, we placed a 10 km wide x 1 km thick lens-shaped magmatic intrusion at 20 km below the surface and propagated a dike to the surface using the finite element program FRANC2d. Figure 4.11 shows the model set-up. The lens was placed within a 70 km x 70 km grid representing the Martian crust. Boundary conditions included fixing the left and right grid boundaries in the x (horizontal) direction and the bottom boundary in the y (vertical) direction, while the top boundary remained free. Martian gravity was applied in the negative y direction and the density of basalt (ρ_b = 3000 kg/m^3) was specified. Lithostatic load, σ_L, therefore,

increased downwards within the grid as $\rho_b g_m d$, where g_m is the gravitational acceleration on Mars = 3.71 m/s^2 and d is the depth below the surface. Two Young's modulus values, $E = 10^{10}$ and 10^{11} Pa, were implemented as well as a range of crack aspect ratios from $\beta = 10^{-2}$ to 10^{-4} to test model sensitivity to these parameters.

Dike emplacement was initialized by pressurizing the magma lens to 1% over the lithostatic load at the depth, d = 20 km. Using FRANC2d, we then assessed where the greatest tensile stress existed along the lens boundary (see Figure 4.12), initiated a crack/dike there and propagated the hydrostatically pressurized dike to the surface.

4.4.2 *Permeability change results*

To find the permeability change outside of the damage zone, stress values were obtained for each model before and after dike emplacement at 2 km depth intervals using the FRANC2d program. Figure 4.13 shows the horizontal stress, σ_x, field around the sill before dike growth for the base model with: $E = 10^{10}$ Pa and $\nu_M = 0.25$. Figures 4.14a and b show the completed dike propagation and resulting σ_x field, respectively, for the model with $E = 10^{10}$ Pa and ρ_m= 2700 kg m^{-3}. Figure 4.15 shows the σ_x field contour plot before dike growth for the model with $E = 10^{11}$ Pa. Figures 4.16a and b show the completed dike propagation and contour plot of σ_x, respectively, for the $E = 10^{11}$ Pa model. The dike reaches the surface in both of these models. Horizontal stress induced by the dike act to open (tensile stress) or close (compressive stress) vertical cracks in the crust. Positive stress values shown are tensile and negative values are compressive.

Stress results show that the compressive lithostatic stress before dike propagation increases to higher compressive levels afterwards, alongside the dike. The increase in compressive stress

will decrease permeability as indicated by Equation (21). Table 4.5 lists permeability change values with depth calculated by applying Equation (21) and the measured σ_x values. Crack aspect ratios applied for the two models of $E = 10^{10}$ and 10^{11} Pa included $\beta = 10^{-2}$, 10^{-3}, and 10^{-4}. Values between 0 and 1 indicate decreases in permeability and negative values suggest essentially no permeability remains in that region. Smaller permeability changes occur for the model with $E = 10^{11}$ Pa than for $E = 10^{10}$ Pa as expected since the higher E indicates a stiffer matrix that is more resistive to acting forces. Also, in general we see that permeability change increases with increasing depth and with decreasing crack aspect ratio.

We note that at depths greater than ~ 11 km, the porosity of the crust on Mars is expected to be extremely low (< 0.01) nominally [*Clifford*, 1993; *Binder and Lange,* 1980], and may not allow water storage. Although, as *Clifford* [1993] states, the assumption by *Binder and Lange* [1980] of 1 kbar for the closure pressure is conservative considering that laboratory experiments show fractures and pore space can remain open at pressures of ~5–10 kbar [*Gold et al.,* 1971; *Todd et al.,* 1973*; Siegfried et al.*, 1977]. Also for wet crust at great depths, the high temperatures and pressures are expected to enable open pore space to a depth ~ 1/3 greater than the estimated "dry crust" porous depth [*Hubert and Rubey*, 1959; *Byerlee and Brace*, 1968; *Brace and Kohlstedt*, 1980; *Thompson and Connolly*, 1992; *Maxwell*, 1964; *Pettijohn*, 1975]. Furthermore, the dike intrusion fracturing process will cause damage zones along the dike margins [e.g. *Germanovich et al.,* 2000] and will induce tensional stresses around the crack tip; both which will increase permeability. A porous crust is therefore assumed plausible to the depth of 20 km as modeled in *Hanna and Phillips* [2006] however, from depths of 15 to 20 km, our model only considers porosity of significance to occur within the dike's damage zone (approximately equal to the horizontal distance of about one dike's width as indicated in

observations by *Germanovich et al.*, 2000), which will restrict the volume of water available for discharge.

According to the permeability changes calculated, there is only a positive permeability change for the $E = 10^{11}$ Pa model with $\beta = 0.01$ at all depths and for $\beta = 0.001$ at depths ≤ 4 km. For the $E = 10^{10}$ Pa model the only positive permeability change occurs for $\beta = 0.01$ at depths ≤ 2 km. The permeability changes are all decreases in permeability by ~ 2 to 5 magnitudes. Therefore, these changes indicate significant compressive stress results from dike insertion.

Tensile stresses do occur at the dike crack tip during propagation, and would therefore increase permeability there. With this in mind, we stall a dike at ~ 2 km below the surface and reassess the two models' stress fields (for $E = 10^{10}$ or 10^{11} Pa). This set up also allows comparison with results from the minimum fissure width model in *Hanna and Phillips* [2006], which extends a dike to a few kilometers below the surface. Figure 4.17 shows stress results for the stalled dike model with $E = 10^{10}$ Pa, and how the σ_x field is in tension from the crack tip to the surface, extending laterally ~12 km to the left and ~14 km to the right. Calculations show an increase in permeability by 27 times. For the $E = 10^{11}$ model the tensile stress field near the surface is about the same and also increases permeability ~ an order of magnitude. The area in tension is therefore ~ 26 km x 2 km deep x ~ 200 km long providing an available water volume ≈ 10^{13} m^3. As discussed further in Section 4.5.2 below, this region provides more than adequate volume for floods to form the valley system Athabasca Valles.

4.4.3 *Water flow rates and volume discharge*

For the nominal models of dike emplacement where the dike reaches the surface, only the $E = 10^{11}$ Pa model with $\beta = 10^{-2}$ and $\beta = 10^{-3}$ at ≤ 4 km and the $E = 10^{11}$ Pa model with $\beta = 10^{-2}$ at

≤ 2 km model shows remaining permeability next to the dike. Assuming an initial permeability for the crust of 10^{-12} m^2, as applied by *Hanna and Phillips* [2006], and applying the stress changes determined in the previous section, permeability reduces to $K_* = 10^{-14}$ m^2 after dike emplacement. Adjacent to the dike, estimated at ~ the width of the dike, there will be a raised permeability within the damage zone caused by dike emplacement disruption. The permeability could increase by three to five orders of magnitude as suggested by models of hydrothermal flow at a mid-ocean ridge during an event plume [*Germanovich et al.,* 2000]. If we use this same increase in the margins of the dike on Mars we arrive at permeabilities between 10^{-9} to 10^{-7} m^2 within the damage zone. Assuming also that the porosity is only significant above 15 km depth we perform boundary layer calculations for a 15 km tall dike. Then, according to dike width to height aspect ratios of 10^{-2} to 10^{-3}, dike half-widths range from, on the order of: 10 to 100 m. For $K = 10^{-8}$ m^2, the boundary layer thickness reaches a maximum of ~1.5 m and water flow would remain within the damage zone of 10 to 100 m for the entire dike height. For the same parameters, but with $K = 10^{-9}$ m^2, δ at the surface reaches ~ 5 m. Again, for this lower permeability and a 10 - 100 m half-width dike, the boundary layer remains within the damage zone for the whole dike height. The same will occur for the higher permeability of $K = 10^{-7}$ m^2. Heat flow and water flow rate results across δ for a hot wall temperature of 600 °C that represents the dike, and with permeabilities of $K = 10^{-9}$ to 10^{-7} m^2 are given in Table 4.6. For the model of a dike stalled ~ 2 km beneath the surface, the permeability above the dike would change from the assumed $K_0 = 10^{-12}$ m^2 to $K_* = 10^{-11}$ m^2. This would enable the previously calculated volume (Section 4.4.2) of 10^{13} m^3 to flow more readily to the surface.

4.5 Discussion

4.5.1 *Megaplume implications for terrestrial ocean ridge model*

Previous studies by *Germanovich et al.* [2000] and *Germanovich et al.* [2011] suggest that increases in permeability along dike margins would cause elevated fluid temperatures similar to those observed during event plumes at the East Pacific Rise 9° 50′N. Our model accounts for this damage zone increase in permeability and adds the consideration of permeability change caused by stresses induced by dike emplacement. We assess the expected values for permeabilities inside the boundary layer and calculate heat and fluid outputs. For a narrow dike of ~ 1 m wide, the damage zone is also then only ~ 1 m and permeabilities outside this region are decreased from dike emplacement stress. The decrease in permeability outside the damage zone could act to focus flow and enable high flow rates close to the ridge axis. However, the decrease in permeability outside the damage zone may act to restrict the volume of water available for supplying the water flux to the seafloor. Once the water has been removed from the damage zone region, additional water further from the dike would flow into the damage zone through the lowered permeability crust and may therefore cause a decrease in overall flow rates to the seafloor. This indicates a limited high flow rate until the damage zone is emptied and then a slower rate after. The decrease in flow rate does follow the observations of high heat flux over several days followed by a large decrease as described e.g. by *Baker et al.* [1995]. *Germanovich et al.* [2000] suggest that the rapid decrease of heat output after a plume event requires the closing of cracks in the damage zone through stresses or chemical precipitation. However, our study indicates that the lower permeability outside the damage zone may be a cause for the lowering of the heat output and fluid flow once the damage zone water is released.

Also, *Lowell and Germanovich* [1995] describe how the recharge zone must have a permeability of $K \sim 10^{-14}$ to 10^{-12} m^2 for cross sectional areas of 10^6 and 10^4 m^2, respectively, to enable the fluid flow required for an event plume. Our permeabilities after dike emplacement ($\sim 10^{-15}$ to 10^{-18} m^2) would then require a recharge area of $\geq 10^7$ m^2. This size may not be feasible for an ocean ridge setting.

The initial elevated heat outputs resulting for an increased permeability within the damage zone of between $K = 10^{-10}$ to 10^{-8} m^2 (Table 4.3) appear to occur at levels comparable to the heat out for event plumes. For $K=10^{-10}$ m^2 the heat out for a 1 km tall dike is 2.9×10^6 J/m/s. Then, for a 20 km long dike that releases heat over a day, a heat out of $\sim 5 \times 10^{15}$ to 5×10^{16} J would occur for permeabilities of $K=10^{-10}$ to 10^{-8} m^2. This falls within the observed range of heat outputs for event plumes.

4.5.2 *Mars dike model comparison to Athabasca Valles formation*

The source fissure for Athabasca Valles occurs in the Cerebus Fossae group. Morphological surveys estimate the feature to be about 1000 m wide and 200 km long, although the width was likely widened by erosion and mass wasting over time, with an initial fissure width of 200 to 500 m suggested by *Hanna and Phillips* [2006]. Estimates of the fluid flow volume based on MOLA (Mars Orbiter Laser Altimeter) topography to form Athabasca fall between 400 km^3 to 1600 km^3 [*Hanna and Phillips*, 2006]. Upper limit flow rate estimates based on the geomorphology of Athabasca Valles range from about 300 to 3×10^5 km^3/yr [*Burr et al.*, 2002a, 2002b, 2004; *Mitchell et al.*, 2005].

Flow rates calculated for a 200 km long dike propagated from 20 km depth to the surface are given in Table 4.6. The dike length was chosen to simulate the fissure length observed at the

source fissure for Athabasca Valles. Rates for permeabilities of $K = 10^{-8}$ and 10^{-7} m^2 fall above 300 km^3/yr and could therefore provide flow to form the valley system. Total volumes are estimated over the conductive lifetime (Equation (31)) of the dike-driven system. A 10 m half-width dike will conduct heat over ~ 3 years and a 100 m half-width dike has a lifetime of about 300 years. Over this time the dike will drive water to the surface from both sides. Total volume amounts for each permeability and dike lifetime/width are shown in Table 4.7. All systems tested meet the minimum volume estimated requirement of 400 km^3 and systems with the wider dike and $K \geq 10^{-9}$ m^2 as well as the narrower dike with $K \geq 10^{-8}$ m^2 meet or exceed the upper 1600 km^3 requirement. A similar model by *Craft and Lowell* [2012] also calculated water flow rates for a dike driven hydrothermal system on Mars, except their analysis did not consider the higher permeabilities in the damage zone which enables quicker flow rates.

One consideration for this model is that the calculations assume the water drawn into the system flows through a similar or higher permeability. In actuality, as shown through the FRANC2d modeling, the permeability outside of the damage zone will be less than or equal to the initial permeability of $K=10^{-12}$ m^2 and may equal zero. The lower permeability could restrict flow into the hydrothermal boundary layer and increase the time required to reach the discharge volume needed, though the flow rate should not be affected. The volume of water available in the higher permeability damage zone can be estimated considering the width of the damage zone ~ the width of the dike. For a Martian dike ~ 15 km deep (where porosity is significant), ~ 200 km long, and with a damage zone ~ 10 – 100 m wide, a volume of 30 to 300 km^3 is available respectively. Therefore, to form Athabasca Valles, flow from outside the damage zone region is required. Since observations indicate that Athabasca Valles likely formed from multiple flood events, the damage zone could have had time to recharge between flood events and still enable

the formation of the valley system.

4.5.3 *Comparison of Mars dike model to Hanna and Phillips [2006] model*

Hanna and Phillips [2006] consider tectonic pressurization resulting from the emplacement of a dike into the crust on Mars. First they calculate dike emplacement stresses and the resulting pore pressures that would occur in an adjacent water saturated aquifer. Results suggest that for a dike of minimum fissure width (dike stalls a shallow depth of a few kilometers) the discharge rates are comparable to those required to form the flood valley feature, Athabasca Valles. Also, total volume output over the tectonic history of the fissure meets and exceeds the range of volume needed (400 to 1600 km^3 [*Hanna and Phillips*, 2006]).

To compare the dike-induced stresses from our model to those found by *Hanna and Phillips* [2006] we apply the stresses calculated in the region adjacent to the dike to the pore pressure equation in *Hanna and Phillips* [2006]:

$$\Delta\sigma_{pore} = B \cdot \frac{\Delta\sigma_x + \Delta\sigma_y + \Delta\sigma_z}{3} \tag{32}$$

where $\Delta\sigma_{pore}$ is the change in pore fluid pressure, $\Delta\sigma_i$ are the normal stress changes in the crust in the three principle directions, and B is the aquifer pressurization coefficient following *Rice and Cleary* [1976] expressed as:

$$B = \frac{\beta_d - \beta_r}{\beta_d - \beta_r + \phi \cdot (\beta_w - \beta_r)} \tag{33}$$

where β_d is the compressibility of the drained aquifer, β_r is the compressibility of the pore-free rock mass, ϕ is the porosity, and β_w is the water compressibility. *Hanna and Phillips* [2006] use $B = .773$ for the nominal model. We apply this value along with $\Delta\sigma_x$ and $\Delta\sigma_y$ for our 2D model and compare stress values. Table 4.8 lists the pore pressure stresses calculated along 2 km intervals with depth. The average pore stresses calculated by our model gives compressive stress values ranging from ~ 50 to 67 MPa. The stresses calculated by *Hanna and Phillips* [2006] are about the same at around 60 MPa ranging to slightly lower at about 20 MPa. The locations of compressive and tensile stresses also match well between the models with tensile stresses at the dike tips and compressive stresses surrounding the dike.

These tectonic pressures could indeed drive fluid flow through the crust, however, flow from outside of the damage zone would occur at a reduced rate due to the decrease in permeability from the dike emplacement. Therefore, the initial damage zone volume of water, approximated at 30 to 300 km^3 (section 4.5.2) could flow at rates suggested by *Hanna and Phillips* [2006], but additional water would flow at lower rates.

4.6 Conclusions

The model presented here provides a more complete picture of the effects of dike emplacement on stress and permeability change as a process for driving water and heat to the surface in terrestrial and Martian environments. The finite element model allows the gradual propagation of the dike into the crust and calculation of induced permeabilities. Previous studies applied permeability change within a dike damage zone to assess fluid and heat outputs at mid-ocean ridges [*Germanovich et al.,* 2000; *Lowell and Germanovich*, 1995; *Germanovich et al.,* 2011] and beneath dike induced fissures on Mars [*Hanna and Phillips*, 2006]. By considering

both damage zone increased permeability and dike induced decreases in permeability outside of the damage zone, our models determine where boundary layer will flow and assess if flow can occur at adequate rates and with sufficient volumes to produce the event plumes at terrestrial mid-ocean ridges and flooding events on Mars. Results determine that heat out for a 200 km long dike releasing heat over a day provides ~ 5 x 10^{16} J which falls within the expected event plume range of 10^{14} – 10^{16} J. Our models also find that flow next to a dike on Mars would occur mainly through the damage zone at adequate flow rates for formation of Athabasca Valles. Total volume required, however, requires recharging to occur between flood events. Comparison of stresses from dike emplacement with those calculated by Hanna and Phillips finds fairly good agreement.

Table 4.1 Symbols **a.** Roman Characters:

Symbol	Definition	Value	Units
A	Area containing cracks	varies	m^2
A_1	Individual crack area	varies	m^2
a	Half-length of crack	varies	m
B	Aquifer pressurization coefficient	0.773	unitless
C	Constant $\approx 2(1-\nu^2)$	varies	unitless
c_f	Specific heat of the water	4.18	$kJ(kg°C)^{-1}$
d	Depth below surface	varies	m
E	Young's modulus	10^{10} to 10^{11}	Pa
f	Similarity variable for velocities	Equation (25)	unitless
g	acceleration of gravity	varies	$m\ s^{-2}$
g_E	acceleration of gravity on Earth	10	$m\ s^{-2}$
g_m	acceleration of gravity on Mars	3.71	$m\ s^{-2}$
H	Dike height	1 or 15	km
h	Distance above lens	varies	m
I	Integral of $(1-u^2)^{3/2}$ over crack length	varies	unitless
K_0	Initial permeability	10^{-12} or 10^{-13}	m^2
K_z	Permeability in z direction	Equation (2)	m^2
K_*	Permeability after dike emplacment	Equation (21)	m^2
ΔK	Change in permeability	varies	m^2
l	Crack length	varies	m
N	number of cracks per unit area	varies	m^{-2}
n	number of cracks	varies	unitless
P	Pressure	varies	Pa
P_d	Dike pressure	varies	Pa
P_0	Crack opening force	Equation (1)	Pa
P_1	Pressure at base of dike	varies	Pa
ΔP	Change in opening force	$1.01*\sigma_L$	Pa
Q	Heat flux across boundary layer	Equation (29)	J/km/yr
$\langle q \rangle$	Effective water flow rate	Equation (14)	$m\ s^{-1}$
$\bar{q}$	Average water flow rate	Equation (8)	$m\ s^{-1}$
$q(x)$	Water flow rate normal to cracks	Equation (4)	$m\ s^{-1}$
$q(z)$	Water flow rate through cracks	Equation (3)	$m\ s^{-1}$
Ra	Rayleigh number	Equation (27)	unitless
S	Average spacing between cracks	varies	m
T	Temperature	varies	°C
T_W	Temperature of heated wall	600	°C
T_∞	Temperature at infinite distance from heated wall	4	°C
u	Represents y/a dimension	varies	unitless
V	volume containg fractures	varies	m^3
v	Vertical water velocity	Equation (22)	m/s
w	Dike/crack width	varies	m
w_0	Crack initial opening	varies	m
w_{max}	Maximum crack width	varies	m
Δw	Change in crack width	varies	m
x	horizontal direction/position	varies	unitless/m
y	vertical direction/position	varies	unitless/m
z	direction into page	varies	unitless

b. Greek variables

Symbol	Definition	Value	Units
a_f	Thermal expansion coefficient of water for high temperature conditions	10^{-3}	$°C^{-1}$
b	Crack aspect ratio	10^{-4} to 10^{-2}	unitless
δ	Boundary layer thickness	Equation (28)	m
η	Similarity variable for position	Equation (26)	unitless
η_δ	Position value at edge of boundary layer	6.6	unitless
θ	Similarity variable for temperature	Equation (24)	unitless
κ	Effective thermal diffusivity	$\lambda/(\rho_\infty c_f)$	$m^2\ s^{-1}$
λ	Thermal conductivity of rock-fluid mixture	2.6	$J(sm°C)^{-1}$
μ	Dynamic viscosity of water	10^{-4}	$kg\ (m\ s)^{-1}$
v	Poisson's ratio	varies	unitless
v_E	Poisson's ratio for crust below mid-ocean ridge	0.264	unitless
v_M	Poisson's ratio for crust on Mars	0.25	unitless
ρ_b	Density of basalt	3000	$kg\ m^{-3}$
ρ_f	Density of the water	Equation (5)	$kg\ m^{-3}$
ρ_m	Density of magma	2600	$kg\ m^{-3}$
ρ_r	Density of rock	2700	$kg\ m^{-3}$
ρ_∞	Density of the fluid at infinite distance from dike wal	1000	$kg\ m^{-3}$
σ_L	Lithostatic load	varies	Pa
$\Delta\sigma_{pore}$	Change in pore fluid pressure	Equation (32)	Pa
σ_x	Horizontal stress	varies	Pa
$\Delta\sigma_y$	Change in vertical stress	varies	Pa
τ	Conductive time scale	Equation (31)	yr
Φ_{Vol}	Volume flow rate per unit dike length	Equation (30)	$m^3(m\ yr)^{-1}$
Ψ	Stream function	varies	unitless
ϕ	Porosity	varies	unitless

Table 4.2 Permeability change, (K_*/K_0), outside of damage zone (see Equation (21)) and resulting permeability, K_* given an initial permeability of $K_0 = 10^{-13}$ m^2, for terrestrial dike emplacement beneath a mid-ocean ridge for a range of crack aspect ratios, $\beta = 10^{-2}$ to 10^{-4}.

	β=0.01		**β=0.001**		**β=0.0001**	
Depth (m)	**K_*/K_0**	**K_*** for $K_0=10^{-13}$ m^2	**K_*/K_0**	**K_*** for $K_0=10^{-13}$ m^2	**K_*/K_0**	**K_*** for $K_0=10^{-13}$ m^2
100	0.86	8.6E-14	1.27E-01	1.3E-14	-62.92	NA
200	0.81	8.1E-14	3.40E-02	3.4E-15	-191.16	NA
300	0.80	8.0E-14	1.90E-02	1.9E-15	-254.04	NA
400	0.78	7.8E-14	1.04E-02	1.0E-15	-316.96	NA
500	0.77	7.7E-14	3.75E-03	3.7E-16	-412.99	NA
600	0.75	7.5E-14	1.05E-03	1.0E-16	-509.10	NA
700	0.74	7.4E-14	5.43E-05	5.4E-18	-640.78	NA
800	0.72	7.2E-14	-1.71E-05	NA	-793.40	NA
900	0.69	6.9E-14	-3.69E-03	NA	-1172.73	NA

Table 4.3 Heat out and water flow rates over a range of damage zone permeabilities for a hydrothermal system driven by a 1 km deep, 1 – 10 m wide dike. Flow remained within damage zone for the 10 m wide dike. Some flow occurred outside the damage zone for $K = 10^{-10}$ m^2 for the 1 m wide dike. The lower permeabilities outside of the damage zone greatly decreased flow rates as shown by the bounding range of permeabilities from $K = 10^{-14}$ to 10^{-18} m^2.

	Damage zone permeabilities (m^2)			Outside DZ - bounding permeabilities (m^2)	
	K=1e-10	1E-09	1E-08	1E-14	1E-18
Heat flux (J/m/s)	2.92E+06	9.22E+06	2.92E+07	29.169	0.292
Mass flow rate (kg/m/s)	2.41	7.63	24.14	0.0241	2.414E-04
Vol flow rate for 200 km long dike (km^3/yr)	15.23	48.15	152.26	0.15	1.52E-03

Table 4.4 Heat and water flow rates for a stalled dike 225 m below the seafloor, at a mid-ocean ridge.

	Before dike	After
	K=10^{-13}	K=10^{-11}
Heat flux (J/m/s)	92.24	922.39
Mass flow rate (kg/m/s)	0.076	0.763
Vol flow rate for 200 km long dike (km^3/yr)	0.48	4.81

Table 4.5 Permeability change (K_*/K_0) (see Equation (21)) and resulting permeability, K_* given an initial permeability $K_0 = 10^{-12}$, for Martian dike emplacement, outside of damage zone

$E=10^{10}$ Pa			
Depth (m)	β=0.01	β=0.001	β=0.0001
2000	3.52E-03	-4.18E+02	-5.88E+05
4000	-4.11E-04	-9.25E+02	-1.21E+06
6000	-2.79E-02	-1.74E+03	-2.16E+06
8000	-1.49E-01	-2.92E+03	-3.51E+06
10000	-4.57E-01	-4.66E+03	-5.45E+06
12000	-1.05E+00	-7.03E+03	-8.07E+06
14000	-2.01E+00	-1.01E+04	-1.14E+07
16000	-3.59E+00	-1.44E+04	-1.60E+07
18000	-5.77E+00	-1.95E+04	-2.16E+07
$E=10^{11}$ Pa			
Depth (m)	β=0.01	β=0.001	β=0.0001
4000	0.74	1.94E-05	-6.66E+02
6000	0.68	-0.01	-1.39E+03
8000	0.62	-0.11	-2.58E+03
10000	0.57	-0.38	-4.28E+03
12000	0.52	-0.88	-6.42E+03
14000	0.47	-1.93	-9.86E+03
16000	0.42	-3.37	-1.38E+04
18000	0.37	-5.95	-2.00E+04

Table 4.6 Heat flow and water flow rate results across δ for a hot wall temperature of 600 °C that represents the dike, and with permeabilities of $K = 10^{-9}$ to 10^{-7} m^2

	K=1E-09 m^2	1E-08	1E-07
Heat flux (KJ/m/s)	2.176E+04	6.881E+04	2.176E+05
Mass flow rate (kg/m/s)	18.01	56.95	180.09
Vol flow rate for 200 km long dike (km^3/yr)	113.59	359.20	1135.84

Table 4.7 Volume output over dike lifetime for range of elevated permeabilities on Mars

dike half width (m)	lifetime (yrs)	K=10^{-9}m^2	K=10^{-8}m^2	K=10^{-7}m^2
10	3	682	2155	6815
100	300	68152	215517	681503

Table 4.8 Average pore pressures calculated from change in stress field after dike emplacement along 2 km intervals with depth on Mars

depth	$\Delta\sigma_x$	$\Delta\sigma_y$	$\Delta\sigma_{pore}$
2000	-4.52E+07	-1.28E+08	-6.68E+07
4000	-5.73E+07	-7.85E+07	-5.25E+07
6000	-6.95E+07	-5.92E+07	-4.97E+07
8000	-8.16E+07	-4.88E+07	-5.04E+07
10000	-9.44E+07	-3.90E+07	-5.16E+07
12000	-1.08E+08	-3.00E+07	-5.31E+07
14000	-1.21E+08	-1.90E+07	-5.40E+07
16000	-1.35E+08	-1.15E+07	-5.66E+07
18000	-1.49E+08	-1.00E+07	-6.15E+07

Figures:

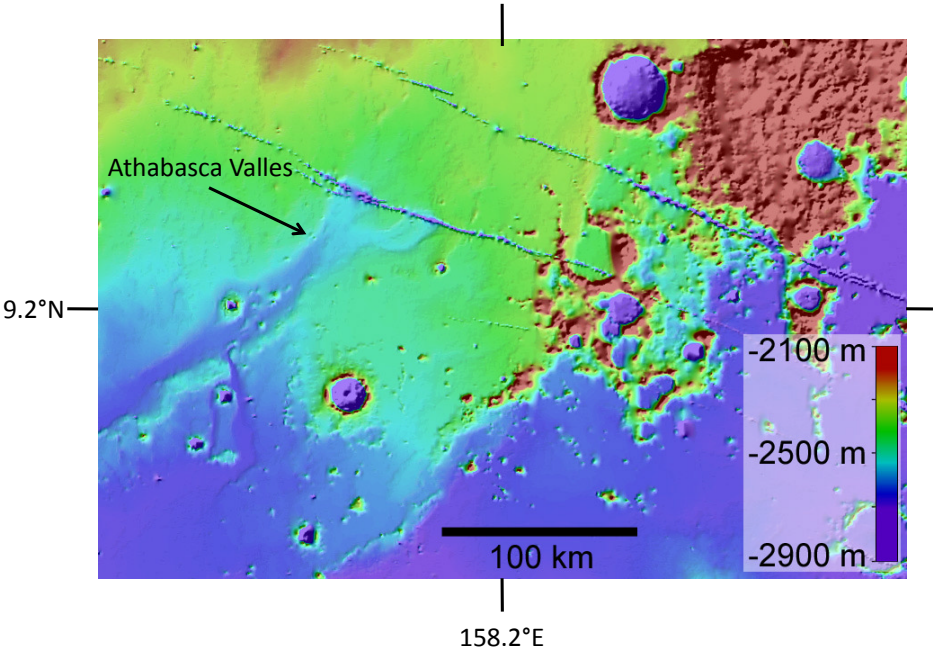

Figure 4.1 MOLA topographic image showing flood feature Athabasca Valles emanating from lower fissure of Cerebus Foassae at SE edge of the Elysium rise region.

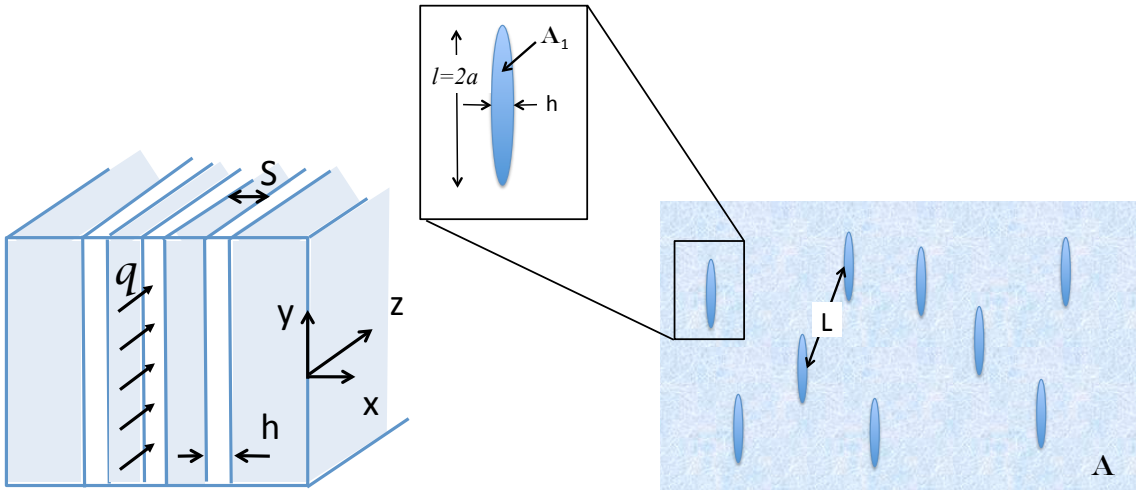

Figure 4.2 a. Fractured crust with flow perpendicular to cracks, q, crack width, h, and crack spacing, S. **b.** Showing sparsely situated vertical cracks as modeled for estimating permeability K_z (Equation 1) in area, A, with spacing, L, individual crack area, A_1, and length, $l = 2a$

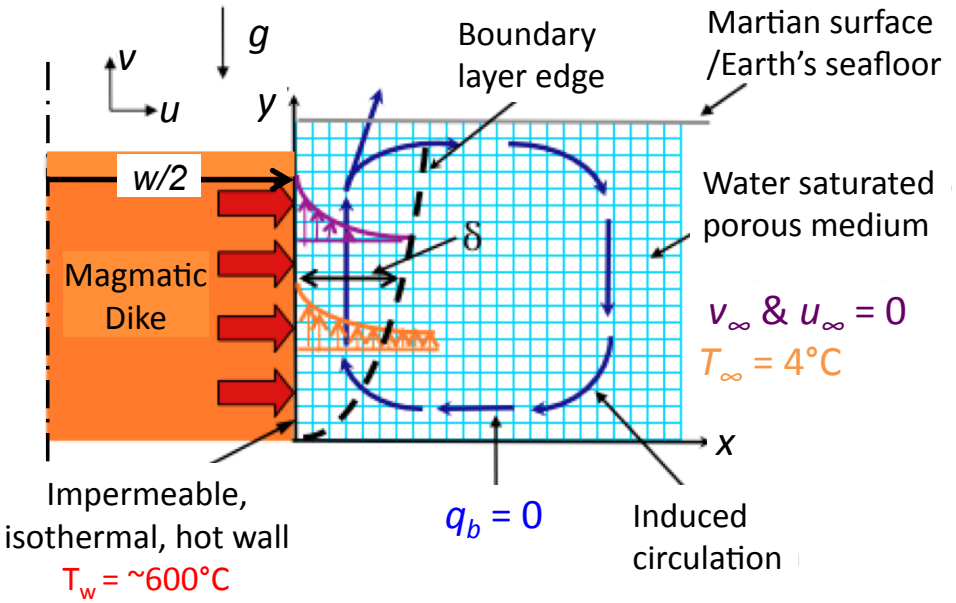

Figure 4.3 Model of emplaced dike heating the adjacent, water-saturated porous crust. Induced water circulation shown by blue arrows. Temperature, *T*, and velocity, *u* & *v*, profiles (orange and purple, respectively) within the boundary layer, *δ,* are depicted [*Craft and Lowell*, 2012].

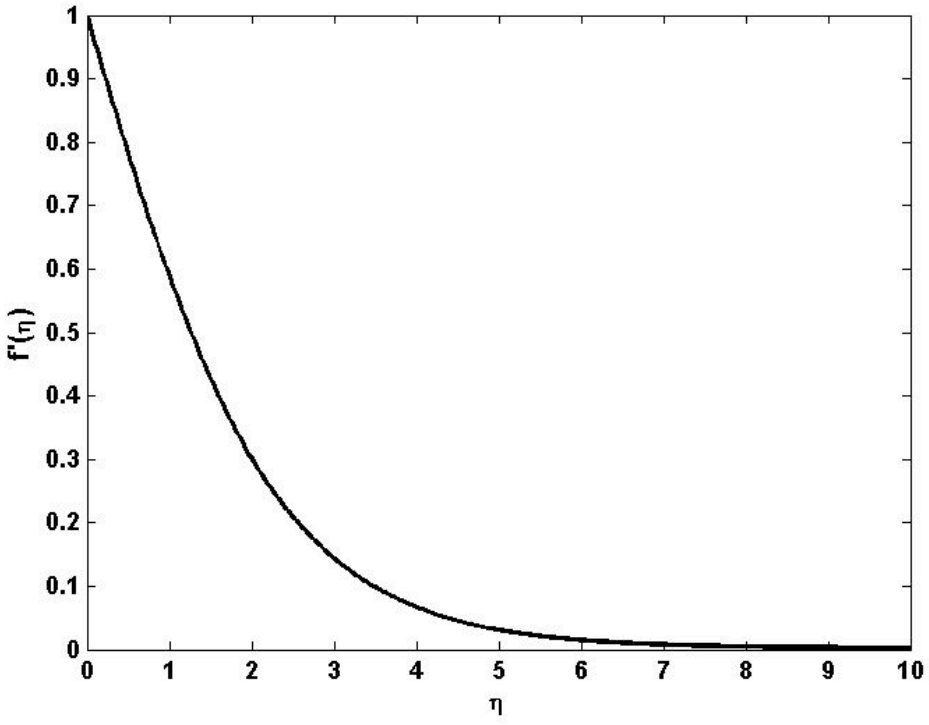

Figure 4.4 Similarity solution for *f '(η)* as a function of *η*. The solution indicates the shape of the temperature and vertical velocity profiles within the boundary layer, where distance from the dike wall increases as *η* increases [*Craft and Lowell*, 2012].

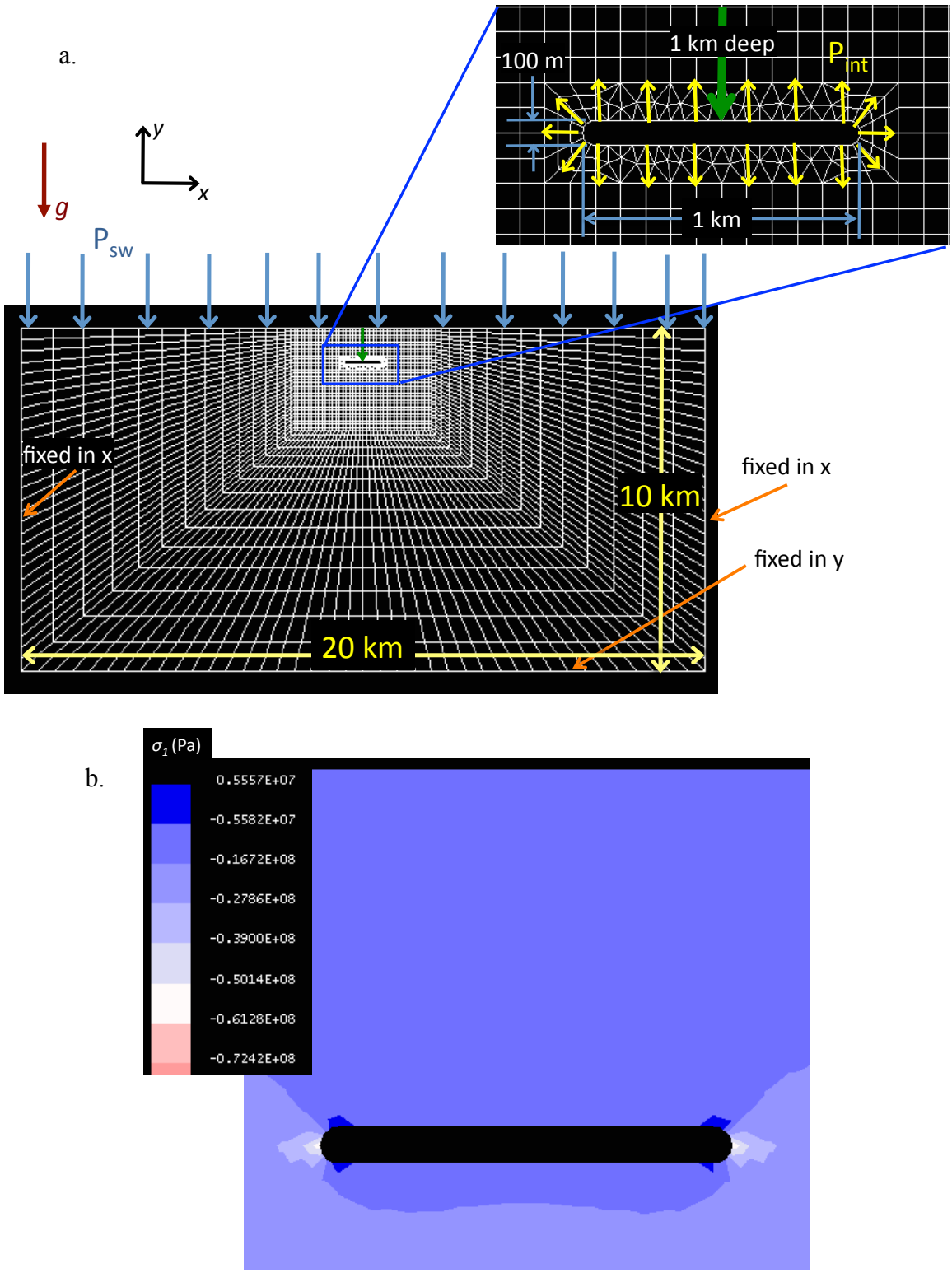

Figure 4.5 a. Terrestrial model set-up **b.** Principle stress, σ_1, contours showing location of greatest tensile principle stresses at corners of magmatic lens.

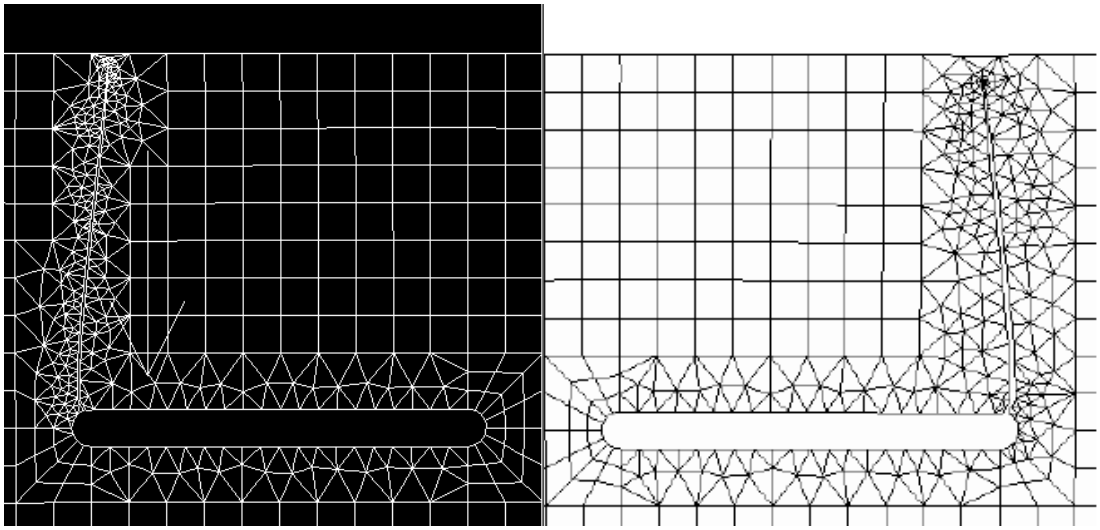

Figure 4.6 Showing comparison of mid-ocean ridge terrestrial dike propagation by: **a.** this study **b.** *Sim* [2004]

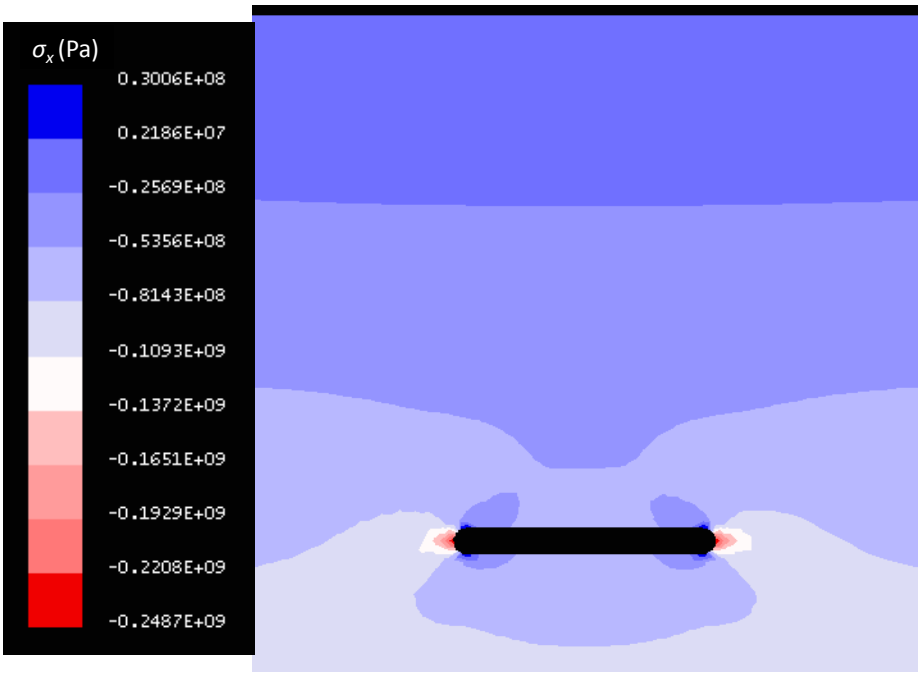

Figure 4.7 Stress field of horizontal stresses, σ_x, around pressurized magmatic lens before dike propagation for the terrestrial MOR model where $E = 6.144 \times 10^{10}$ Pa.

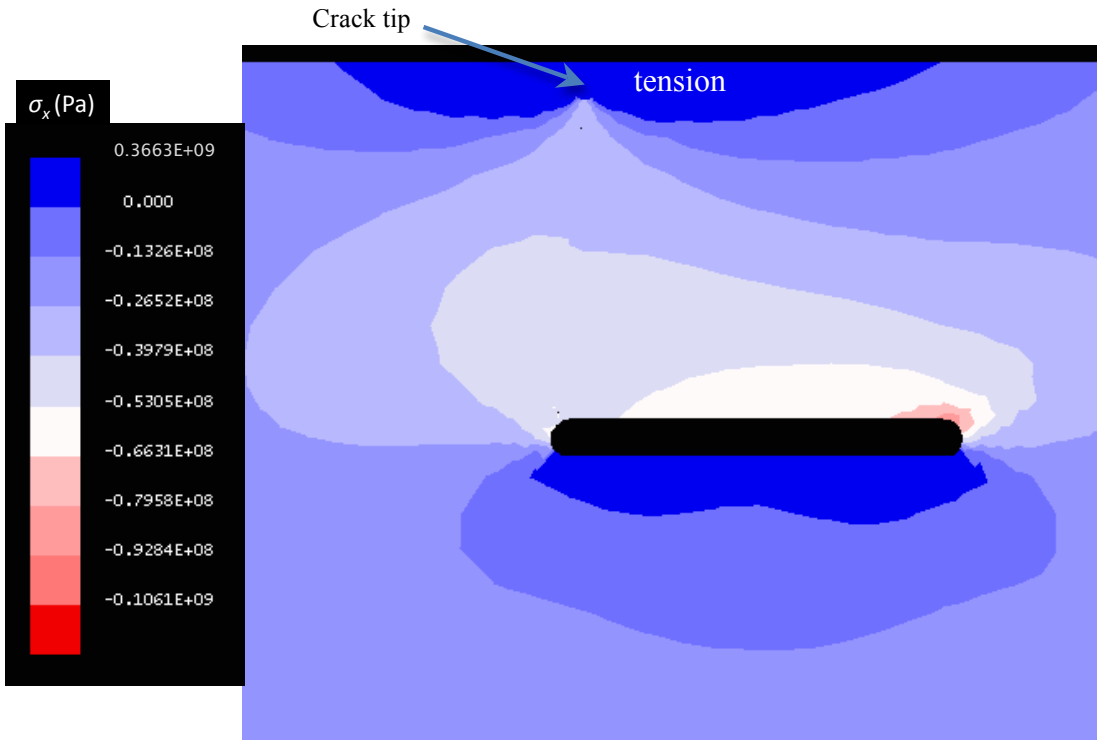

Figure 4.8 σ_x stress field induced by emplaced dike, where dark blue is tensile and the other colors show degree of compression. See Figure 4.6 for depiction of completed dike propagation.

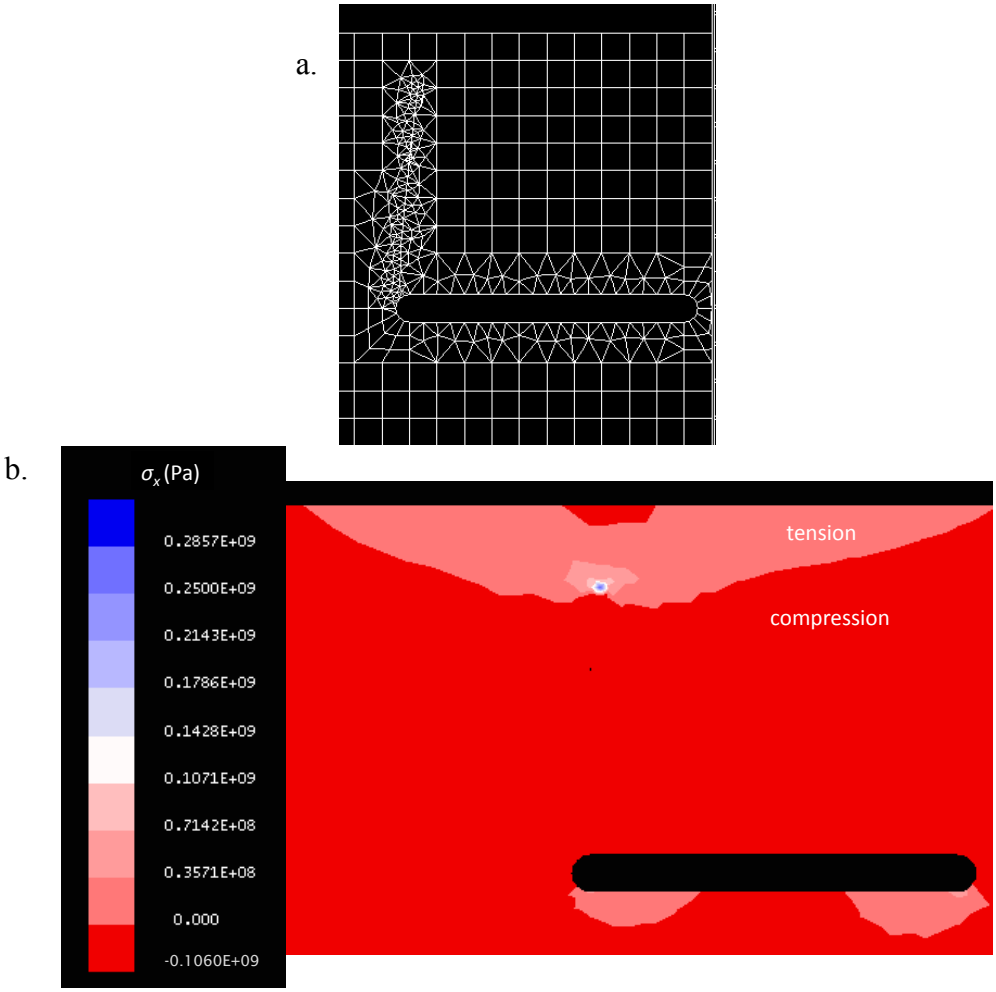

Figure 4.9 Model of shallow dike propagation, that stalls ~ 225 m from the surface for the terrestrial mid-ocean ridge case. **a.** Dike propagation path **b.** σ_x stress values. Note how tensile stress occurs above the crack tip to the surface and extends laterally ~10 km to each side. A permeability increase of ~ 10^2 is calculated within the tensile regions.

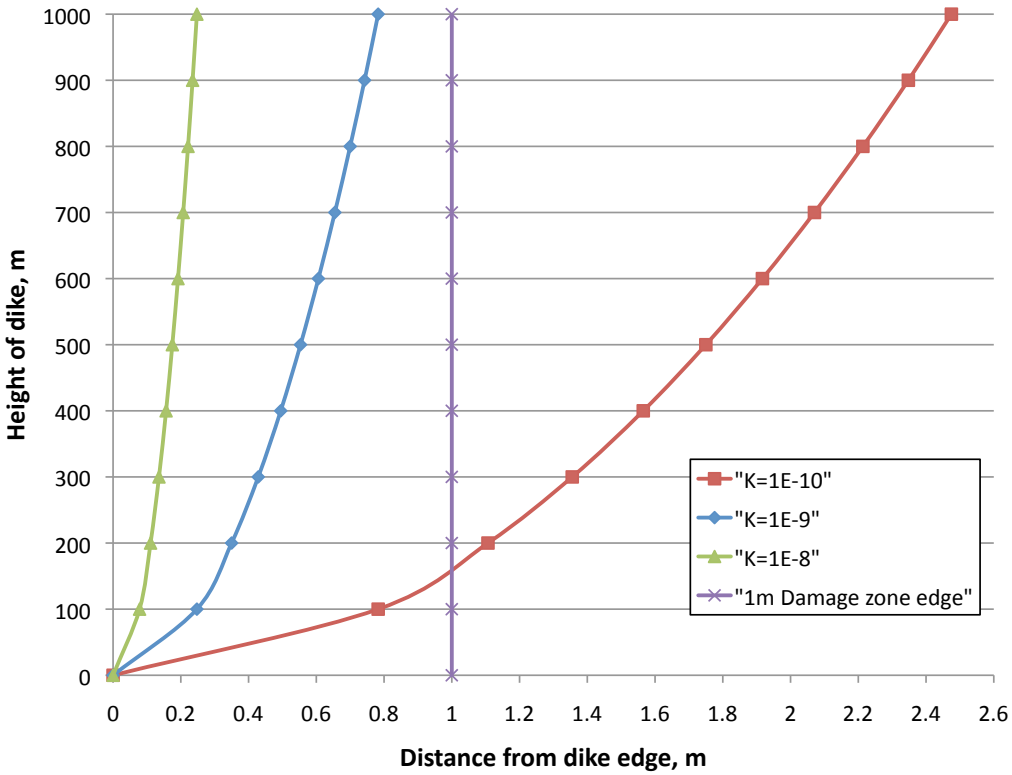

Figure 4.10 Boundary layer thicknesses next to a 1 km tall, 1 - 10 m wide dike beneath the mid-ocean ridge for the range of permeabilities between 10^{-10} to 10^{-8} m^2. For a 1 m wide dike, water flow within the boundary layer occurs at damage zone permeability values when $\delta \leq 1$ m and at the lower, dike induced permeabilities for $\delta > 1$ m. For a wider dike of 10 m, all flow will occur within its damage zone at the higher permeabilities.

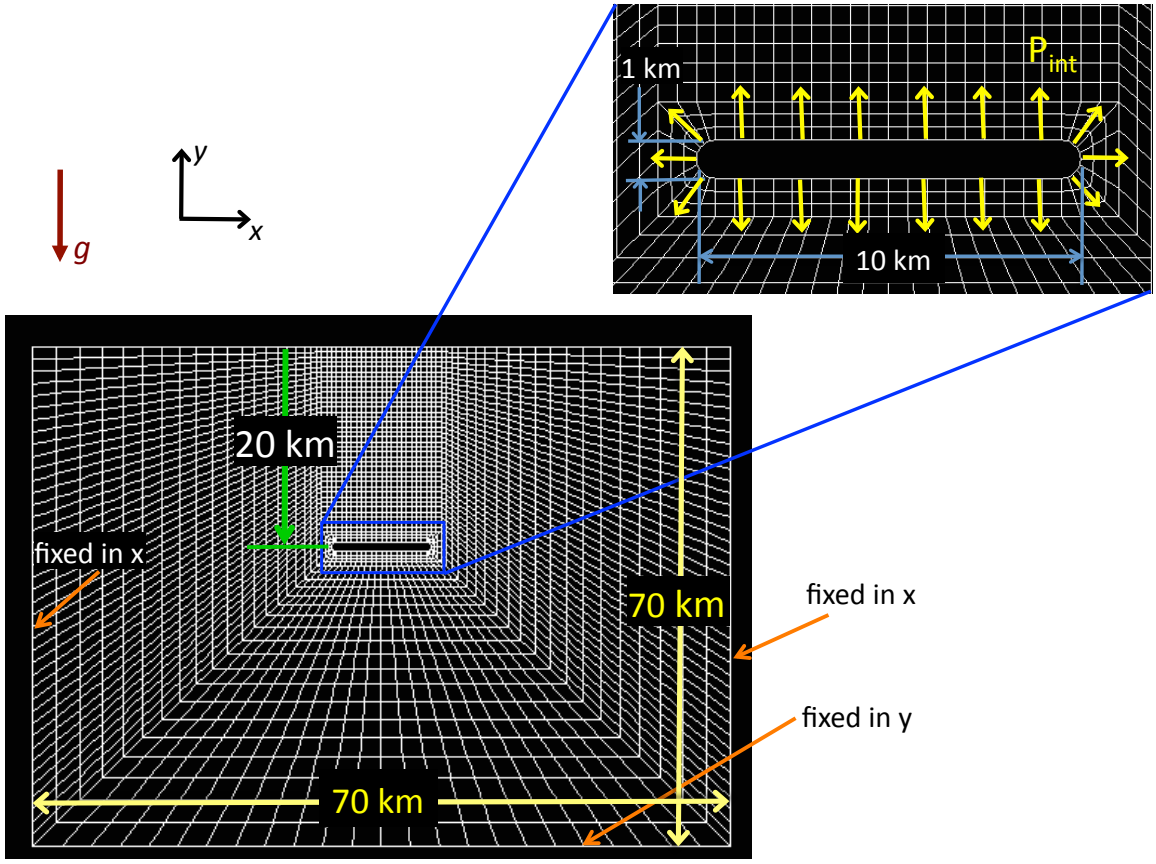

Figure 4.11 Martian dike emplacement model set-up

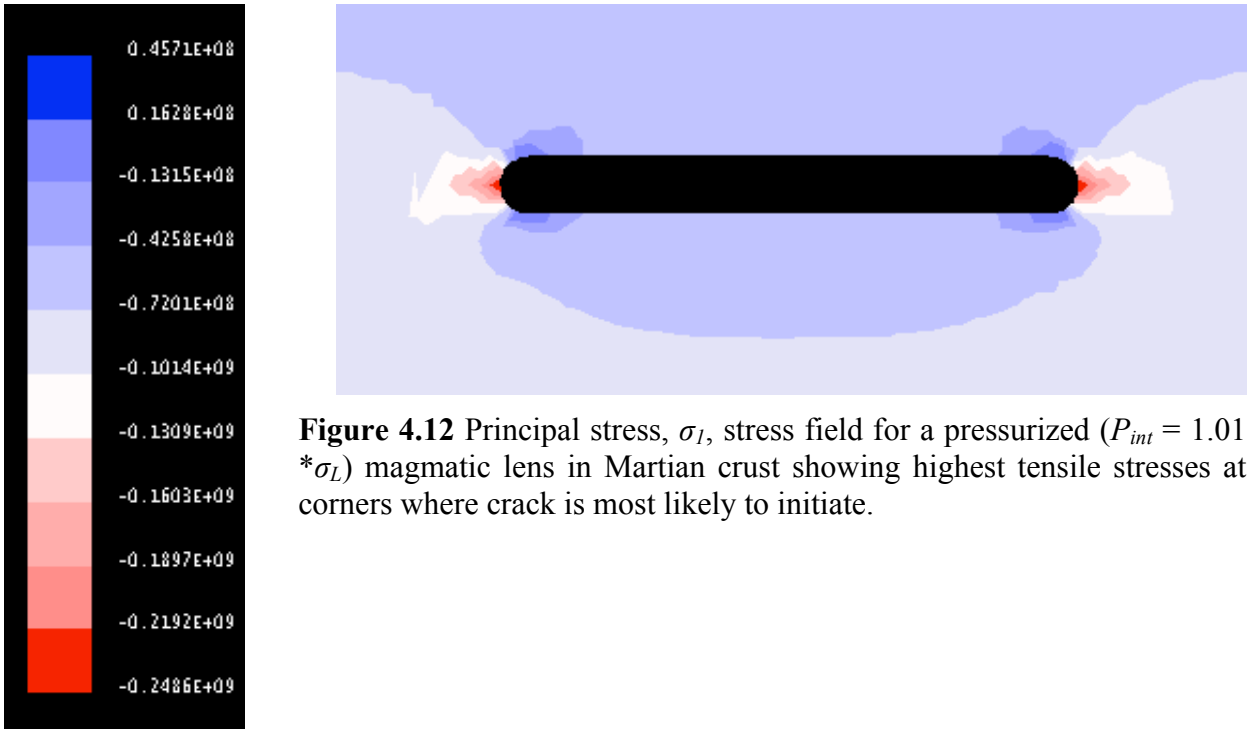

Figure 4.12 Principal stress, σ_1, stress field for a pressurized (P_{int} = 1.01 *σ_L) magmatic lens in Martian crust showing highest tensile stresses at corners where crack is most likely to initiate.

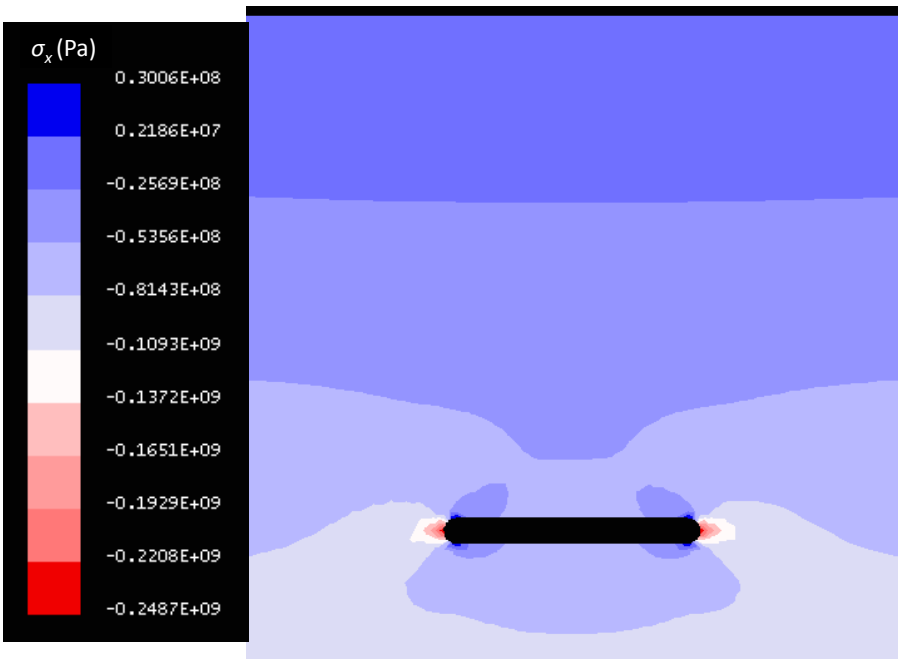

Figure 4.13 Stress field of horizontal stresses, σ_x, around pressurized magmatic lens before dike propagation for the base Mars model where $E = 10^{10}$ Pa.

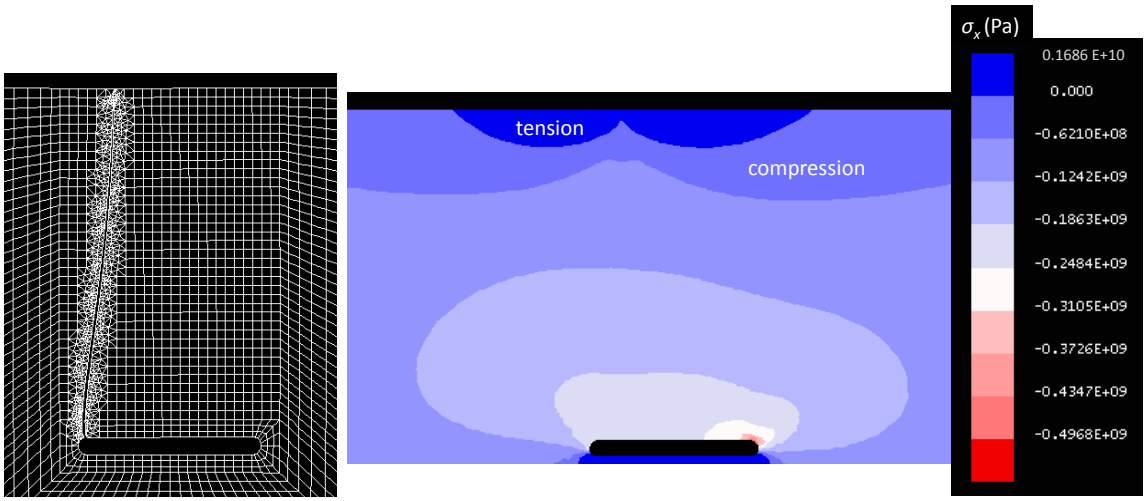

Figure 4.14 a. Dike propagation for model with $E = 10^{10}$ Pa. **b**. showing σ_x stress field induced by emplaced dike with dark blue showing areas in tension and other colors showing degrees of compression.

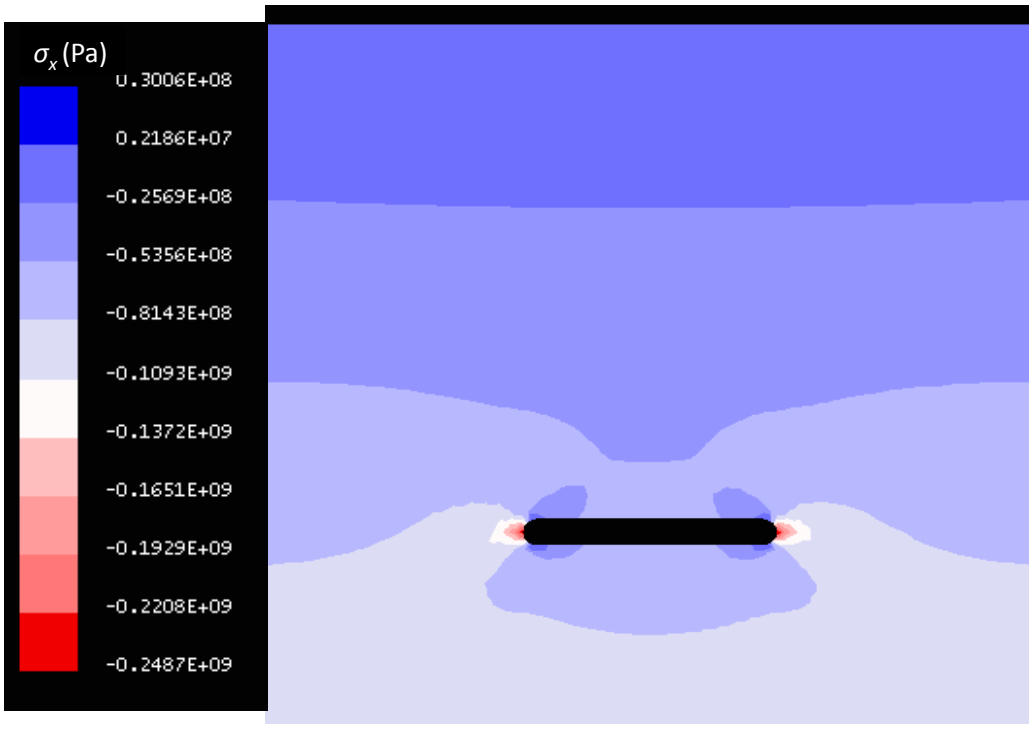

Figure 4.15 Stress field of horizontal stresses, σ_x, around pressurized magmatic lens before dike propagation for the Mars model where $E = 10^{11}$ Pa.

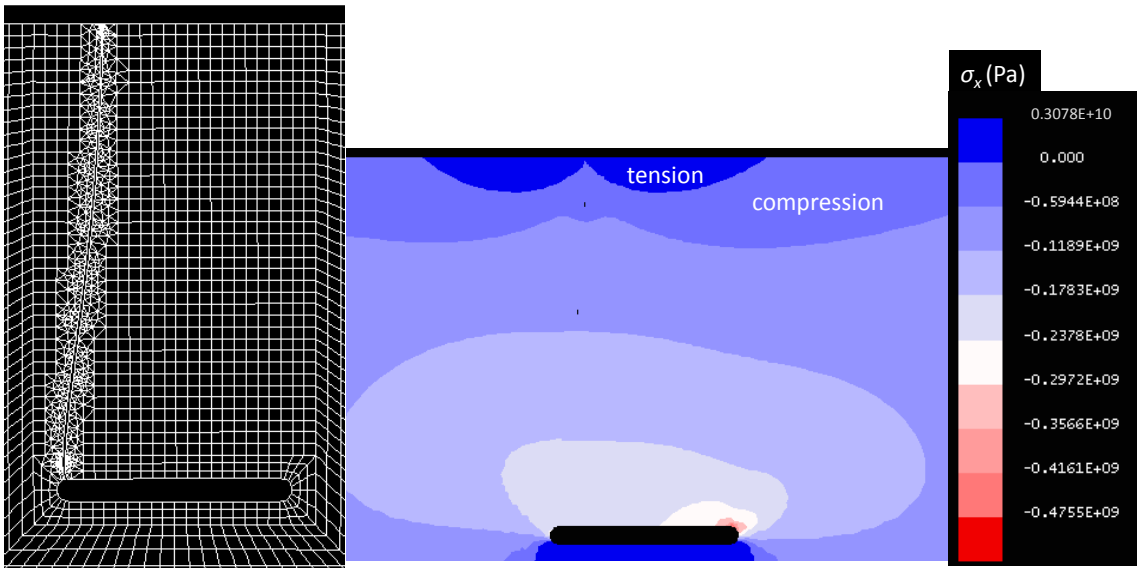

Figure 4.16 a. Dike propagation for model with $E = 10^{11}$ Pa. **b.** σ_x stress field induced by emplaced dike, where dark blue shows area in tension and other colors show degree of compression.

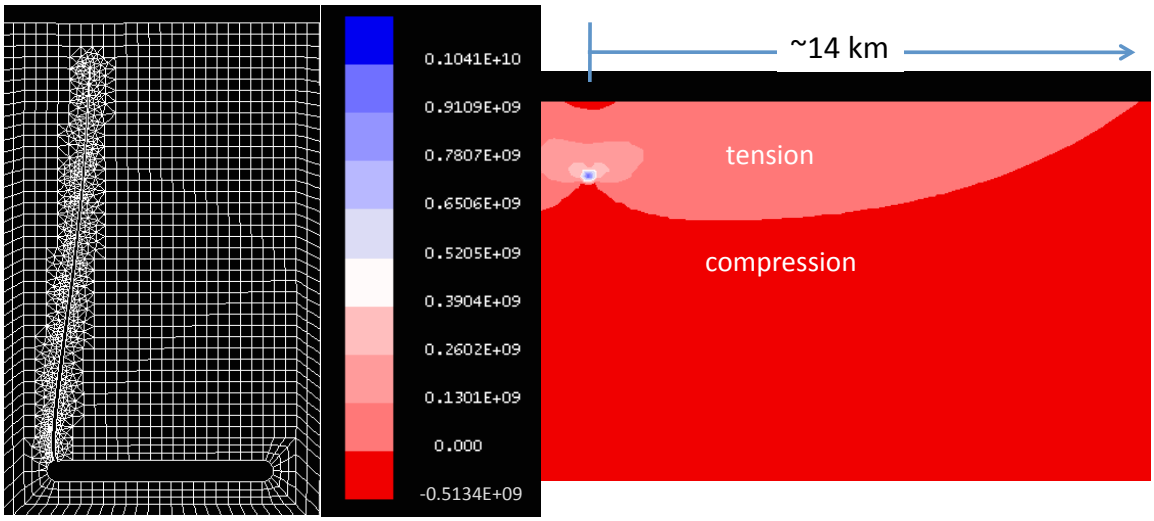

Figure 4.17 Model of a dike propagation that stalls ~ 2 km from the surface for the $E = 10^{10}$ Pa case. Note how σ_x stress field is in tension from the crack tip to the surface, and extends laterally ~12 km left and ~14 km right. An increase in permeability is expected within the regions in tension.

References

Anderson, T. L. (2005), *Fracture Mechanics*, 3rd ed., 621 pp., Taylor and Francis Group, Boca Raton.

Baker, E.T. (1998), Patterns of event and chronic hydrothermal venting following a magmatic intrusion: New perspectives from the 1996 Gorda Ridge eruption, *Deep Sea Res.,Part II, 45*, 2599-2618.

Baker et al. (1995), Hydrothermal event plumes from the coaxial seafloor eruption site, Juan de Fuca Ridge, *Geophys. Res. Lett., 22*, 147-150 DOI: 10.1029/94GL02403

Baker, E . T., J. W. Lavelle, R . A. Feely, G . J. Massoth S. L.Walker, and J.E. Lupton (1989), Episodic venting of hydrothermal fluids from the Juan de Fuca Ridge, *J. Geophys. Res., 94*, 9237-9250.

Baker, E. T., G. J. Massotha, and R. A. Feely (1987), Cataclysmic hydrothermal venting on the Juan de Fuca Ridge, *Nature*, *329*, 149-151.

Binder, A. B. and M. A. Lange (1980), On the thermal history, thermal state and related tectonism of a moon of fission origin, *J. Geophys. Res., 85*, 3194-3208.

Brace, W. F. and D. L. Kohlstedt (1980), Limits on lithospheric stress imposed by laboratory experiments, *J. Geophys. Res., 85*, 6248-6252.

Burr, D. M., A. S. McEwen, and S. E. H. Sakimoto (2002a), Recent aqueous floods from the Cerberus Fossae, Mars, *Geophys. Res. Lett., 29(1)*, 1013, doi: 10.1029/2001GL013345.

Burr, D. M., J. A. Grier, A. S. McEwen, and L. P. Keszthelyi (2002b), Repeated aqueous flooding from the Cerberus Fossae: Evidence for very recently extant, deep groundwater on Mars, *Icarus, 159*, 53–73.

Burr, D. M., P. A. Carling, R. A. Beyer, and N. Lancaster (2004), Flood- formed dunes in Athabasca Valles, Mars: Morphology, modeling, and implications, *Icarus, 171*, 68–83.

Byerlee, J. D. and W. F. Brace (1968), Stick-slip stable sliding and earthquakes: Effect of rock type, pressure, strain rate and stiffness, *J. Geophys. Res., 73*, 6031-6037.

Cherkaoui, A. S. M., W. S.D. Wilcock, and E.T. Baker (1997), Thermal fluxes associated with the 1993 diking event on the CoAxial segment Juan de Fuca Ridge: A model for the convective cooling of a dike, *J. Geophys. Res., 102*, 24,887-24,902.

Clifford, S.M. (1993), A model for the hydrologic and climatic behavior of water on Mars, *J. Geophys. Res., 98*, 10,973-11,016.

Coleman, R.G., *Ophiolites*, 229 pp., Springer-Verlag, New York, 1977.

Craft, K. L., and R. P. Lowell (2012), Boundary layer models of hydrothermal circulation on Mars and its relationship to geomorphic features, *J. Geophys. Res., 117*, E05006, doi:10.1029/2012JE004049.

Craft, K. and R.P. Lowell, 2009, A Boundary Layer Model for Submarine Hydrothermal Heat Flows at On-Axis and Near Axis Regions, Geochem. *Geophys. Geosyst. 10*, Q12012, doi:10.1029/2009GC002707.

Ernst, R. E., E. B. Grosfils and D. Mège (2001), Giant Dike Swarms: Earth, Venus, and Mars, *Ann. Rev. Earth Planet. Sci., 29*, 489-534, doi: 10.1146/annurev.earth.29.1.489.

Germanovich et al., 2000 Stress-dependent permeability and the formation of seafloor event plumes, *J. Geophys. Res., 105*, 8341-83

Germanovich, L. N., R. P. Lowell, and P. Ramondenc (2011), Magmatic origin of hydrothermal response to earthquake swarms: Constraints from heat flow and geochemical data, J. Geophys. Res., 116, B05103, doi:10.1029/2009JB006588.

Gold, T., B. T. O'Leary and M. Campbell (1971), Some physical properties of Apollo 12 lunar samples, *Proc. Lunar Sci. Conf., 2nd, 3*, 2173-2181.

Gudmundsson, A. (2011), Rock Fractures in Geological Processes, Cambridge University Press, Cambridge, UK.

Hanna, J. C. and R. J. Phillips (2006), Tectonic pressurization of aquifers in the formation of Mangala and Athabasca Valles, Mars, *J. Geophys. Res., 111*, E03003, doi:10.1029/2005JE002546.

Hauber, E., P. Brož, F. Jagert, P. Jodłowski, and T. Platz (2011), Very recent and wide‐spread basaltic volcanism on Mars, *Geophys. Res. Lett., 38*, L10201, doi:10.1029/2011GL047310.

Head, J. W., L. Wilson, and K. Mitchell (2003), Generation of recent massive water floods at Cerberus Fossae, Mars by dike emplacement, cryospheric cracking, and confined aquifer groundwater release*, Geophys. Res. Lett.*, *30*, NO. 11, 1577-80.

Hubert, M. K. and W. W. Rubey (1959), Role of fluid pressure in mechanics of overthrust faulting, *Bull. Geol. Soc. Am., 70*, 115.

Lowell, R. P., Crowell, B. W., Lewis, K. C. and Liu, L. (2013) Modeling Multiphase, Multicomponent Processes at Oceanic Spreading Centers, in Magma to Microbe (eds R. P. Lowell, J. S. Seewald, A. Metaxas and M. R. Perfit), American Geophysical Union, Washington, D. C.. doi: 10.1029/178GM03

Lowell, R. P., and L. N. Germanovich (1995), Dike injection and the formation of megaplumes at ocean ridges, *Science*, *267*, 1804- 1807.

Maxwell, J. C. (1964), Influence of depth, temperature, and geologic age on porosity of quartzose sandstones, *Bull. Am. Assoc. Pet. Geol., 48*, 697-709.

Mége, D. and P. Masson (1996), A plume tectonics model for the Tharsis province, Mars, *Planet. Space Sci.*, *44*, 1499–1546.

Mitchell, K. L., F. Leesch and L. Wilson (2005), Uncertainties in water discharge rates at the Athabasca Valles paleochannel system, Mars, *LPSC XXXVI*, Abstract #1930, LPI, Houston, TX.

Mouginis-Mark, P. J. (1990), Recent water release in the Tharsis region of Mars, *Icarus, 84*, 362-373.

Nehlig, P., and T. Juteau (1988), Flow porosities, permeabilities and preliminary data on fluid inclusions and fossil thermal gradients in the crustal sequence of the Sumail ophiolite (Oman), *Tectonophysics*, *151*, 199 – 221, doi:10.1016/0040- 1951(88)90246-6.

Pettijohn F. J. (1975), Sedimentary Rocks, 3rd ed., Harper and Row, New York.

Plescia, J. B. (2003), Cerberus Fossae, Elysium, Mars: A source for lava and water, *Icarus*, 164, 79– 95.

Ramondenc, P., Germanovich, L. N. and Lowell, R. P. (2013) Modeling Hydrothermal Response to Earthquakes at Oceanic Spreading Centers, in Magma to Microbe (eds R. P. Lowell, J. S. Seewald, A. Metaxas and M. R. Perfit), American Geophysical Union, Washington, D. C.. doi: 10.1029/178GM06

Rice, J. R., and M. P. Cleary (1976), Some basic stress diffusion solutions for fluid-saturated elastic porous media with compressible constituents, *Rev. Geophys., 14(2)*, 227– 241.

Rubin, A. M. (1995), Propagation of magma-filled cracks. *Annu. Rev. Earth Planet. Sci., 23*, 287-336.

Siegfried, R. W., G. Simmons, D. Richter and F. Horz (1977), Microfractures produced by a laboratory scale hypervelocity impact into granite, *Proc. Lunar Sci. Conf., 8th,* 1249-1270.

Sim, Youngjong (2004), Mechanics of Complex Hydraulic Fractures in the Earth's Crust, *PhD Dissertation* at Georgia Tech, Atlanta, GA.

Spence, D. A. and D. L. Turcotte (1985), Magma-Driven Propagation of Cracks, *J. Geophys. Res., 90*, B1, 575-580.

Spera, F. J., Aspects of magma transport, Physics of Magmatic ProcessesR. B. Hargraves, 263–323, *Princeton University Press,* Princeton, N.J., 1980.

Todd, T., D. A. Richter, G. Simmons and H. Wang (1973), Unique characterization of lunar samples by physical properties, *Proc. 4th Lunar Sci. Conf., Geochiem. Cosmochim. Acta, Suppl. 4, 3*, 2639-2662.

Thompson, A. B., and J. A. D. Connolly (1992), Migration of metamorphic fluid: Some aspects of mass and heat transfer, *Earth Sci. Rev., 32*, 107–121, doi:10.1016/0012-8252(92)90014-K.

van Everdingen, D. A. (1995), Fracture characteristics of the Sheeted Dike Complex, Troodos ophiolite, Cyprus: Implications for permeability of oceanic crust, *J. Geophys. Res., 100*, 19,957–19,972, doi:10.1029/95JB01575.

Vera, E.E., J.C. Mutter, P. Buhl, J.A. Orcutt, A.J. Harding, M.E. Kappus, R.S. Detrick, and T.M. Brocher (1990), The structure of 0- to 0.2-m.y.-old oceanic crust at 9°N on the East Pacific Rise from expanded spreading profiles, *J. of Geophys. Res., 95(B10)*, 15529-15556.

Wawrzynek, P. A. and A. R. Ingraffea (1987), Interactive finite element analysis of fracture processes: An integrated approach, *Theoret. App. Frac. Mech., 8,* 137-150.

Wilcock, W. S. D. and A. McNabb (1996), Estimates of crustal permeability on the Endeavour segment of the Juan de Fuca mid-ocean ridge, *Earth and Planetary Science Letters, 138*, 83-91.

Wilson, L. and J. W. Head (2002), Heat transfer and melting in subglacial basaltic volcanic eruptions: implications for volcanic deposit morphology and meltwater volumes, in *Volcano-Ice Interaction on Earth and Mars*, ed. by Smellie, J. L. and M. G. Chapman, Geological Society, London, Special Publications, *202*, 5-26.

Xenophontos, C., and G. C. Bond (1978), Petrology, sedimentation and paleogeography of the Smartville terrane (Jurassic): Bearing on the genesis of the Smartville ophiolite, in Mesozoic Paleogeography of the Western United States, edited by D. G. Howell and K. A. MacDougell, pp. 291-302, Soc. of Econ. Paleontol. and Mineral., Los Angeles.

5 CONCLUSIONS

5.1 Summary

In summary, this thesis investigated hydrothermal and fracturing processes on three planetary bodies, Earth, Mars and Europa. Hydrothermal boundary layer model results found that the water volumes produced by a dike-driven hydrothermal system were adequate to form Athabasca Valles, yet the flow rates were low. We suggest that episodic flood releases could enable the higher flow rates if water was first collected in aquifers, possibly stored beneath ice. On Europa, sill emplacement through fracturing processes appears possible with promising results for stress direction change that can turn fracture propagation more horizontal. However, the sill lifetime is less than the time a study by *Dombard et al.* [2013] calculated to be necessary for the formation of flexure fractures along margins of double ridges. The last study investigated dike induced permeability changes on Earth and Mars and related the changes to water and heat flow rates and water volumes. Comparisons were made to event plume heat and elevated fluid temperatures observed at mid-ocean ridges. Heat values determined by the models agreed well with the range of heat out expected. For the Martian model, water flow rates and volumes were compared to formation requirements for the valley system Athabasca Valles. Results found that flow rates would be adequate in the high permeability damage zone adjacent to the dike. However, the lowered permeability outside the damage zone would restrict replenishment flow and could cause the need for water storage and periodic release between flood events as the volume within the damage zone is not adequate for the valley formation.

5.2 Future Work:

Concerning sill emplacement on Europa, future work will explore the effect of crack spacing on fracture propagation and will study mechanical layering and lateral stress gradients in greater detail in an effort to enable wider sill emplacement. I also plan to investigate replenishment mechanisms for the sill in an effort to in crease its lifetime. Brine migration may play a role in helping to drive circulation. The Martian and terrestrial systems would benefit from an analysis that could look at the evolution of the heat, salinity, and fluid flow over time and also be able to consider permeability. The program FISHES [*Lewis*, 2009a, b] is a finite control volume code that can analyze complex systems such as this and also determine two-phase flow.

References

Bibring, J.-P., et al. (2004), OMEGA: Observatoire pour la Minéralogie, l'Eau, les Glaces et l'Activité, in Mars Express: The Scientific Payload, edited by A. Wilson, pp. 37–49, ESA Publ. Div., Noordwijk, Netherlands.

Dombard, A. J., G. W. Patterson, A. P. Lederer and L. M. Prockter (2013), Flanking fractures and the formation of double ridges on Europa, *Icarus, 223,* 74-81.

Lewis, K. C., and R. P. Lowell (2009a), Numerical modeling of two-phase flow in the NaCl-H2O system: Introduction of a numerical method and benchmarking, *J. Geophys. Res., 114* , B05202, doi:10.1029/2008JB006029.

Lewis, K. C., and R. P. Lowell (2009b), Numerical modeling of two-phase flow in the NaCl-H2O system: 2. Examples, *J. Geophys. Res., 114* , B08204, doi:10.1029/2008JB006030.

Murchie, S., et al. (2007), Compact Reconnaissance Imaging Spectrometer for Mars (CRISM) on Mars Reconnaissance Orbiter (MRO), *J. Geophys. Res., 112*, E05S03, doi:10.1029/2006JE002682.

Murchie, S. L., et al. (2009), Compact Reconnaissance Imaging Spectrometer investigation and data set from the Mars Reconnaissance Orbiter's primary science phase, *J. Geophys. Res., 114*, E00D06, doi:10.1029/2009JE003342.